Low–mass dielectron production in S-Au collisions at 200 GeV/n.

Carlos Pérez de los Heros.

Department of Particle Physics,
Weizmann Institute of Science.
Rehovot, Israel.

April, 1996.

Low–mass dielectron production in S-Au collisions at 200 GeV/n.

Carlos Pérez de los Heros.

Department of Particle Physics,
Weizmann Institute of Science.
Rehovot, Israel.

Thesis presented to the Feinberg Graduate School
of the Weizmann Institute of Science for the degree of PhD. in Physics.

Supervisor Prof. Itzhak Tserruya.

April, 1996.

To Mortadelo and Filemón for the good times spent together.

Abstract

Relativistic nuclear collisions offer a natural means of testing the prediction of QCD that at high enough temperatures and/or energy densities nuclear matter undergoes a phase transition to a deconfined state, the quark-gluon plasma (QGP). It is also predicted that chiral symmetry is restored under very similar conditions. Dileptons provide a unique probe of these predictions in several aspects: *i)* Due to their electromagnetic character they can leave the interaction region without further scattering, providing information on the very early stages of the collision, where QGP is expected to be formed. *ii)* They can distinguish between the QGP phase and a dense hadron gas due to the different features of the *thermal* dilepton yield in both phases. *iii)* They allow to assess chiral symmetry restoration through the detection of the in-medium modification of the ρ mass and width. A detailed discussion of these topics is given in Chapters 1 and 2.

CERES is the only experiment devoted to the measurement of low-mass ($0.1 < m_{e^+e^-} < 1.5$ GeV/c^2) e^+e^- pairs produced at mid rapidity in nuclear collisions at 200 GeV/c at the CERN SPS. As part of its physics programme, CERES has also measured low-mass e^+e^- pairs emitted in 450 GeV/c p-Be and 450 GeV/c p-Au collisions. These measurements serve as a reference for comparison with the nucleus–nucleus results. The detection of e^+e^- pairs in relativistic nuclear collisions represents a formidable experimental challenge and CERES has developed for that a novel spectrometer. Its essential components are two RICH detectors separated by a magnetic field. In addition, a silicon radial-drift chamber placed in the target region is used for a precise off-line determination of the event multiplicity and to help in the pattern recognition of the RICHes.

My work within the CERES collaboration was mainly concentrated in the analysis of the data taken in the spring of 1992 with a 200 GeV/c ^{32}S beam on an ^{197}Au target. This thesis presents the results of this analysis.

The e^+e^- invariant-mass spectra measured in the proton-induced interactions are very well explained, both in shape and absolute magnitude, by pairs from the known hadronic sources. However, the dielectron invariant–mass spectrum from S-Au interactions shows a different shape and a strong enhancement in the mass region $0.2 < m_{e^+e^-} < 1.5$ GeV/c^2 of a factor of $4.7 \pm 0.8_{stat} \pm 2.2_{sys}$ over the hadronic sources. The onset of the excess, starting at a mass of $\sim 2m_\pi$, together with a possible quadratic dependence on the event multiplicity, suggest the opening of the $\pi^+\pi^- \to e^+e^-$ annihilation channel. This would be the first observation of thermal radiation from dense hadronic matter. Several theoretical models proposed recently to explain the measured low-mass dielectron enhancement are summarized in the discussion of Chapter 7.

Resúmen

La colisiones de iones relativistas proporcionan una forma natural de probar la predicción de QCD de que a suficientemente alta temperatura y/o densidad de energía la materia nuclear sufre una transición de fase a un estado deconfinado, el plasma de quarks y gluones (QGP). QCD predice también que la simetría quiral se restablece en condiciones similares. La producción de dileptones es una herramienta única para corroborar estas predicciones en varios aspectos: *i)* Debido a su carácter electromagnético, los dileptones pueden escapar de la zona de interacción sin subsiguientes interacciones fuertes proporcionando, por lo tanto, información sobre los primeros estadios de la colisión, donde se espera que se forme el QGP. *ii)* Los dileptones pueden distinguir la fase QGP de la fase formada por un gas de hadrones a través de las distintas características de la produccion de dileptones térmicos en ambas fases. *iii)* Permiten estudiar el restablecimiento de simetría quiral a través de la medida de la modificación de la masa y anchura del ρ en el medio denso formado en la colisión. Una discusión detallada de estos temas se presenta en los Capítulos 1 y 2.

CERES es el único experimento dedicado a la medida de pares e^+e^- de baja masa ($0.1 < m_{e^+e^-} < 1.5$ GeV/c^2) producidos en colisiones nucleares a 200 GeV/c en el SPS del CERN. Como parte de su programa, CERES ha medido también pares e^+e^- de baja masa producidos en colisiones p-Be y p-Au a 450 GeV/c. Estas medidas sirven como referencia para comparar los resultados de interacciones núcleo–núcleo. La medida de pares e^+e^- en colisiones de iones relativistas supone un reto experimental formidable. El experimento CERES ha desarrollado para ello un espectrómetro especial. Sus componentes esenciales son dos detectores RICH separados por un campo magnético. Adicionalmente CERES usa una cámara de deriva radial de Silicio posicionada en la región del blanco que sirve para la determinación precisa de la multiplicidad cargada de los sucesos asi como para el reconocimiento de trazas en los RICHes.

Mi trabajo dentro de la colaboración CERES se concentró en el análisis de los datos tomados en la primavera de 1992 con un haz de ^{32}S de 200 GeV/c sobre un blanco de ^{197}Au . En esta tesis se presentan los resultados de dicho análisis.

Los espectros de masa invariante de los pares e^+e^- producidos en las interacciones inducidas con protones se explican satisfactoriamente, tanto en su forma como en la integral total, mediante las fuentes hadrónicas de e^+e^- conocidas. Sin embargo el espectro de masa invariante de los pares e^+e^- resultado de las interacciones S-Au presenta una forma diferente y un fuerte exceso, de un factor $4.7 \pm 0.8_{stat} \pm 2.2_{sys}$, en la región de masa $0.2 < m_{e^+e^-} < 1.5$ GeV/c^2 respecto a las fuentes conocidas. La aparición de dicho exceso, a $\sim 2m_\pi$, junto con su posible dependencia cuadrática con la multiplicidad del suceso, sugiere la apertura del canal de aniquilación $\pi^+\pi^- \rightarrow e^+e^-$. Este resultado sería la primera observación de radiación térmica emitida por un sistema de materia hadrónica extremadamente denso. En la discusión del Capítulo 7 se resúmen varios modelos teóricos que han sido propuestos recientemente para explicar el exceso de dielectrones de pequeña masa medido por CERES.

Acknowledgments:

During the last four years, since I joined the Weizmann group of the CERES collaboration, I have enjoyed a very pleasant working environment and many useful discussions with my colleagues. I would specially like to mention Prof. Itzhak Tserruya who welcomed me into his group and guided this thesis with his excellent advice and assistance. Prof. Zeev Fraenkel has been a source of help and professional support through these years.

I greatly benefitted in my first contacts with the CERES hardware and software from the experience and patience of Victor Steiner. To Ilia Ravinovich and Guy Tel-Zur I express my gratitude for their help with the Monte Carlo simulations and with all the other questions that I kept asking them. G. Li and W. Cassing have helped me with the understanding of their codes and have kindly provided their figures which I include in the discussion of chapter 7.

The members of the Heidelberg group helped me in many ways with software problems along these years. I would like to mention Thomas Ullrich for his help with all matters related with the CERES data analysis and Andreas Pfeiffer for his assistance with all kind of on-line data taking details during the runs. I would also like to thank Prof. Peter Wurm for his support during my stay at the Heidelberg University.

All the friends that I have made during these years in Israel have given me excellent moments that I will always remember.

To all of you, thanks for making this work possible.

Rehovot, April 1996.

Had I been present in the Creation,
I would have given some useful hints
for the better ordering of the Universe.

Alphonse X (1221-1284), king of Castille,
after being presented the Ptolemaic system.

Contents

1 Introduction **1**
1.1 The rationale for relativistic heavy ion collisions. 1
1.2 The dynamics of a relativistic nuclear collision. 3
1.3 Main experimental results from the first round of heavy ion experiments. . . . 3
1.3.1 Global interaction features. 3
1.3.2 QGP signatures. 8
1.4 Dileptons as a probe of relativistic nuclear interactions. 11
1.5 The dilepton programme at CERN. 12
1.6 The CERES physics programme. 12

2 Sources of dileptons in hadronic and nuclear collisions **15**
2.1 Electron pair production in nucleon–nucleon collisions 15
2.1.1 e^+e^- pairs from hadron decays 16
2.1.2 e^+e^- production through Drell-Yan annihilation 19
2.1.3 Heavy flavour decay into e^+e^- 21
2.2 Dilepton production in hadronic collisions: present status. 21
2.3 Dilepton production in nuclear collisions 22
2.3.1 Thermal e^+e^- production from the hot fireball. 24
2.3.2 e^+e^- production through bremsstrahlung 27
2.3.3 e^+e^- pairs from vector meson decays 27
2.4 Summary of contributions to the dielectron spectrum 29

3 The CERES experiment. **31**
3.1 Spectrometer description and performance. 31
3.1.1 Overall design. 31
3.1.2 The UV detectors. 34
3.1.3 Performance of the RICH detectors. 37
3.1.4 The Silicon Pad Detector. 40
3.1.5 The Silicon Drift Chamber. 42
3.1.6 The trigger system. 46
3.2 Signal and Background estimates. 47

4 The Monte Carlo e^+e^- -pair generator **53**
4.1 Relative particle-production cross sections. 53
4.1.1 Parameterization of the particle-production cross sections. 53
4.2 Functional form of the different particle decays. 55
4.3 Invariant mass distribution from the Monte-Carlo generator. 57
4.3.1 Comparison of the Monte Carlo results with experimental data. 59

5 The $S - Au$ data sample and analysis **61**
5.1 The 1992 heavy ion running conditions. 61
5.1.1 The target. 61
5.1.2 Trigger. 62
5.2 The data analysis procedure. 63
5.2.1 Pattern recognition. 64
5.2.2 Extraction of the signal. 72

6 Results **77**
6.1 Dielectron signal. 77
6.2 Normalization of the signal 79
6.2.1 Trigger enrichment. 79
6.2.2 Pair reconstruction efficiency. 82
6.3 Differential e^+e^- invariant mass spectrum. 83
6.4 Multiplicity dependence of the dielectron yield. 85

7 Discussion **89**
7.1 Comparison with other experiments. 89
7.2 Comparison with theoretical models. 90

Appendix
Basic Čerenkov radiation formulae 95

List of Figures

1.1 Schematic view of the phase diagram of nuclear matter (not to scale). Heavy ion collisions are expected to bring the interacting system along the dotted line to a QGP phase. 2
1.2 Differential nuclear cross section as a function of E_t measured by NA34 (left) and as a function of multiplicity measured by E802 (right). 4
1.3 A simple geometrical picture of an interaction of two nuclei at impact parameter b in terms of *participants* and *spectators*. 5
1.4 Ratio of the p_t distribution of A-A to p-p collisions (the dotted curve is to guide the eye). 7

2.1 Dalitz decay of the type Vector(Pseudoscalar) $\rightarrow$ Pseudoscalar(Vector) e^+e^- . 16
2.2 Dalitz decay of the type Pseudoscalar $\rightarrow$ $\gamma\, e^+e^-$ 16
2.3 VMD model of coupling of hadrons to photons 18
2.4 Form factor of the η as predicted by the VMD model (dashed line) compared with a pole-fit (full line) of the available data. 19
2.5 Form factor of the ω as predicted by the VMD model (dashed line) compared with the available data. See the text for details on curves 1, 2 and 4. 19
2.6 Lowest order lepton pair production through the Drell-Yan process. 19
2.7 Results on e^+e^- production in p-Be interactions from HELIOS/1 collaboration. The data is compared to the predicted yield from the conventional hadron sources. 22
2.8 The space-time (left) and temperature (right) evolution of a nucleus-nucleus collision. 23
2.9 Lowest order bremsstrahlung processes from elastic pion scattering. 27

3.1 Schematic view of the CERES spectrometer. 32
3.2 The CERES general coordinate system. 33
3.3 The amplification/detection scheme of the UV detectors. Distances are shown in mm for UV1/UV2. 35
3.4 A S+Au collision as seen in RICH2. A series of background hits and two asymptotic electron rings can be easily identified. The pad structure of one of the rings is shown in the right plot. 36
3.5 Measured distribution of number of hits per ring. The curve is a fit to a Poisson distribution. 38

3.6 Measured single hit resolution for high momentum (p_t >0.2 GeV) particles. The curve is a fit to a gaussian plus a linear background. The values quoted are the r.m.s in mrad. 41

3.7 **left:** The SiPAD detector, where the pad structure of the eight concentric sectors can be seen. The grey scale is proportional to the analog signal seen by each pad. The summed analog signal of these sectors is used to define the first–level trigger. **right:** The number of hit pads as a function of the event multiplicity. The superimposed curve represents the expectation of a uniform multiplicity distribution over the covered pseudo-rapidity range. 42

3.8 **Left:** Schematic view of the SiDC detector. **Right:** A typical S+Au event as seen by SiDC. The SiDC provides the (θ, ϕ) coordinates of the charged particles produced in the collision and serves for the off-line characterization of the event multiplicity. 43

3.9 SiDC efficiency. 45

3.10 The CERES target area. A double wall carbon fibre tube serves both for holding the SiPAD and the SiDC in position respect to the beam direction and for the cooling system. 46

4.1 **Left:** Rapidity distribution of pions produced according to Bourquin-Gaillard (BG) parameterization, equation (4.1), and according to the modified Bourquin-Gaillard (MBG), equation (4.7). The superimposed data correspond to S-S collisions at 200 GeV/n measured by NA35. **Right:** p_t distribution from π^o 's generated according the modified BG parameterization. Data of p-p collisions at 450 GeV/c from NA27 is superimposed. 55

4.2 Invariant mass distribution of the hadronic decays known to contribute to the CERES mass range. The yield has been scaled by the measured average charged particle multiplicity in S-Au collisions. 58

4.3 Comparison between the generated dielectron invariant mass spectrum and CERES data on p-Be at 450 GeV/c. 59

5.1 Charged particle multiplicity distribution. The white dots represent the actually measured down-scaled distribution. The black dots represent the distribution corrected by the down-scaling factor. 63

5.2 Measured charged particle multiplicity distributions from the FLT and SLT data samples. The distributions have been normalized to the same (arbitrary) number of entries to enhance the difference in shape. 63

5.3 Variation of the UV detectors gain along the Sulphur run period. An off-line gain correction brings the run gain to a nominal of 5×10^5, shown as the horizontal line in the plots. 64

5.4 A typical S-Au event as seen by the CERES first RICH detector. Unphysical pad clusters due to electronic instabilities or particle tracks traversing the UV detector seen in the raw event (top) are removed by the off-line software (bottom). 66

5.5 An asymptotic electron ring as seen in the pad array (left) and its Hough transformation (right). The Hough transformation gives a peak at the ring center position (bottom). 68

5.6 Fitted ring in RICH2. The original candidate centers are shown as the crosses. Only one of the three potential candidates survived the Hough peak quality cut or the fitting cuts applied. 69

5.7 Matching of rings between RICH1 and RICH2. The angular displacement results from the combined effect of the magnetic field deflection, the ring center resolution and the multiple scattering. 71

5.8 The actual butterfly-shaped area used in the analysis to match rings between RICH1 and RICH2. In this event two rings have been found in RICH2 within the search area of the ring in RICH1. Such pattern is identified as a γ conversion. 71

5.9 Distribution of the fitted vertex position in the x-y plane. The circle shows the position and size of the target disk. 72

5.10 p_t of single tracks and opening angle distributions of the e^+e^- pair from the π^o Dalitz and $\rho \to e^+e^-$ decays. 73

5.11 **Left:** Distribution of the analog sum for single and double rings. **Right:** Corresponding recognition and rejection efficiency curves based on the summed analog cut. 74

5.12 **Left:** Distribution of the number of hits for single and double rings **Right:** Corresponding recognition and rejection efficiency curve based on the number of hits cut. 74

6.1 Like-sign and unlike-sign pair invariant mass distributions. 78

6.2 Trigger rejection, efficiency and enrichment as a function of the charged particle rapidity density. The three curves of the rejection factor shown correspond to the three methods of obtaining the rejection as explained in the text. 81

6.3 Pair reconstruction efficiency as a function of the event multiplicity for pairs with $m > 200$ MeV/c^2 (left) and as a function of the pair invariant mass (right). In both cases a $p_t > 0.2$ GeV/c^2 cut on each track and an opening angle cut of $\Theta > 35$ mrad. was applied. 83

6.4 Dielectron invariant mass spectrum obtained from the S-Au data by CERES. . 85

6.5 Dependence of the e^+e^- yield on the event charged particle multiplicity for both the FLT and SLT data samples. The lowest plot shows the combined FLT+SLT results. We have used the average trigger enrichment from the three possible methods discussed in the text. 86

7.1 Results from HELIOS (left) and NA38 (right) collaborations on dimuon production in both p-nucleus and nucleus-nucleus collisions. 90

7.2 Comparison of the predictions of the models of Li *et al*, Cassing *et al* and Srivastava *et al* with CERES data. See the text for further details and references. 92

7.3 Comparison of the prediction of the models from Li *et al* and Cassing *et al* with CERES data when the in-medium modification of the ρ mass is included. See the text for further details and references. 93
7.4 Momentum dependence of the Čerenkov ring radius for pions and muons with respect to the asymptotic electron one in RICH1. 97

List of Tables

3.1 Specifications of the two RICH detectors. 37
3.2 Comparison of the expected an measured average number of photons per ring. 39
3.3 Comparison of the expected and measured single hit resolution. 40
3.4 Specifications of the SiDC geometry and materials. 44
3.5 Estimate of the e^+e^- production rate from meson decays relative to π_o emission at central rapidity in p-p collisions. $\epsilon_{m>200}$ represents the fraction of the e^+e^- yield above mass $m > 0.2$ GeV/c^2. 48
3.6 List of materials and corresponding radiation length in the CERES spectrometer used during the S+Au run of April 1992. 49
3.7 Expected e^+e^- pairs per event from the signal and the main physical background sources relevant to CERES, π^o Dalitz decays and γ conversions. 50

4.1 Values of the total cross sections and branching ratios into e^+e^- of the hadron decay processes included in the CERES Monte Carlo generator. 54
4.2 Λ values used in the pole-type form factors of equation 4.10 57

5.1 Data sample of the CERES 1992 heavy ion run. In the case of the second level triggered (SLT) the number of minimum bias equivalent events is calculated from the analyzed sample taking into account the trigger enrichment (see Section 5.2.2 below). 62

6.1 Sample sizes in the FLT, SLT and total data sets. 78
6.2 Trigger rejection, efficiency and enrichment factors obtained by the different methods mentioned in the text. 80
6.3 Values of the quantities used in the normalization of the data. The pair reconstruction efficiency ε is a function of mass (see Figure 6.3) and only the average value is quoted. E is the average trigger enrichment factor as determined in Section 5.2.2 84

7.1 Threshold momenta, p_{thr}, ring radius at p_{thr} and momenta for a radius equal to the asymptotic electron radius for pions and muons in RICH1. 96

Chapter 1

Introduction

1.1 The rationale for relativistic heavy ion collisions.

It is now about ten years since the first heavy ion beams became available at both the SPS at CERN and the AGS at BNL. CERN provided beams of ^{32}S and ^{16}O at 60 and 200 GeV/nucleon, while the AGS used ^{16}O and ^{28}Si at 14 GeV/nucleon. A series of experiments at both laboratories were set up to start a systematic study of the interactions of such heavy ions on several fixed heavy targets, typically ^{197}Au and ^{208}Pb . Currently a new round of experiments are being carried out with heavier projectiles, ^{197}Au at 11 GeV/nucleon at AGS and ^{208}Pb at 160 GeV/nucleon at CERN.

In an interaction of, say, a ^{32}S nucleus on a ^{208}Pb one at the above mentioned energies, several hundreds of charged particles are emitted. Being mainly a many-body strong interaction process it is an extremely difficult task to understand which are the exact reaction mechanisms at play. Why then to embark on such an ambitious programme when one can study the strong interaction in e^+e^- , $p\bar{p}$ or ep collisions with at most a few tens of particles in the final state? The main reason is that nucleus-nucleus (AA) collisions are expected to produce the appropriate conditions of pressure and energy density for a phase transition from highly excited hadronic matter to a plasma of free quarks and gluons (QGP) to occur. The prediction of this phase transition dates back to the work of Polyakov in 1978 [1], whose analysis of a thermal system described by the Yang-Mills Hamiltonian shows that confinement is absent for small values of the inverse temperature parameter β.

Restoration of chiral symmetry as we approach the deconfining phase transition is another prediction of QCD which can be tested with heavy ion collisions [2]. The gradual melting of the chiral condensate $\langle\phi\bar{\phi}\rangle$ as the chiral restoration temperature is approached is expected to modify the mass and width of the lightest mesons in a strong fashion. This will distort the shape of their different decay channels in an experimentally measurable way.

The study of the possible QCD phase transition by means of heavy ion collisions is also relevant to Cosmology and Astrophysics. The Universe is supposed to have gone through this transition a few μs after the Big Bang, whilst cooling from the hot and dense primeval fireball to the nucleosynthesis era. Any density inhomogeneity at the hadronization time that might have survived this process could have an important role in the large scale structure of the universe observed today [3]. Also a thorough understanding of the behaviour of hot and dense nuclear matter is an essential ingredient for the study of the contraction of supernova–candidate massive stars which will eventually result in the formation of neutron stars. It has also been suggested that the core of neutron stars may exist in the form of cold and highly compressed QGP [4].

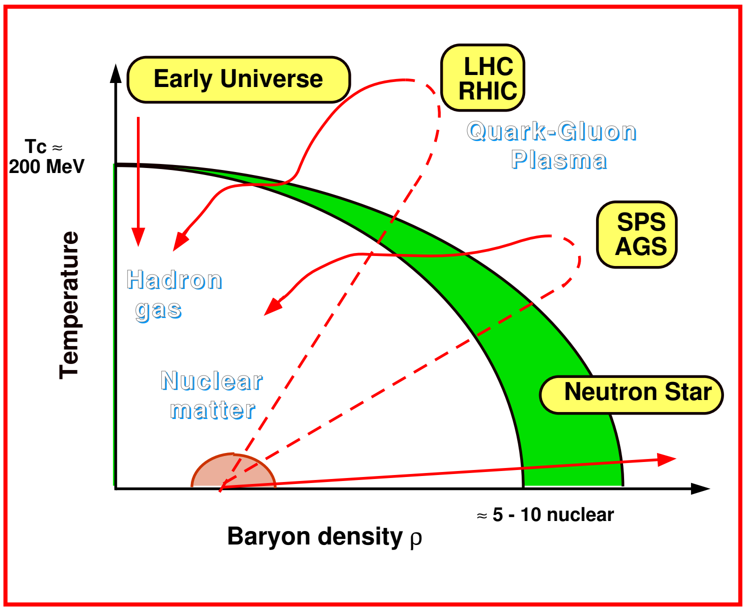

Figure 1.1: Schematic view of the phase diagram of nuclear matter (not to scale). Heavy ion collisions are expected to bring the interacting system along the dotted line to a QGP phase.

The ultimate aim in the study of relativistic heavy ion physics must be deriving a phase diagram of nuclear matter as the one shown in Figure 1.1 from first principles. The framework provided by QCD is adequate in the high energy limit where perturbative expansions can be applied reliably. However, processes at “low” energies (below the GeV scale) like the hadronization of QGP or the hadron decays (with a typical energy scale of the hadron mass), are intractable within QCD at present. For this “low energy” regime a series of effective models are used to carry out actual calculations. We may cite among the more popular the Dual Parton model [5], Lattice QCD [6], QCD sum rules [7, 8] and chiral lagrangian approaches [9, 10]. See also the proceedings of the several Quark Matter conferences held so far for a comprehensive view of the field [11].

On the experimental side, in order to study the phase transition to a deconfined QGP and the properties of the QGP itself we must create a system which is both “big” compared to the hadronic radius, and "long lived" compared to typical strong interaction time scale. These requirements become clear if we think that we want to detect free quarks and gluons and that such freedom should manifest itself over distances greater than the confining radius of the strong force ($\sim$ 1 fm). Moreover, to be able to apply thermodynamic methods, we must have a long-lived and dense (many-particle) system which can reach thermal equilibrium through the interaction of its constituents. The collisions of heavy ions at relativistic energies are expected to create such a system in the laboratory.

1.2 The dynamics of a relativistic nuclear collision.

We will see in a detailed manner the space-time evolution of an interaction between two heavy nuclei at high energies in Chapter 2, but with the help of Figure 1.1 we can picture it in the following way: in a first stage, inelastic scattering between the quarks inside the incoming nucleons takes place, redistributing the original beam energy into internal degrees of freedom, driving the system along the dotted line(s) in Figure 1.1. Since the two incoming nuclei are Lorentz-contracted along their direction of motion, the initial energy is deposited in a small region of space in a short interval of time, forming a hot and dense *fireball*.

As the system expands and cools down through the full line(s) of Figure 1.1, the QGP hadronizes into a highly excited hadron gas which subsequently cools down and finally decouples. The products of the collision are therefore detected by the experiments long after the interactions have ceased, leaving the experimentalist with the difficult task of disentangling the space-time evolution of the system from the detected particles.

There are several observables that have been proposed as useful tools to probe the interaction dynamics and the characteristics of the fireball formed. We refer the reader to the topical reviews of J. Cleymans *et. al.* [12], H. Stocker and W. Greiner [13], H. R. Schmidt, J. Schukraft [14] and the books by H. Wong [15] and R. C. Hwa [16] for a detailed description and implications of such "QGP probes". We will present in the next section just a concise summary of the main results obtained by the first round of heavy ion experiments at CERN and BNL (see I. Tserruya in [17] for a comprehensive recent review), and we will concentrate in describing in a separate section the interesting features of the dilepton yield, which is the topic of the present work.

1.3 Main experimental results from the first round of heavy ion experiments.

1.3.1 Global interaction features.

There are several variables which are widely used to extract information of the global features of a collision between two heavy ions: the transverse energy, E_t, the transverse momentum,

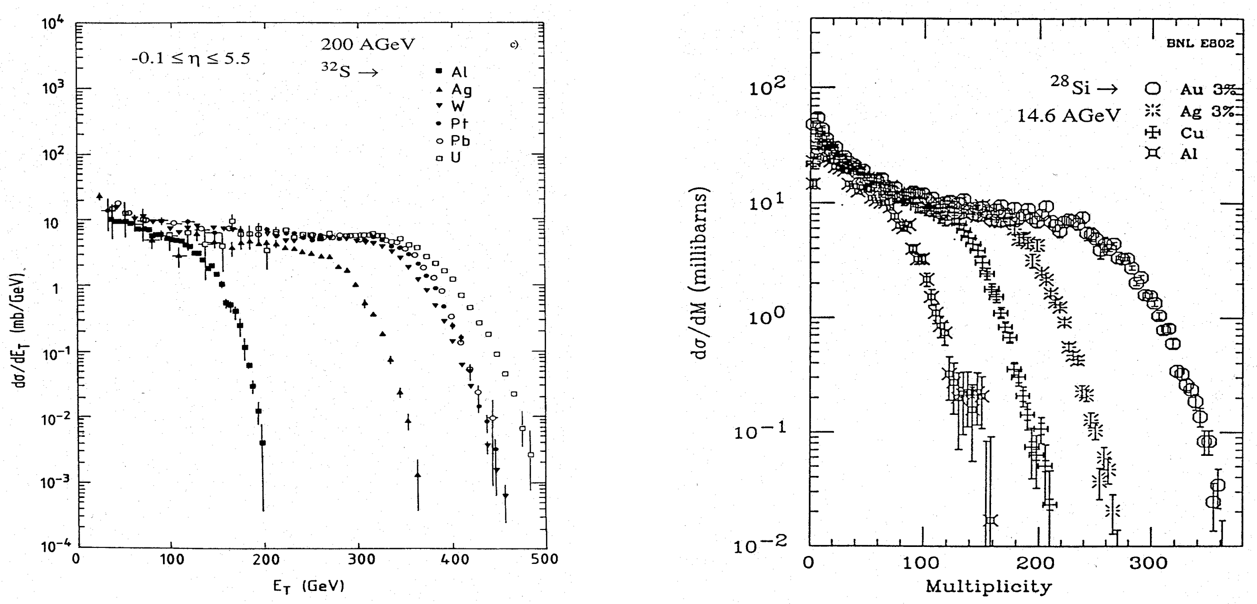

Figure 1.2: Differential nuclear cross section as a function of E_t measured by NA34 (left) and as a function of multiplicity measured by E802 (right).

p_t, and the particle multiplicity distributions.[1)] Furthermore one can use pion interferometry, (HBT effect), to obtain information on the global size of the fireball at hadronization time. From these observables one can deduce, in a model-dependent way, the initial conditions reached in the interaction. As the subsequent evolution of the fireball strongly depends on its initial condition, the study of these variables has provided a realistic input for phenomenological models of the space-time evolution of heavy ion collisions which, in turn, are used to extract predictions on particular aspects of the interaction.

Transverse energy, E_t:

The transverse energy and the charged particle multiplicity are closely related since they both reflect the amount of initial energy used for new final degrees of freedom: high E_t values correspond to high depositions of initial energy in the interaction region, and a high number of particles is produced. Furthermore they can be related to the impact parameter and initial energy density achieved.

The differential total cross section as a function of these variables, $d\sigma/dE_t$ and $d\sigma/dN_{ch}$, is shown in Figure 1.2 as obtained by HELIOS [18] and E802 [19] collaborations respectively. The spectra reflect the geometry of the interaction through the probability distribution of the number of possible incoming nucleon-nucleon interactions, which can be calculated taking into account the extended character of the nuclei (as for example in the Glauber model) [20, 21, 22]. In a first approximation we can picture the geometry of a nuclear collision as

[1)] Usually the experiments measure the charged particle multiplicity, N_{ch}.

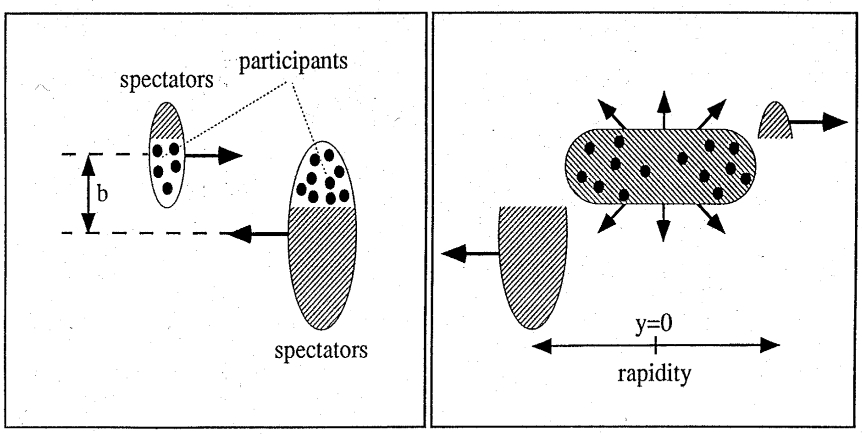

Figure 1.3: A simple geometrical picture of an interaction of two nuclei at impact parameter b in terms of *participants* and *spectators*.

shown in Figure 1.3. The "participant" nucleons from the overlapping volume of the two incoming nuclei define the volume of the interaction and the average number of possible individual nucleon-nucleon interactions. The rest are "spectator" nucleons, which do not take active part in the collision.

With this simple approach we can understand the distributions of Figure 1.2. The low E_t region presents a "neck" corresponding to the large cross section of peripheral collisions, with only a few participants. With decreasing impact parameter the number of participants increases until reaching the full overlap of the two nuclei. This corresponds to the "plateau". This plateau reaches a "knee" for impact parameters close to zero followed by a high-E_t rapidly-decreasing tail, which accounts for fluctuations in the number of individual nucleon-nucleon collisions. The $d\sigma/dN_{ch}$ distribution shows a similar shape as it is expected from its correlation with E_t.

But the main interest in measuring the E_t distribution is its link with the initial energy density ϵ_o achieved in the collision. To relate the measured E_t to ϵ_o we need a model for the space-time evolution of the interaction. A popular choice is the Bjorken model [23]. It provides a simple description of the development of a nuclear collision, where a *formation time* τ_o is introduced to account for the fact that it takes a certain time for the matter in the fireball to reach local equilibrium after the collision. The subsequent evolution of the system is described using standard hydrodynamical and thermodynamical techniques [24]. The initial energy density of the system in this model is given by

$$\epsilon_o = \frac{1}{\tau_o \mathcal{A}} \frac{dE_t}{dy}\bigg|_{y=0} \tag{1.1}$$

where τ_o is the formation time and $\mathcal{A}$ the transverse area of the system. τ_o is usually taken to be 1 fm/c and $\mathcal{A}$ as the transverse area of the projectile nucleus, $\mathcal{A} \sim \pi\, r_o^2 A^{2/3}$ fm^2 with r_o the nuclear radius parameter, $r_o = 1.2$ fm [23].

The data of NA35 [25], WA80 [26, 27] and HELIOS [28] show that the maximum values of dE_t/dy achieved at SPS energies give an initial energy density of $\sim 2-3$ GeV/fm^3 or, equivalently, a compression $\rho/\rho_{nuclear} \sim 12-20$ [14, 29]. These energy densities are comparable to those predicted for the phase transition to QGP, but we must stress that a high energy density alone does not necessarily imply the formation of QGP. Additional evidence from the probes that we will mention in the next section has to be taken together with the information of the initial conditions to be able to extract a global picture of the collision.

Finally, two words of caution are needed. First, the main uncertainty in Bjorken's model lies in the theoretical estimation of τ_o. The common approach is to take $\tau_o = 1$ fm on the grounds that this is the typical hadronic formation time obtained from string fragmentation models. However it is yet not clear that one can speak of thermalization already at such short times, and there are authors who prefer a somewhat larger τ_o, up to ~ 2 fm (see [30] for a comparison of the values of ϵ_o for different τ_o scenarios). Second, the naive geometrical model shown in Figure 1.3 does not include re-scattering of the secondaries in the interaction region. Such an effect has proved to be an important contribution to the final energy distribution [32, 33].

Transverse momentum.

The $d\sigma/dp_t$ distribution is sensitive to initial and final state interactions, and can shed light on the mechanisms at play in the collision. There are two striking differences between the charged particle p_t distributions in p-p and A-A collisions. In the nuclear case $d\sigma/dp_t$ shows an enhancement both at low p_t ($p_t <$0.2 GeV/c) and at high p_t ($p_t >$ 1 GeV/c), the Cronin effect, with respect to the result in p-p collisions[2)] [34]. Figure 1.4 shows the ratio of $d\sigma/dp_t$ of different nuclear systems to p-p interactions as an example of these results (the dotted line is just to guide the eye). Note that there is no appreciable rapidity dependence except in the very low p_t region.

The explanation of these effects is still controversial. The ideas put forward to explain the low p_t enhancement range from phase space considerations [35], rescattering and cascading of secondaries in the target nucleus to resonance decays (mainly N* and Δ^{++}) [36]. The suggestions to explain the Cronin effect concentrate on considering initial-state low-momentum scattering of partons [37].

A variable which is commonly used in the analysis of data on individual particle species is the transverse mass, $m_t = (p_t^2 + m^2)^{1/2}$. The use of m_t is introduced since the production cross section of a given particle type can be well described as an exponential in m_t,

2) In p-p collisions the $d\sigma/dp_t$ distribution can be parameterized as an exponential up to $p_t \sim 1$ GeV/c. For higher p_t the onset of hard QCD scattering calls for a power law parameterization.

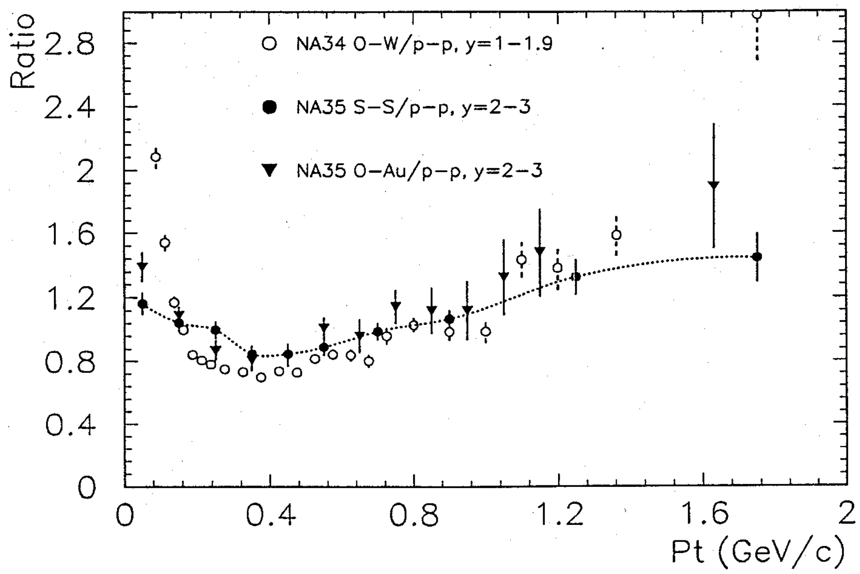

Figure 1.4: Ratio of the p_t distribution of A-A to p-p collisions (the dotted curve is to guide the eye).

$(1/p_t)(d\sigma/dp_t) \propto exp(-m_t/T)$. In the case of p-p collisions at ISR energies the slope parameter T is common for the different particle types, $T \sim 120$ MeV, while for heavy ion collisions the slope parameter increases with the mass of the particle. While it is not clear how to interpret the seemingly thermal behaviour in p-p interactions, in the case of heavy ion collisions the m_t spectra can be understood by assuming that a thermalized system is formed. In this scenario the m_t spectra is a convolution of both the degree of thermalization achieved in the collision and the transverse flow [38]. Therefore the value of T extracted directly from a fit of the data to $exp(-m_t/T)$ does not reflect the temperature of the fireball: the effect of the radial expansion has to be subtracted to obtain a meaningful value for the temperature. Data from NA44 [39] suggest a "real" temperature of 140 MeV and an average radial flow velocity β of $\langle\beta\rangle = 0.42$.

Additional information on the size of the system providing independent evidence of transverse flow can be extracted from interferometric studies as described in the next section.

Bose-Einstein interferometry:

Boson interferometry is used to extract information about the size of the emitting source. The method is based on the well known Handbury-Brown-Twiss (HBT) effect concerning the emission of bosons from a thermalized incoherent source [40]. Bosons tend to be produced in the same quantum state and, therefore, the emission of like-momentum pions from the fireball is favoured. For a static source, the evaluation of the two-pion symmetrized wave function leads to an interference term proportional to $cos(p_1 - p_2)(r_1 - r_2)$ and thus, in principle, by measuring the momentum of correlated pions we can deduce the size $|r_1 - r_2|$ of the emitting source. Data is usually analyzed in terms of a correlation function and an assumption on the shape of the emitting source [41]. The correlation function is defined as the ratio of the two-particle cross section to the product of the two single-particle cross sections. The source size is commonly taken as being gaussian or exponential and it is parameterized in terms of a transverse and longitudinal "size" parameters. From an experimental point of view the analysis of HBT data is difficult for a variety of reasons: the system is not static but expanding, there is contamination from resonance decays and there might be rescattering of the species used with each other or within the rest of the system which destroy the original correlation. For an expanding source we are actually getting information of a "homogeneity" scale from which particles with similar momentum are emitted.

Several experiments have used this method to measure the size of the fireball. We must note that the information we can extract by pion interferometry concerns the hadronic phase: we are seeing the size of the system at hadronization time, after some expansion has taken place. The results both from the CERN SPS (NA35 [42], NA44 [43] and WA80 [44]) and from the AGS at BNL (E814 [36] and E859 [45]) show that indeed a "big" system, with a transverse dimension greater than the geometrical dimensions of the beam nucleus, $R_\perp \geq$4-6 fm, is reached in heavy ion collisions .

1.3.2 QGP signatures.

Strangeness enhancement.

An enhancement of the strange-particle yield in A-A collisions with respect to that in p-p or p-A has been proposed as a clear signature of QGP formation [46]. The production of $s\bar{s}$ pairs is energetically favoured in a QGP with respect to a hadron gas. In the latter case the formation of strange particles has to proceed through the collision of non-strange hadrons with relatively high thresholds.[3)] In QGP the production of a $s\bar{s}$ pair takes $2m_s \sim 300$ MeV, closer to the expected temperatures of the plasma. Even if we consider the case of high stopping, where the QGP is produced in a baryon-rich environment, the chemical potential of the u and d quarks favours the production of s quarks, giving rise to an enhanced production of open-strange hadrons, mainly Ks and Λs but also Ωs and Ξs.

There are several experiments both at the AGS (E802, E810) and at the SPS (NA35, NA36, WA85) measuring strangeness production in heavy ion collisions . Typically, K/π and strange baryon to antibaryon ratios ($\Lambda/\bar{\Lambda}$, $\Xi/\bar{\Xi}$) are measured as they provide information on the production mechanism and possible thermal origin of the strangeness yield [47].

A consistent enhancement, up to a factor of 3, of strangeness production has been found by the mentioned experiments [48, 49, 50, 51, 52] when going from p-p to central A-A collisions.

3)The lowest threshold reaction is $p + n \rightarrow \Lambda + K + n$ which requires 671 MeV. The production of a $K\bar{K}$ pair requires 986 MeV.

However these results can be also explained by a hot thermalized hadron gas in chemical equilibrium if one includes rescattering of the produced particles among themselves or in the surrounding matter. The space-time evolution of the system plays then a crucial role in the prediction of the strangeness yield of both phases, and the uncertainty in τ_o mentioned above makes it difficult to extract unambiguous conclusions from the observed enhancement[4)]. What seems to be a clear message from the measured strangeness enhancement is that a hot (probably thermalized) fireball is formed. The enhancement can not be explained by assuming just a superposition of p-p collisions, supporting the same evidence from other signatures.

ϕ enhancement.

The same arguments which we advanced to justify the expectation of an increased strangeness yield by QGP can be used to advocate an increased ϕ production in the plasma [53]. ϕ production in p-p collisions is suppressed by the OZI rule[5)]. On the other hand, strange-quark abundance in the QGP can get close to saturation, making it likely for a s quark to join a $\bar{s}$ at hadronization time to form a ϕ meson. This mechanism of ϕ production will not be OZI suppressed and the ratio of ϕ to non-strange mesons is then expected to be several times larger than that found in p-p collisions.

The first results on this topic were published by the NA38 collaboration [55, 56] and indicate an increase of the ϕ production of about a factor of 3 when going from $p-U$ to $S-U$ collisions, while the $\rho+\omega$ peak shows no significant increase. However these data were obtained with a quite high p_t cut ($p_t > 1GeV$) and at forward rapidities. Though one can invoke a QGP scenario to explain this effect, more conventional (purely hadronic) scenarios, based on final state rescattering, have been proposed that can account for this result [57, 58].

Another interesting issue still in need of experimental input is whether the ϕ can convey information from the early stage of the hadronization process. Since in vacuum the ϕ has a small cross section (<10 mb) of scattering with non strange hadrons and has a lifetime of 45 fm/c, it is usually assumed that, once produced from the hadronization of QGP, it can leave the interaction region essentially without further rescattering. This would provide a unique hadronic window to the conditions of the system at hadronization time. However, recent calculations of the ϕ mean free path , λ_ϕ, based on kinetic theory [59] show that in hot hadronic matter λ_ϕ is a strongly decreasing function of temperature, reaching the typical transverse size of the fireball (~10 fm) at a temperature of about 170 MeV. It is thus likely that the ϕ mesons produced at hadronization time, while the fireball is still close to T_c, will rescatter and thermalize in the medium before having the chance of leaving the interaction zone, thus reflecting a somewhat lower temperature than T_c. This could explain the low

[4)]However some authors consider the fireball lifetime and temperature that one has to use for a hadron-gas origin of the enhancement somewhat too high for what is commonly assumed for the hadronic phase [106].

[5)]The OZI rule states that processes which involve non connected quark diagrams are suppressed [54]. The hadronic production of an $s\bar{s}$ has to proceed through three gluons and, therefore, being an α^3 order process is strongly suppressed.

freeze-out temperature deduced from the strange to non-strange meson ratios, $T \sim 120$ MeV, in comparison with transition temperatures of the order of 200 MeV [60].

J/ψ suppression.

The prediction that J/ψ production should be suppressed in the QGP is based on the screening of the $c\bar{c}$ binding potential by the free gluons moving in the deconfined medium [61]. This is an effect similar to Debye screening in QED. In a hot unconfined medium, any produced $c\bar{c}$ pair will dissolve. At hadronization time, the single c and $\bar{c}$ quarks will coalesce with the more abundant u and d, giving rise to open-charm mesons and to a suppression of the resonant $c\bar{c}$ system. The effect is expected to be more pronounced at low p_t, since high p_t $c\bar{c}$ pairs can leave the fireball before the c and the $\bar{c}$ have spatially separated by the confining radius of the bound state, and therefore the J/ψ can be formed outside the interaction region.

The measurement of J/ψ suppression in S+U and O+U collisions by NA38 [62] as early as 1987 triggered a lot of expectation and also a lot of theoretical work on the subject. The main aim of the theoretical effort has concentrated in the extensive study and modeling of the J/ψ production and rescattering in a dense hadronic system. As a result several models have been proposed which explain J/ψ suppression in a hadronic scenario: destruction through rescattering with comoving produced hadrons [63, 64] or through absorption by spectator nucleons [65].

Summary:

From the results collected so far a coherent picture of heavy ion collisions is starting to emerge where it seems clear that a hot and dense system in thermal equilibrium is formed already at SPS energies with the beams used to date. The behaviour of m_t and HBT studies suggest that the system reaches thermal and chemical equilibrium and that at freeze-out it has undergone radial expansion. This picture is further supported by the measured strangeness enhancement and J/ψ suppression. Whether these are the effects of QGP formation or just those form a hot hadron gas is still not clear since the above-mentioned effects can be reproduced from rescattering and/or absorption in the dense interaction region, without invoking new phenomena.

Lacking definite, unambiguous theoretical predictions on QGP formation, the experimental approach to the understanding of heavy ion collisions relies heavily on the nucleon–nucleon results for comparison. The experimental results on any observable are compared to the expected yield from known hadronic processes scaled with multiplicity, assuming that nucleus–nucleus collisions are just a mere superposition of constituent nucleon–nucleon interactions. Any new physics will manifest itself as a deviation from this simple picture.

1.4 Dileptons as a probe of relativistic nuclear interactions.

The production of lepton pairs in heavy ion collisions is the subject of the present work and will be dealt with at large in the next chapter. Here we will point out the main features of dilepton production which make it one of the most interesting probes of the dynamics of the interaction [66].

The main feature that makes dileptons an unique probe of the nuclear collision dynamics is their electromagnetic character. Their mean free path is much larger than the typical dimensions of the fireball, and they can thus leave the interaction region unaffected by further rescattering, transporting information of the properties of the system at the time they are emitted. We can easily perform an order-of-magnitude estimation of the mean free path of dileptons inside quark matter with the use of a simplified model for the fireball. Assuming a static gas of quarks at T=200 MeV and recalling the standard thermodynamic methods, we find that the mean free path of an electron in such a system is $\lambda \propto \alpha^{-2}(m_q T)^{-1/2} \sim 10^3$ fm [67, 68]. This is several orders of magnitude bigger than the typical transverse dimensions of the fireball formed in the collision, which initially is given by the size of the beam nucleus (3.6 fm for a ^{32}S nucleus).

Second, dileptons are produced throughout the whole space-time evolution of the collision by different processes, providing a window to the several stages the interacting system goes through.

As we will mention in detail in Section 2.3.1, another crucial feature of dilepton production in heavy ion collisions is their ability to reflect the initial temperature of the fireball. Dileptons can be emitted as thermal radiation from the QGP phase through $q\bar{q} \to \ell^+\ell^-$ and from the hadronic phase by pion annihilation, $\pi^+\pi^- \to \ell^+\ell^-$[6]. Since this thermal radiation is proportional to T^4, it will be most abundantly produced at the early stages of the interaction when the temperature of the system reaches its highest value. Therefore dileptons can be an important (even dominant) contribution to the total dilepton yield if sufficiently high initial temperatures are reached.

Finally, dileptons give us the chance to measure the vector mesons through their electromagnetic decays into $\ell^+\ell^-$. In particular the properties of the ρ meson are expected to be modified in a detectable way due to partial restoration of chiral symmetry in the dense fireball. Additionally, the total ρ yield can as well serve as a measure of the fireball lifetime [69]. And we have already mentioned that a ϕ enhancement with respect to the scaled p-p production can be an indication of QGP formation. We will return to these topics in more detail in Chapter 2 Section 2.3 below.

---

[6]Along with real photons. However, from the experimental point of view, the detection of direct photons from the fireball suffers from a much higher background than the dilepton case.

1.5 The dilepton programme at CERN.

There are three experiments dedicated to the measurement of dilepton pairs in nucleus–nucleus collisions at SPS energies: CERES, HELIOS and NA38. I will briefly describe here the main features of HELIOS and NA38 since their results, along with those of CERES, provide the main input to our current understanding of dilepton production in heavy ion collisions.

HELIOS [70] has undertaken a systematic study of dilepton production in both p-p and A-A collisions since its first data taking period back in 1986. The first experiment (HELIOS-1) investigated dilepton (both e^+e^- and $\mu^+\mu^-$) production in p-Be collisions at 450 GeV/c [71]. The continuation of HELIOS-1, HELIOS-2 and HELIOS-3, concentrated in $\mu^+\mu^-$ production in nuclear collisions with a ^{32}S beam. It consists of a muon spectrometer composed of an absorber and MWPC for muon tracking, covering the dimuon invariant masses $m_{\mu^+\mu^-} < 4$ GeV/c^2 at forward rapidities, $\eta > 3.5$.

NA38 [72] is the continuation of the experiment NA10 measuring dimuon production in pion induced interactions. NA38 has been upgraded to study dimuon production in nuclear interactions. It also uses an absorber and MWPC for muon detection. In addition it has an electromagnetic calorimeter for the measurement of the transverse energy. It covers the rapidity region $2.8 < \eta < 3.5$ and the medium-high invariant mass range $\sim 1 < m_{\mu^+\mu^-} < 4$ GeV/c^2 [73], but concentrates mainly in the study of J/Ψ and Ψ' suppression.

1.6 The CERES physics programme.

CERES (**Ce**renkov **R**ing **E**lectron **S**pectrometer) [74] is the only experiment devoted to the systematic study of low mass ($\sim 0.1 < m_{e^+e^-} < 1.5$ GeV/c^2) e^+e^- pairs produced at mid rapidity in nucleon-nucleon, nucleon–nucleus and nucleus–nucleus collisions at the CERN SPS. The CERES spectrometer has been specifically designed to cope with the inherent difficulty of such a measurement: an extremely weak dilepton yield ($\sim 5 \times 10^{-5}/\pi^o$) has to be detected among an overwhelming combinatorial background which stems from the π^o Dalitz decay and γ conversions. The spectrometer is based on two RICH (Ring Imaging CHerenkov) detectors and its concept allows to achieve a maximum rejection of the mentioned background sources while allowing its operation in the high multiplicity environment of heavy ion collisions. A detailed description of the spectrometer is given in Chapter 3.

The main topic that CERES addresses is the search for a thermal signal from QGP or from the hot and dense hadronic system expected to be formed in nuclear collisions. In addition CERES can also study the vector mesons ρ, ω and ϕ through their direct decays into e^+e^- as described in Chapter 2.

Direct photons can also be measured with CERES through their conversion into an e^+e^- pair, using the target as a converter. Like all electromagnetic probes they can provide information about the temperature achieved in the early stages of the collision. See [75] for the CERES results on real photon production in S–Au collisions at 200 GeV/c.

High-p_t pions can be identified in the CERES RICH detectors by their non-saturated ring radius. The pion p_t spectrum is sensitive to the degree of thermalization achieved in the collision and can also carry information about the collective transversal flow in the interaction region [76].

Finally, CERES can use very peripheral collisions to study e^+e^- pairs produced by the strong electric fields created during the collision [77]. The cross section for this process is very large as it scales as e^4 and, thus, in the case of two nuclei as $(Z_1Z_2)^2$.

This thesis presents the result of my analysis of the data on low–mass e^+e^- pair production in ^{32}S – ^{197}Au collisions at 200 GeV/nucleon taken by CERES in the spring of 1992.

Chapter 2

Sources of dileptons in hadronic and nuclear collisions

In this chapter I will review the current understanding of dilepton production in hadronic and nuclear collisions. As we are interested in detecting new dilepton sources in nuclear interactions (thermal emission or dense-medium effects in the production and decay of hadrons) which are not present in hadronic interactions, a complete understanding of the mechanisms which contribute to the dilepton spectrum in p-p collisions is therefore essential. Furthermore the cross sections, branching ratios and form factors used in predicting the dilepton yield expected in nuclear interactions are drawn from our current understanding of hadronic interactions.

2.1 Electron pair production in nucleon–nucleon collisions

The dilepton spectrum from the decay of known hadronic sources forms the physical background in the study of e^+e^- emission in nuclear collisions. In the next sections we will mention the most important sources of dileptons in the mass range relevant to CERES, also mentioning for the sake of completeness the Drell-Yan mechanism and the semi-leptonic heavy flavour decays, although they are expected to contribute at somewhat higher invariant masses than the mass range covered by CERES.

We will concentrate from now on in electron pair production. Most of the processes and production mechanisms that we will mention hold also for dimuons, but there are slight differences[1)] which will render a generalization inadequate.

[1)]For example a π^o Dalitz decay to dimuons is inexistent. Also bremsstrahlung and background considerations from K decays need a different treatment in the muon case.

2.1.1 e^+e^- pairs from hadron decays

The main sources of e^+e^- pairs in hadronic collisions are the electromagnetic decays of hadrons and resonances produced in the interaction. The main processes are the Dalitz decays of the η, η', ω and π^o,

$$\eta,\ \eta',\ \pi^o \rightarrow e^+e^-\gamma \qquad\qquad \omega\ \rightarrow\ \pi^o e^+e^- \tag{2.1}$$

which will populate the region of low invariant masses, $M_{e^+e^-} \leq 1\,GeV$, and the decays of the vector mesons ρ, ω and ϕ,

$$\rho,\ \omega,\ \phi \rightarrow e^+e^- \tag{2.2}$$

which will produce the typical resonance shape in the invariant mass plot around $m_{\rho,\omega} = 0.8$ GeV/c^2 and $m_\phi = 1$ GeV/c^2.

Dalitz decay modes

In general, the processes from (2.1) are meson decays of the type A$\rightarrow$Bγ^* with a further conversion of the virtual photon into an e^+e^- pair as shown in figures 2.1 and 2.2. CP conservation allows only transitions of the type vector(pseudo-scalar) $\rightarrow$ pseudo-scalar(vector) plus γ or pseudo-scalar $\rightarrow 2\gamma$. The matrix element for this kind of transitions can be factorized into a transition matrix for the process A$\rightarrow$Bγ^*, $\mathcal{M}^\mu_{A\rightarrow B\gamma^*}$, times an elementary QED matrix element, $\mathcal{L}_\mu$. The transition amplitude is also trivial up to a form factor, f_{AB}, which takes into account the fact that the hadrons involved are not elementary particles. Thus we have (see for example [78], [79]),

$$\mathcal{M}_{A\rightarrow Be^+e^-} \;=\; ie^2\,\mathcal{M}^\mu_{A\rightarrow B\gamma^*}\,\frac{1}{q^2}\,\mathcal{L}_\mu \tag{2.3}$$

where

$$\mathcal{M}^\mu_{A\rightarrow B\gamma^*} \;=\; f_{AB}(q^2)\mathcal{E}^{\alpha\beta\gamma\mu}p_\alpha q_\beta \epsilon_\gamma \tag{2.4}$$

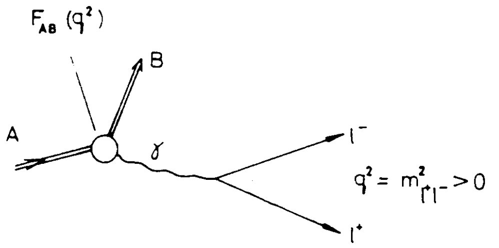

Figure 2.1: Dalitz decay of the type Vector(Pseudoscalar) $\rightarrow$ Pseudoscalar(Vector) e^+e^-

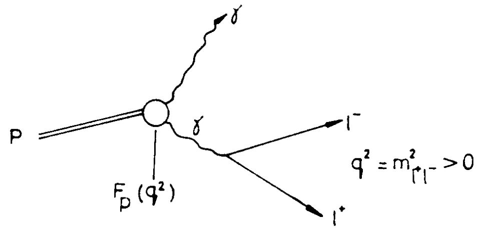

Figure 2.2: Dalitz decay of the type Pseudoscalar $\rightarrow\ \gamma\, e^+e^-$

and

$$\mathcal{L}_\mu = \bar{u}(k)\gamma_\mu v(k') \quad or \quad \mathcal{L}_\mu = \epsilon_{\lambda\mu}(q^2) \tag{2.5}$$

the second case in (2.5) corresponding to particle B being a photon. The notation is as follows: q_β is the 4–momentum of the virtual photon, $q^2 = m^2_{e^+e^-}$, p_α the 4–momentum of particle B, ϵ_γ the polarization vector of the vector meson involved and $\mathcal{E}^{\alpha\beta\gamma\mu}$ the totally antisymmetric unit tensor. The index λ in $\epsilon_{\lambda\mu}$ takes into account the polarization of the final state real photon and one has to sum over its two possible values.

From these amplitudes we can obtain the differential decay rate into lepton pairs with invariant mass $q^2 = m^2_{e^+e^-}$ from hadron decays. The elementary QED conversion rate was first calculated by N. M. Kroll and W. Wada [80]. In the case of composite particles this result gets modified by the form factor of the decaying particle. It is usual to normalize the decay rate to the corresponding one when the photon is real, $\Gamma(A \to B\gamma)$, given by

$$\Gamma(A \to B\gamma) = \frac{1}{4\pi}\frac{(m_A^2 - m_B^2)^3}{8m_A^3} \times |f_{AB}(0)|^2 \tag{2.6}$$

Thus

$$\frac{d\Gamma(A \to Be^+e^-)}{dm_{e^+e^-}\Gamma(A \to B\gamma)} = \frac{\alpha}{3\pi}\frac{1}{m_{e^+e^-}}\sqrt{1 - \frac{4m_e^2}{m^2_{e^+e^-}}}\left(1 + \frac{2m_e^2}{m^2_{e^+e^-}}\right) \times \left[\left(1 + \frac{m^2_{e^+e^-}}{m_A^2 - m_B^2}\right)^2 - \frac{4m_A^2 m^2_{e^+e^-}}{(m_A^2 - m_B^2)^2}\right]^{3/2} |F_{AB}|^2 \tag{2.7}$$

and

$$\frac{d\Gamma(A \to e^+e^-\gamma)}{dm_{e^+e^-}\Gamma(A \to \gamma\gamma)} = \frac{2\alpha}{3\pi}\frac{1}{m_{e^+e^-}}\sqrt{1 - \frac{4m_e^2}{m^2_{e^+e^-}}}\left(1 + \frac{2m_e^2}{m^2_{e^+e^-}}\right)\left(1 - \frac{m^2_{e^+e^-}}{m_A^2}\right)^3 |F_A|^2 \tag{2.8}$$

where the F's are defined as

$$\left|F_{AB}(q^2)\right|^2 = \frac{|f_{AB}(q^2)|}{|f_{AB}(0)|} \tag{2.9}$$

The form factors can be measured experimentally by simply comparing the observed cross section for the mentioned processes to the known QED cross section of the equivalent elementary process. But one would prefer to have some model based on the underlying physical picture of the decay process to predict the value and behavior of $|F|^2$. Such models exist, the simplest of them being the Vector Meson Dominance model (VMD) [81, 82, 83] which we will briefly discuss below. For other models see [79] and references therein.

Vector Meson Dominance model

The VMD model takes advantage of the fact that there are several vector mesons with the same quantum numbers as the photon, that is, $J^{PC} = 1^{--}$ and Q=B=S=0. The lowest mass hadronic states with these characteristics are the ρ, the ω and the ϕ. The basic assumption of the VMD model is that photon–hadron interactions proceed through the photon turning into one of these mesons, which in turn interacts with the target hadron, as schematically shown in Figure 2.3. In other words, the hadronic current in Figure 2.3 is

$$J_\mu = \sum_V \frac{e\, m_V^2}{2g_V} V_\mu \tag{2.10}$$

where the sum runs over all the relevant vector mesons, for example V= ρ, ω, ϕ, and g_V plays the role of a coupling constant to be determined from experiment. The m_V^2 is introduced in (2.10) to keep the coupling constants dimensionless.

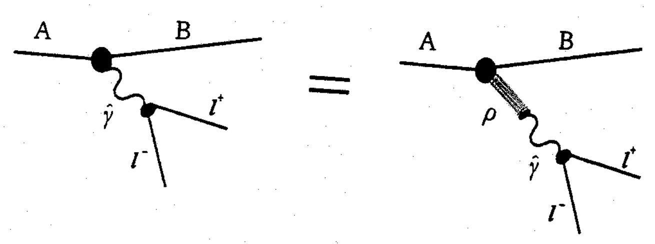

Figure 2.3: VMD model of coupling of hadrons to photons

The VMD model provides thus a framework to calculate transition form factors from an underlying physical picture. The form factors are now expressed in terms of the (unspecified by the model) coupling constants g_V,

$$F_{AB}(q^2) = \sum_i \frac{g_{V_i}}{g_{V_1} + g_{V_2} + \dots} \frac{m_{V_i}^2}{\left(m_{V_i}^2 - q^2 + i m_{V_i}\Gamma_{V_i}\right)} \tag{2.11}$$

The coupling constants can be estimated using the quark model or by fitting to the data [78].

Despite its simplicity the VMD model agrees reasonably well with the experimental data. Figure 2.4 shows the prediction of the VMD model for the η form factor compared to the available data [79]. There are still some open questions like the failure of the VMD model to account for the ω form factor for masses $m_{e^+e^-} \geq 0.2$ GeV. This is shown in Figure 2.5 where the VMD prediction is shown as a dashed line (curve 3). The full line is a pole-fit to the experimental data and the curves 2 and 4 have been obtained from a modified ρ propagator and with the non-local quark model respectively (see references in [79] for details). Experimentally the data is scarce: only one experiment has measured this form factor in the time-like region [84].

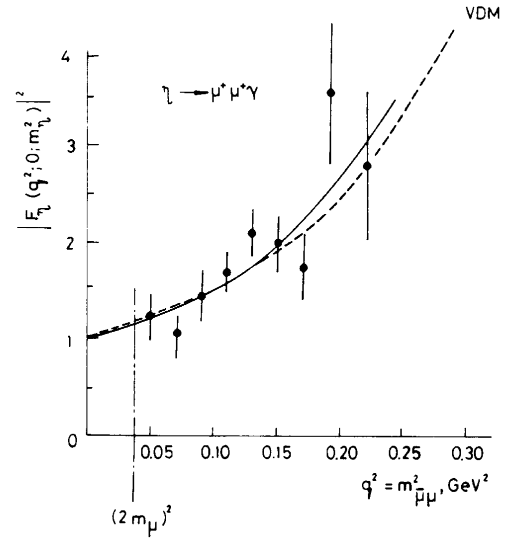

Figure 2.4: Form factor of the η as predicted by the VMD model (dashed line) compared with a pole-fit (full line) of the available data.

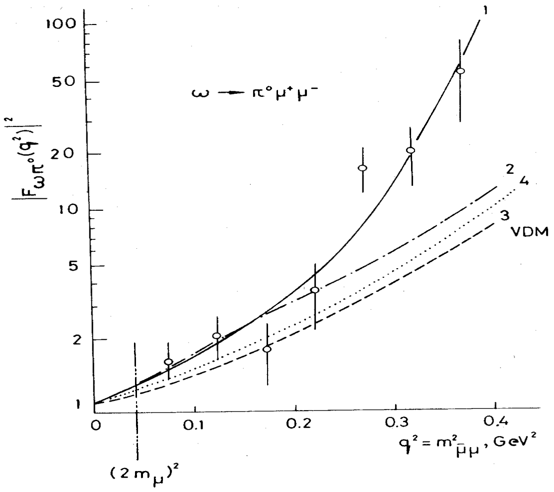

Figure 2.5: Form factor of the ω as predicted by the VMD model (dashed line) compared with the available data. See the text for details on curves 1, 2 and 4.

2.1.2 e^+e^- production through Drell-Yan annihilation

Apart from the valence quarks that carry its quantum numbers, a hadron is composed of a *sea* of virtual quark-antiquark pairs and gluons that play a role in hadronic interactions. A confirmation of the existence of such sea of virtual particles within hadrons is the production of dileptons through the Drell-Yan (DY) process [85], which is an important contribution to e^+e^- production in high energy hadronic collisions. The DY mechanism to leading order is shown in Figure 2.6. A quark from hadron A annihilates with an antiquark from hadron B giving rise to an e^+e^- pair.

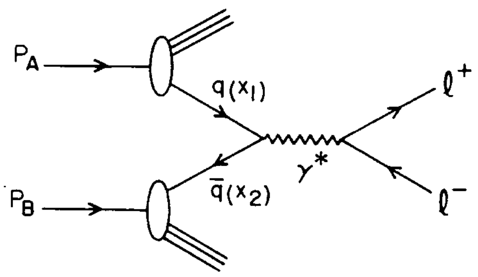

Figure 2.6: Lowest order lepton pair production through the Drell-Yan process.

The cross section of such a process as a function of the e^+e^- pair invariant mass is given by (see for example [86, 87])

$$\frac{d\sigma}{dM^2}(AB \to e^+e^-X) = \frac{4\pi\alpha^2}{9M^4}\sum_q e_q^2 \int_0^1 dx_a \int_0^1 dx_b \, [f_A^q(x_a)\, f_B^{\bar{q}}(x_b) + f_A^{\bar{q}}(x_a)\, f_B^q(x_b)] \times \delta\left(1 - x_a x_b \frac{s}{M^2}\right) \quad (2.12)$$

where we identify the first factor in the *r.h.s.* of (2.12) as the first order QED cross section for the elementary process $q\bar{q} \to e^+e^-$. The expression under the sum takes into account the structure of the interacting particles: x_i is the fraction of the hadron momentum carried by the interacting parton, $p_{parton} = x_i\, p_{hadron}$ and the structure function $f(x_i)$ represents the probability of finding a parton with momentum fraction x_i within the interacting hadron. $M^2 = (p_q + p_{\bar{q}})^2 = (x_a p_A + x_b p_B)^2$ and e_q is the electric charge of quark q.

The process shown in Figure 2.6 is second order in the electromagnetic coupling constant α, but zeroth order in α_s. A complete treatment of the DY process should include higher QCD corrections at the $q\bar{q}\,\gamma$ vertex [88]. For high energies and high pair invariant masses ($M > 2\,GeV/c^2$) the QCD corrections can be reliably calculated as a perturbation to the main diagram of Figure 2.6. However for lower pair invariant masses the α_s-order corrections calculated with perturbative QCD can give a sizeable contribution, rendering the perturbative method unreliable.

One can parametrise the parton distribution functions $f(x_i)$ to get a somewhat more useful form of equation (2.12) directly comparable with experimental results. Equation (2.12) can be rewritten as [15]

$$\left.\frac{d^2\sigma}{dM\,dy}\right|_{y=0} \sim \frac{1}{M^3}\left(\frac{M}{\sqrt{s}}\right)^A e^{-M/T_{DY}} \quad (2.13)$$

where A and T_{DY} absorb the parametrisation "constants" used in $f(x_i)$. Actually, both A and T_{DY} depend on M^2. This provides a good account of the experimental results, which can be fitted as [78]

$$\left.\frac{d^2\sigma}{dM\,dy}\right|_{y=0} = 3 \times 10^{-32}\frac{1}{M^3}e^{-15M/\sqrt{s}} \quad (2.14)$$

The Drell-Yan contribution to low masses ($M \leq 1\,GeV/c^2$) is not reliably calculable within perturbation theory. In any case it is thought to be negligible with respect to the much stronger yield from hadron decays and possibly thermal pairs in this mass range. Drell-Yan is a sizeable contribution above masses $M \sim 2\,GeV/c^2$, where it only competes with e^+e^- from heavy flavour decays.

In the case of an interaction between two nuclei of mass numbers A and B respectively, the Drell-Yan yield is expected to scale as [15, 89]

$$\frac{d^2\sigma_{DY}^{AB}}{dM\,dy} = AB\frac{d^2\sigma_{DY}^{nn}}{dM\,dy} \tag{2.15}$$

2.1.3 Heavy flavour decay into e^+e^-

We mention briefly the contribution to e^+e^- production from heavy flavour decays just for completeness as it is not relevant in the mass range accessible to CERES.

Charm production in nucleon–nucleon collisions proceeds through the processes

$$q\bar{q} \rightarrow c\bar{c} \qquad\qquad gg \rightarrow c\bar{c} \tag{2.16}$$

The further fragmentation of the $c\bar{c}$ system gives rise to open charm production, a $D\bar{D}$ pair. The semi-leptonic decays of the D and $\bar{D}$ will produce uncorrelated e^+e^- pairs in a wide range of the dilepton invariant mass, following an exponential distribution. However, due to the high mass of the D and despite that the final e^+e^- pair will carry only a fraction of the invariant mass of the parent system, the contribution from the processes (2.16) is negligible below masses $m_{e^+e^-} \sim 1$ GeV/c^2.

Estimates of the heavy flavour cross sections in p–p collisions and dilepton invariant mass distributions from heavy flavour decays are given in [90, 128].

2.2 Dilepton production in hadronic collisions: present status.

Our current understanding of dilepton production in hadronic collisions rests in the sources mentioned in Section 2.1 above. The claim by several experiments in the late 70's and during the 80's [92, 93] that an anomalous excess of low mass dileptons over the conventional hadronic sources had been observed, has been superseded by recent HELIOS/1 data [94] and confirmed by CERES [95]. Early experiments on the subject suffered from the poorly known values of the cross sections and kinematical distributions of the resonances involved, mainly the η. New data from NA27 [96] and HELIOS/1 [94] itself have allowed a more precise study of dilepton production in p-p collisions. One of the interesting aspects of HELIOS is that it has measured directly the η Dalitz decay contribution to the dilepton spectrum. This method avoids using the η production cross section and reduces the final uncertainty in the expected hadronic yield. Figure 2.7 shows the HELIOS/1 data (black dots) on e^+e^- production on p-Be collisions at 450 GeV/c. The plot shows also the expected contribution from the individual sources as well as the summed yield. Uncertainties in the total yield are indicated as the shaded area which represents the $\pm 1\sigma$ errors on the summed contributions, stemming from the errors on the production cross sections of the individual processes.

The HELIOS/1 data indicate that there is no need to call for any new source of e^+e^- pairs in p-p collisions with a 90% confidence level within the present level of 50% uncertainty. Preliminary results from CERES on p-Be at the same energy confirm this conclusion (see Chapter 4). The ongoing data analysis of CERES data on p-Be taken in conjunction with the TAPS calorimeter [97] is expected to reduce the uncertainty of HELIOS data through a more precise measurement of the η production cross section.

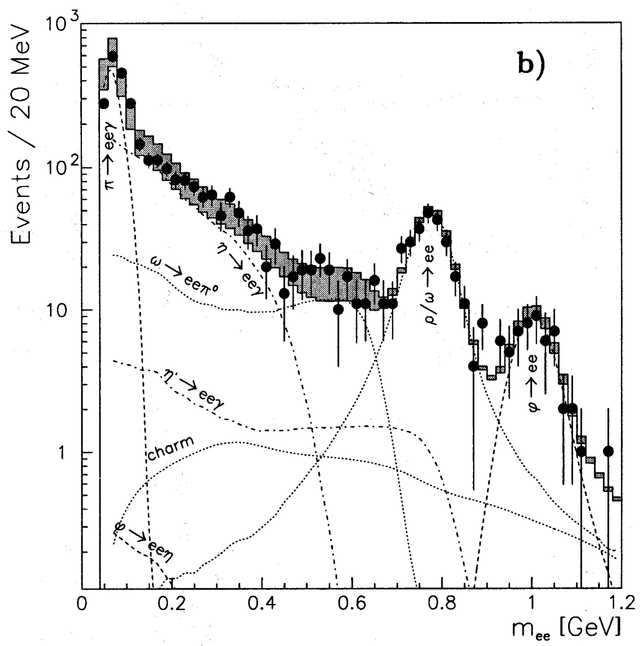

Figure 2.7: Results on e^+e^- production in p-Be interactions from HELIOS/1 collaboration. The data is compared to the predicted yield from the conventional hadron sources.

2.3 Dilepton production in nuclear collisions

We turn now to the issue of dilepton production in nucleus–nucleus collisions. We expect that in addition to the sources mentioned in the previous section, we will have dilepton emission through thermal radiation from the hot fireball formed in the interaction and through bremsstrahlung of its constituents. The dilepton spectrum from nuclear collisions can be further distorted by the modification of the hadronic parameters (mass and decay width) in the dense medium as the system approaches the phase transition restoring chiral symmetry. These three additional sources of dileptons render heavy ion collisions a unique way of studying dense nuclear matter.

Time evolution of a nucleus–nucleus collision.

Electron-positron pairs are emitted throughout the whole space-time evolution of the nuclear interaction, with different processes contributing to the e^+e^- yield at different phases of the interaction. Figure 2.8 shows the evolution in the CM frame of the interaction between two relativistic nuclei in the z-t plane, as well as the temperature evolution of the fireball formed in the collision as a function of time. Both figures assume the following scenario: initial formation of QGP at a temperature T_o, expanding and cooling, a first order phase transition to hadronic matter (hadron gas) at a temperature T_c, and further cooling of the produced hadrons until the decoupling (freeze-out) temperature T_f[2)].

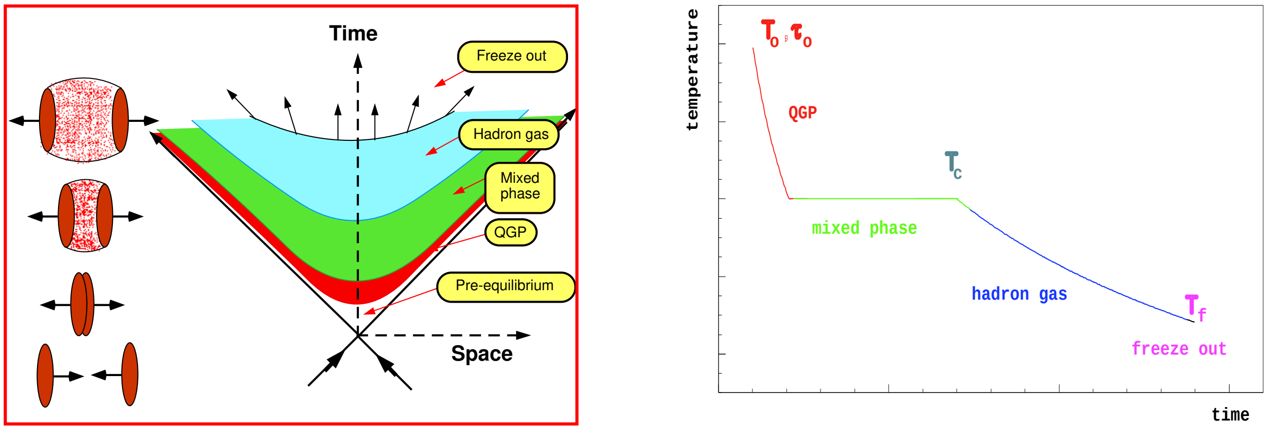

Figure 2.8: The space-time (left) and temperature (right) evolution of a nucleus-nucleus collision.

If we follow in this way the interaction we can distinguish the following dilepton sources: In a first stage, the two nuclei approach each other essentially at the speed of light as two Lorentz-contracted pancakes in the direction of motion. Dileptons are produced here by the inelastic nucleon–nucleon scattering through the Drell-Yan mechanism. Also heavy flavour mesons $(D, \bar{D})$ are produced at this stage, which will give rise to uncorrelated e^+e^- pairs from their decays. As these are hard processes, the resulting dileptons will typically populate the high invariant mass zone of the spectrum, $M \geq 1.5\, GeV/c^2$.

The strong interaction between the nucleons within the incoming nuclei creates a dense region of colour strings stretched between the participant partons. The fragmentation of such color strings results in copious production of quark-antiquark pairs, creating a dense and hot system of quarks and gluons, a quark-gluon plasma (QGP). This system expands and cools down, reaching a critical temperature T_c, where the QGP starts to hadronize into a hot interacting gas of hadrons. At this stage both phases– the QGP and the hadron gas– may coexist.

[2)]If in the initial stage the deconfining temperature T_c is not reached, the interaction will proceed directly through a dense interacting hadronic gas which will expand and cool until a decoupling temperature T_f, after which the hadrons will expand freely.

e^+e^- pairs are emitted as thermal radiation during the expansion and cooling stages of the QGP phase by $q\bar{q}$ annihilation and in the hadron phase by $\pi^+\pi^-$ annihilation. In addition, bremsstrahlung emission ($q\bar{q} \to q\bar{q}\ e^+e^-$ in the QGP and $\pi^+\pi^- \to \pi^+\pi^-\ e^+e^-$ in the hadron gas) contributes to the very low mass region of dileptons.

Once the hadronization is complete, the hadron gas will expand and cool down until it reaches the freeze-out temperature, where the hadrons cease to interact and decouple, undergoing free expansion from this point on. After the decoupling time, an amount of additional e^+e^- pairs is emitted through the electromagnetic decays of long lived resonances, mainly low mass vector mesons and π^o Dalitz decays.

In principle, the experimental measurement of the dilepton yield in nuclear collisions would allow to study the time evolution of the interaction by identifying the different dilepton sources just mentioned. In order to do that one must calculate the relative strength of each process to obtain a total expected yield to compare with the measured one. This involves the use of a model for the complete space-time evolution depicted in Figure 2.8. The approach to thermalization and phase transition to QGP, and the further hadronization of the quark phase are the stages which present more difficulties for a theoretical treatment. Bjorken's model [23] provides a simple way of evaluating the initial conditions reached in nuclear collisions, and a simple evolutionary model on which to base further calculations on differential production rates which must involve an integration over the space-time history of the system.

2.3.1 Thermal e^+e^- production from the hot fireball.

Thermal e^+e^- production takes place both in the hadron gas and in the QGP by annihilation of their constituents. The basic processes contributing are

$$a)\quad q\bar{q} \to e^+e^- \qquad\qquad b)\ \pi^+\pi^- \to e^+e^- \tag{2.17}$$

The thermal e^+e^- production rate can be written in a similar fashion for both the hadronic gas phase and the QGP phase assuming the QGP to be an ideal gas of quarks and gluons. The different physics is absorbed in the transition matrix element of the processes (2.17) [15, 98, 68],

$$\frac{dN^{e^+e^-}}{d^4x} = \int d\Omega\, f_1(E_1) f_2(E_2)\, |M(1+2 \to e^+e^-)|^2\, (2\pi)^4 \delta(p_1 + p_2 - p_{e^+} - p_{e^-}) \tag{2.18}$$

where the subscripts 1 and 2 stand for the q and $\bar{q}$ in the case of QGP or π^+ and π^- in the case of a pion gas. $d\Omega = \prod d^4p_i/(2\pi)^3 \delta(p_i^2 - m_i^2)\theta(E_i)$ is the invariant phase space measure and $f_i(E_i)$ are the occupation probabilities for fermions (QGP) or bosons (pion gas), $f_i(E_i) = 1/(e^{E_i/T} \pm 1)$. We are assuming immediate decoupling of the e^+e^- pair after production and therefore we do not introduce Pauli blocking for the final state leptons.

Let us turn now to the form of the matrix element in the two possible scenarios:

a) QGP: If we neglect quantum effects in the QGP, we can approximate $f_i(E_i)$ by $f_i(E_i) \sim e^{-E_i/T}$ in (2.18). This approximation can be justified at high enough temperatures where a relativistic treatment of the quark gas is mandatory, but where quantum interference effects can be neglected due to the high number of degrees of freedom available in the system. This approximation will allow us to carry out an analytical solution of (2.18) which illustrates the main characteristics of thermal radiation from QGP. Under the mentioned assumptions the differential production rate of e^+e^- pairs from a QGP is,

$$\frac{dN^{e^+e^-}}{d^4x dM^2} = \frac{1}{2(2\pi)^4}\sigma(M)M^3 T K_1\left(\frac{M}{T}\right) \tag{2.19}$$

K_1 in (2.19) is the modified Bessel function of order 1 and $\sigma(M)$ is the first order cross section for the QED elementary process (2.17a),

$$\sigma_{q^+q^-\to e^+e^-} = F_q\frac{4\pi\alpha^2}{3M^2}\left(1-\frac{4m_q^2}{M^2}\right)^{-1/2}\left(1-\frac{4m_e^2}{M^2}\right)^{1/2}\left(1+2\frac{m_q^2+m_e^2}{M^2}+4\frac{m_q^2m_e^2}{M^4}\right) \tag{2.20}$$

where F_q counts the number of degrees of freedom due to colour, N_c, spin, s, and flavour, N_f,

$$F_q = N_c(2s+1)^2\sum_f^{N_f} e_f^2 \tag{2.21}$$

and e_f is the electric charge of flavour f. For a plasma composed only of u and d quarks $F_q = 20/3$. The quark and electron masses can be neglected in (2.20) which then simplifies to[3)]

$$\sigma_{q^+q^-\to e^+e^-} = F_q\frac{4\pi\alpha^2}{3M^2} \tag{2.22}$$

Integrating (2.19) over M^2 we can obtain the e^+e^- yield per unit volume and time,

$$\frac{dN^{e^+e^-}}{d^4x}(T) = \frac{10\alpha^2}{9\pi^3}T^4 \tag{2.23}$$

An estimation of the total e^+e^- yield involves the use of a model about the space-time evolution of the system to be able to integrate over d^4x. For an estimation of the behavior of the thermal e^+e^- production in a QGP we can take Bjorken's model for two interacting nuclei of the same size. Within this model the total e^+e^- yield per unit of rapidity is [68]

$$\frac{dN^{e^+e^-}}{dy} = \frac{12\alpha^2\sum_f e_f^2}{4\pi^2}R_A^2 t_o^2 T_o^4\left[\left(\frac{T_o}{T_c}\right)^2 - 1\right] \tag{2.24}$$

[3)]Note that if we were to consider dimuon production we could not neglect the muon mass in (2.20).

The differential invariant-mass dielectron yield can be obtained by integrating (2.19) over d^4x,

$$\frac{dN^{e^+e^-}}{dM^2} \propto \sqrt{MT^3}e^{-M/T} \tag{2.25}$$

Despite the simplifying assumptions of the Bjorken model, equations (2.24) and (2.25) show the main features of the thermal yield from a QGP: a strong dependence on the initial temperature of the system formed. Since for a hadronic system there is a limiting maximum temperature (above which we will reach a phase transition to QGP), the thermal production from QGP dominates any other yield for high enough initial temperatures.

b) Hadron gas: Given that the pions are composite particles, the cross section for the process (2.17b) will be given by the elementary QED annihilation cross section modified by the pion form factor,

$$\sigma_{\pi^+\pi^-\to e^+e^-} = |F_\pi(M)|^2 \, \sigma_{\pi^+\pi^-\to e^+e^-}|_{QED} \tag{2.26}$$

We must note that the elementary QED cross section of pion annihilation into e^+e^- differs from (2.20) due to the fact that pions are bosons. The Feynmann rules vertexes involving bosons are different from those for fermions [99] giving the QED annihilation cross section of two pions as

$$\sigma_{\pi^+\pi^-\to e^+e^-}|_{QED} = \frac{4\pi\alpha^2}{3M^2}\left(1-\frac{4m_\pi^2}{M^2}\right)^{1/2}\left(1-\frac{4m_e^2}{M^2}\right)^{1/2}\left(1+\frac{2m_e^2}{M^2}\right) \tag{2.27}$$

As in the previous case, we can neglect the electron mass and express (2.26) as

$$\sigma_{\pi^+\pi^-\to e^+e^-} = \frac{4\pi\alpha^2}{3M^2}\left(1-\frac{4m_\pi^2}{M^2}\right)^{1/2} \times |F_\pi(M)|^2 \tag{2.28}$$

The pion form factor can be obtained from the VMD model. We know that the process (2.17b) proceeds through $\pi^+\pi^- \to \rho \to e^+e^-$ and then $F_\pi(M)$ can be obtained from the ρ propagator. The result is

$$|F_\pi(M)|^2 = \frac{m_\rho^4}{(M^2-m_\rho^2)^2 + m_\rho^2\Gamma_\rho^2} \tag{2.29}$$

With the cross section from (2.28) we can use (2.18) to calculate the e^+e^- yield from a hadron gas, with the only difference that a simple analytical form like (2.24) can not be obtained. One should note that the hadron gas temperature has a limit, above which the phase transition to QGP occurs.

A major difference between thermal radiation from QGP and a pion gas is the shape of the resulting e^+e^- invariant mass spectrum. The invariant mass spectrum from pion annihilation shows a threshold at twice the pion mass and is strongly favoured in the ρ region due to the pole in (2.29). On the other hand the thermal dielectron spectrum from QGP (2.25) shows an exponential distribution without a lower threshold (the constituent quark masses can be neglected at the temperatures involved). The results on any prediction of the relative strength of both yields are very sensitive to the dynamical model used to describe the evolution of the system and the initial conditions assumed.

2.3.2 e^+e^- production through bremsstrahlung

An additional source of e^+e^- pairs both from QGP or the hadron phase is bremsstrahlung of the respective constituents, $qq \to qqe^+e^-$ and $\pi\pi \to \pi\pi e^+e^-$, where a virtual photon is radiated off as shown in figure 2.9. The rate for this process can be written in a similar fashion to (2.18). The only difference being the Bose-condensation or Fermi-blocking factors needed for the final state particles[4)].

In an obvious notation,

$$\frac{dN^{e^+e^-}}{d^4x} = \int d\Omega\, f_1(E_1) f_2(E_2)\,(1 \pm f_3(E_3))(1 \pm f_4(E_4))|M(1+2 \to 3+4+e^+e^-)|^2 \times (2\pi)^4 \delta(p_1+p_2-p_3-p_4-p_{e^+}-p_{e^-}) \tag{2.30}$$

e^+e^- pairs emitted by bremsstrahlung are typically soft and will populate the very low invariant mass region of the spectrum, $m_{e^+e^-} < 50$ MeV/c^2. The total bremsstrahlung yield will depend on how much time the system spends in each phase and, again, we meet here the uncertainties introduced by the dynamical model used in describing the space-time evolution of the interaction.

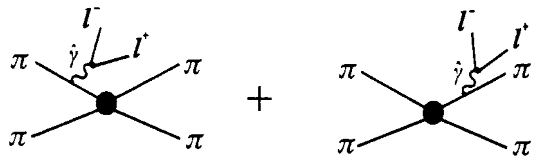

Figure 2.9: Lowest order bremsstrahlung processes from elastic pion scattering.

2.3.3 e^+e^- pairs from vector meson decays

The ρ, ω and ϕ mesons produced in a nuclear interaction will decay through the two body process ρ, ω, $\phi \to e^+e^-$ according to the proper branching ratio. These decays are the subject of intense theoretical research for they can provide valuable information on the dynamics of the fireball.

[4)]In a bremsstrahlung process, quarks in the QGP or pions in the hadron gas are scattered into a medium where states are already occupied with a weight given by the Fermi-Dirac or the Bose-Einstein functions. This is not the case in annihilation processes in the QGP or pion gas, where we are assuming that the produced e^+e^- pair leaves the interaction region immediately

ϕ enhancement as an indication of QGP formation

The rationale to study ϕ production in heavy ion collisions has been explained in detail in Section 1.3 and we will not repeat it here. We will only stress that the decay of the ϕ meson into dileptons, $\phi \to \ell^+\ell^-$, provides an excellent tool to address the questions of the expected ϕ enhancement and its decoupling temperature mentioned there.

The ρ peak as a chiral symmetry restoration indicator

If we neglect the heavy-quark sector, which is not relevant at the energies we are talking about, the QCD Lagrangian almost possesses chiral symmetry due to the small masses of the u and d quarks. However the QCD vacuum is definitely *not* chirally symmetric as can be seen from the vacuum expectation value of the quark condensate, $\langle 0|\bar{\psi}\psi|0\rangle \sim -(240\text{ MeV})^3$. This spontaneous breaking of chiral symmetry has important consequences for QCD phenomenology at the hadronic level, which are usually treated within QCD sum rules, effective Lagrangians or lattice QCD approaches. The general result is that $\langle 0|\bar{\psi}\psi|0\rangle$ decreases with increasing density or temperature, reaching a symmetry restoration phase transition where it becomes 0. This translates into a reduction of the hadronic masses in the dense medium, a "melting" effect, as we approach the critical point.[5)] A well known example is the reduction of the nucleon mass within the nucleus as calculated by Walecka [101] using a scalar mean-field model.

However there is presently no full consensus about how the effects of the dense medium should affect the parameters of the ρ meson. Calculations by Brown and Rho [107] with an effective Lagrangian and Hatsuda and Lee and Asakawa and Rho [31, 108] within the QCD sum rule approach, show that the ρ mass peak decreases with increasing medium density. Within the same framework, it has been suggested that the ρ width decreases with increasing temperature due to the appearance of the reduced ρ mass in the expression of its width [109]. On the other hand, VMD-model and chiral-perturbation based calculations result in a broadening of the ρ width, while its mass does not change appreciably [110].

The conditions under which chiral symmetry is restored are expected to be similar to those for the hadron-QGP phase transition [2]. Whether both transitions occur at the same temperature T_o or the chiral symmetry restoring temperature, T_c, is higher than the deconfining temperature, T_d, is still an open issue. The case $T_c < T_d$ is excluded since any confining theory must break chiral symmetry [103]. An excellent tool to study this topic is provided by the ρ meson [104, 105]. Due to its much shorter lifetime ($\tau_\rho = 1.3$ fm/c) compared with typical fireball lifetimes of 10-20 fm/c, several generations of ρ mesons are produced and decay during a nuclear collision at SPS energies [69]. The most important aspect is that they decay inside the dense interaction region, while they retain their reduced mass.[6)] Thus, their decay

[5)]The effect is expected to be more pronounced in the density axis than along the temperature axis. In the limit of zero baryon density and high temperature the reduction of the hadronic masses is due to the presence of baryon-antibaryon pairs. At lower temperatures, the density effect dominates.

[6)]Note that when we take into account the space-time development of the system $\rho = \rho(t)$, and therefore through the dilepton channel provides a unique experimental window to the dense-medium effects on the ρ. This effect is not so clear for the other mesons, ω, ϕ or J/ψ because of their much longer lifetimes: they will be re-absorbed in the medium or they will decay well outside the interaction region when they have regained their vacuum masses.

An experimental input on this topic is indeed needed in order to distinguish the different and somewhat conflicting scenarios just mentioned. It is, in any case, clear from the previous discussion that the dielectron yield will be affected by the behavior of the ρ parameters with temperature and density. Consider for example pion annihilation. As we saw in Section 2.1, it proceeds through an intermediate virtual ρ, whose mass and width enter the pion form factor as

$$|F_\pi(M)|^2 = \frac{m_\rho^4}{(M^2 - m_\rho^2)^2 + m_\rho^2\Gamma_\rho^2} \tag{2.31}$$

A distorted, and possibly shifted, ρ peak, would open pion annihilation channels at lower $\pi^+\pi^-$ invariant masses, where they are more abundant. This will produce an enhancement of the dielectron yield at $m_{e^+e^-} \leq m_\rho$ which should be detectable experimentally. We will come to this point in Chapter 6 when discussing the results of CERES.

2.4 Summary of contributions to the dielectron spectrum

We will now put all the pieces together and summarize the contribution of each of the processes just mentioned to different dielectron invariant mass ranges.

Two-body resonance decays: The relevant processes for CERES are the decays of the ρ, ω and ϕ. They will produce the typical resonance Breit–Wigner peak, possibly modified by dense-medium and/or high temperature effects.

Dalitz decays: Decays of the π^o, η and η' into γe^+e^- and ω into π^o e^+e^- . They populate the low mass region, below the ρ peak.

Drell-Yan mechanism: Dominant process at high masses ($M \geq 2$ GeV/c^2), competing with heavy flavour decays. Shows an approximate exponential invariant mass distribution, parametrised in terms of a "Drell–Yan temperature" T_{DY}

Heavy flavour decays: From the semi-leptonic decay of D mesons produced in the early nucleon–nucleon collisions. Contributes mainly to masses ($M \geq 2$ GeV/c^2).

Thermal production: This is the main topic of interest. It can originate from the QGP or a dense and hot hadron gas. The spectral shape in both cases is different: the hadron gas shows a threshold at $2m_\pi$ (which is absent in the QGP case where one

the hadronic parameters depend on time through ρ.

can neglect the quark masses) and presents a resonance behaviour in the ρ region. The QGP shows an exponential differential mass distribution. The relative strength of both sources is uncertain as the calculation depends strongly on the parameters used in the description of the space-time evolution of the collision.

Bremsstrahlung: Another important contribution at very low masses from elastic pion (quark) scattering in a pion gas (QGP). It contributes to pair invariant masses $M \leq 0.1$ GeV/c^2.

Chapter 3

The CERES experiment.

In this chapter I give an overall description of the CERES spectrometer and its performance in the heavy ion run of 1992, discussing in detail the main features which allow the efficient rejection of the combinatorial background to manageable levels and its successful operation in the high multiplicity environment of heavy ion collisions. At the end of the chapter I will also give a quantitative estimate of the signal and background expected within the CERES acceptance from the relevant dielectron sources.

3.1 Spectrometer description and performance.

There are three main experimental challenges that an experiment attempting to measure dielectrons in heavy ion collisions has to deal with. First, the high multiplicities inherent to this type of collisions: up to 160 charged particles per unit of rapidity in a central S-Au collision at SPS energies. Second, an extremely low dielectron yield ($\sim 5 \times 10^{-5}$ e^+e^- pairs per π^o) and, third, a strong yield of e^+e^- pairs from photon conversions and π^o Dalitz decays, which will produce a huge combinatorial background if not properly identified and rejected. CERES has developed a novel spectrometer capable of successfully operating in these conditions, as we describe below.

3.1.1 Overall design.

A schematic view of the CERES spectrometer is shown in Figure 3.1. The spectrometer consists of two azimuthally symmetric Ring Imaging Čerenkov (RICH) counters separated by a super-conducting double solenoid, covering the fiducial pseudo-rapidity region $2.10 \leq \eta \leq 2.65$. A spherical mirror in each RICH reflects the Čerenkov photons emitted in the radiator towards a UV-photon detector. The mirror in RICH1 needs to be as thin as possible to minimize conversions or interactions of secondaries in its material. It is made of a single piece 0.8 mm thick carbon fiber surface, held only at the outer circumference. In RICH2 the requirement for a minimum thickness is less critical and a solution based on a segmented 6 mm glass mirror was adopted. The need for the segments was dictated by its large size

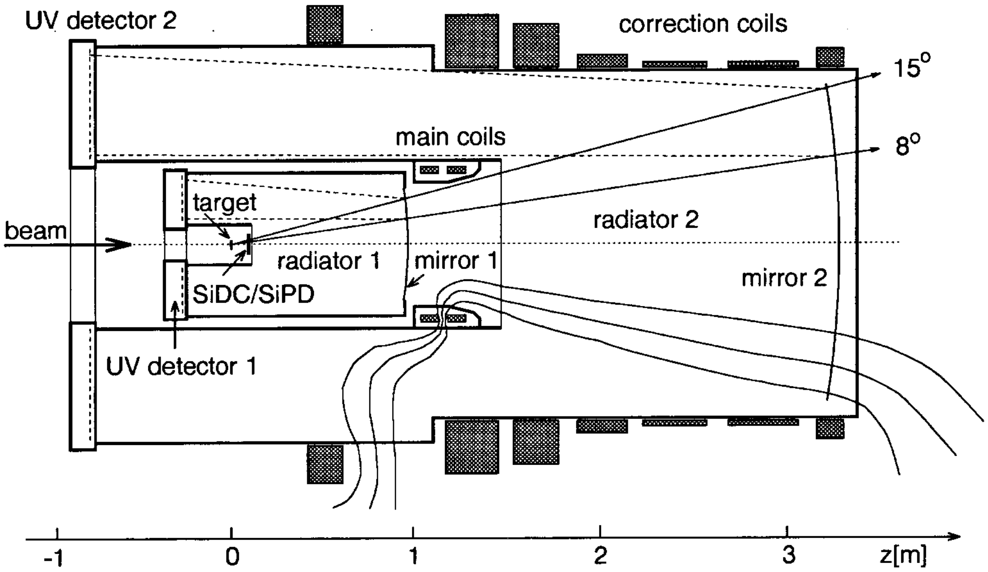

Figure 3.1: Schematic view of the CERES spectrometer.

(1.75 m. of outer diameter) and to provide mechanical stability to the whole structure.

An essential characteristic of the CERES design is the location of the UV detectors. They are placed at the focal plane of the mirrors, upstream of the target, and thus they are not traversed by the intense flux of particles produced in the interaction. A UV transparent window of calcium fluoride (CaF_2) in RICH1 and quartz in RICH2 separates the radiator from the UV detectors. The particles crossing the radiators produce a ring in the UV detector plane, due to the typical cone-shaped Čerenkov emission and the geometry of the mirrors (see the appendix). As the RICHes measure only the direction of the particle, there is no real tracking in the conventional sense.

The main field is generated by two superconducting coils which carry currents in opposite directions. The radiator region in RICH1 is kept field-free by an asymmetry in the currents of the superconducting coils and with the help of a conventional correction coil placed upstream of the main superconducting ones. The field in the radiator of RICH2 is shaped to be conical and pointing to the target. This is achieved by several warm correction coils placed around the RICH2 radiator as shown in Figure 3.1. The trajectories of the particles traversing RICH2 are then parallel to the field lines and remain unaffected also in this region. The overall effect of such field configuration is to produce a relative displacement in the ϕ coordinate of the corresponding rings in RICH1 and RICH2, $\Delta\phi$. This localized kick provides the momentum measurement as $p(\mathrm{GeV}) = 120/\Delta\phi(\mathrm{mrad})$. The charge is determined by the direction of the displacement.

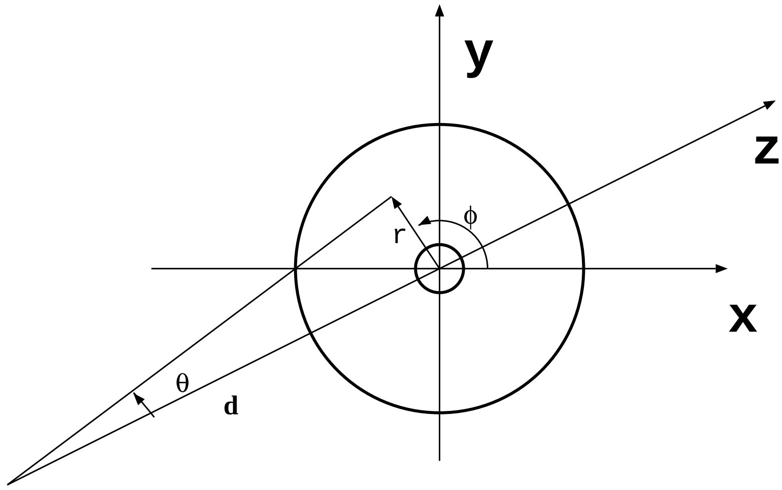

Figure 3.2: The CERES general coordinate system.

There are three main features in the design of the CERES spectrometer of particular importance for its operation at high multiplicities:

First, the spectrometer is "blind" to hadrons. The radiators of the RICHes are filled with CH_4 at atmospheric pressure, which has $\gamma_{thr} = 32$. This value ensures that essentially only electrons emit Čerenkov radiation when traversing the detector. High energy pions with $p \geq 4$ GeV/c start to be above their Čerenkov threshold, producing rings of variable radius depending on their momentum. The pion ring radius reaches 95% of the asymptotic electron radius for pion momentum of $p \sim 15$ GeV/c (see the appendix).

Second, the amount of material within the acceptance (not counting the target) has been kept at the level of 1% of a radiation length (see section 3.2 below). This minimizes the amount of gamma conversion pairs which would otherwise contribute to the combinatorial background.

Third, the magnetic field shaping results in a field-free region in RICH1. This is of extreme importance since it allows to recognize and reject Dalitz decays and conversion pairs by a cut in their opening angle.

In addition the spectrometer has a Silicon detector (SiPAD) and a Silicon drift chamber (SiDC) located just after the target. The SiPAD detector provides the first–level trigger through a coarse multiplicity evaluation. The high resolution SiDC serves as a precise multiplicity detector used off-line for the event characterization. It also helps in the rejection of conversions and fake tracks. A description of both detectors and their performance will be given below.

Although hardwarewise each detector has its own coordinate system ((x,y) for the RICHes, (r,ϕ) for the SiDC), the global coordinates used in the analysis are (θ , ϕ) as shown in Figure 3.2. This is a natural choice given the configuration of the magnetic field between the RICHes. For the SiDC the polar angle θ of a particle is given by tanθ=r/d, where d is the distance from the target position. In the case of the RICHes θ is given by θ=r/f, where f the mirror focal length.

3.1.2 The UV detectors.

The UV detectors are the essential elements of the spectrometer. They are gas chambers filled with a mixture of He (94%) and C_2H_6 (6%) and saturated vapor of TMAE at 40 ^oC as photosensitive agent. The detectors are operated at a gain of $3-5\times10^5$ at atmospheric pressure and are kept at a temperature of 50^oC in order to prevent TMAE condensation.

The layout of the UV detectors is depicted in Figure 3.3. After entering the detector volume from the radiator, Čerenkov photons are converted to electrons by photoionization in the TMAE in a 15 mm deep conversion gap. The measured absorption length in the TMAE at the operating conditions of the spectrometer is 6.6±0.2 mm and, therefore, the conversion gap corresponds to 90% conversion efficiency [111]. The primary electron drifts under the electric field existing in the conversion region until it reaches the first amplification stage. This consists of a Parallel Plate Avalanche Chamber (PPAC). The PPAC electrodes are made of a stainless steel mesh of 50 μm wire diameter and 500 μm spacing glued to two concentric rings made of G10. There are no spokes connecting the two rings. Instead, the two rings keep the tension of the mesh and in turn the mesh keeps the two rings concentric. The resulting avalanche drifts further to the second amplification stage, another PPAC, and then to the last amplification stage, a multi-wire Proportional Chamber (MWPC). The first cathode of the MWPC is a mesh plane identical to the PPAC electrodes. The anode plane of the MWPC is a wire plane divided azimuthally in 10 sectors (16 in UV2) by radial spokes connecting the inner and outer frame. The wires are made of gold-plated tungsten, having a 30 μm diameter and arranged with 3 mm spacing. The spokes define the wire geometry (the wires are parallel to the central radius within each sector) and provide the mechanical stability that the wires alone cannot supply.

The Pad Readout.

The second cathode of the MWPC is a pad array readout plane consisting in a sandwich structure of a resistive layer (RL)[1)], a 0.6 (2.6 in UV2) mm dielectric made of G10 and the pad electrode. The pads are squared and etched on a copper plate with a pitch of 2.74 (7.62) mm in UV1 (UV2), so that 53800 (48400) pads are needed to cover the whole active area of the UV detectors (0.42 and 2.84 m^2 respectively). Each pad is connected to a socket at the outer side of the detector where preamplifiers are directly plugged. The preamplifiers and the read–out logic are controlled by CAMEX chips. These chips contain 64 multiplexed channels

[1)] An epoxy resin-based paint of high resistivity.

and they are arranged in a modular structure, each module serving 256 (8×32) channels in UV1, ie. 4 chips, and 121 (11×11) channels in UV2, ie. 2 chips.

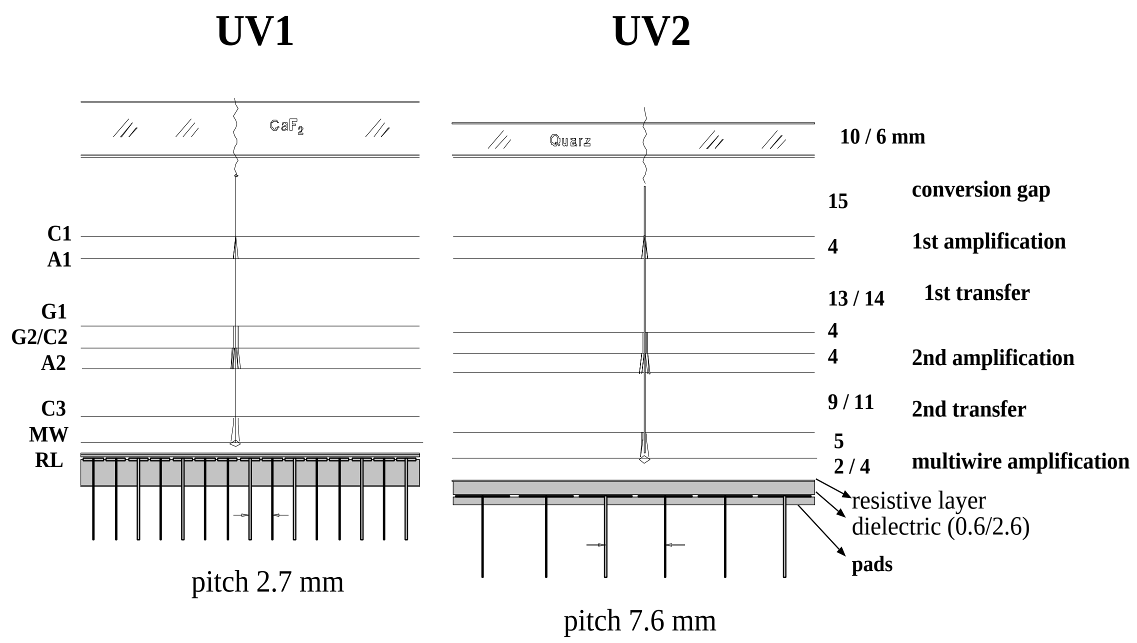

Figure 3.3: The amplification/detection scheme of the UV detectors. Distances are shown in mm for UV1/UV2.

The charged avalanche collected in a wire induces a charge accumulation in the RL which in turn induces a charge in the pads. The shape of the induced signal is Gaussian to a very good approximation[2)] , extending over a few neighboring pads, typically within a 5×5 pad box. This allows the determination of the position of the original incoming photon by calculating the center of gravity of the final avalanche. The preamplified analog pad pulse amplitudes are sent to 16 (14) chains in UV1 (UV2), which are read out at a typical speed of 2.5 MHz. The readout proceeds by reading at the same time the first pad of each module, then the second, and so on. Several chips are thus chained into a common output line, making the readout a multiplexed and parallel process. The total readout time achieved is about 1600 μs per detector.

Each pad pulse height is then digitized. In order to reduce the event length and, thus, the

[2)]The charge distribution induced by a point-like electric charge Q placed near an anode wire on the pad cathode plane can be calculated using the method of charge images. In one dimension it is given by

$$\sigma(x) = -\frac{Q}{4d} sech(\frac{\pi x}{2d})$$

where d is the distance between the anode wire and the cathode plane.

dead time used for writing the event to tape, a *zero-suppression* is performed on the digitized information of both RICHes: only pads with an amplitude above a predefined level[3)] are stored on tape. Typical event lengths after the zero-suppression are 500 to 5000 pads.

A typical S+Au collision as seen by the UV detectors (UV2) is shown in Figure 3.4. Two asymptotic electron rings can be easily identified along with some single hit background. Such single hits originate from pions just above threshold and low energy δ-electrons, where the full ring structure is lost due to the effect of multiple scattering. Also fast particles emitted backwards and traversing the UV detectors can produce short tracks or big blobs of activated pads, most of them in saturation, introducing an additional background. In Section 5.2 below we show an example of this and how the off-line analysis has been tuned to reject such background.

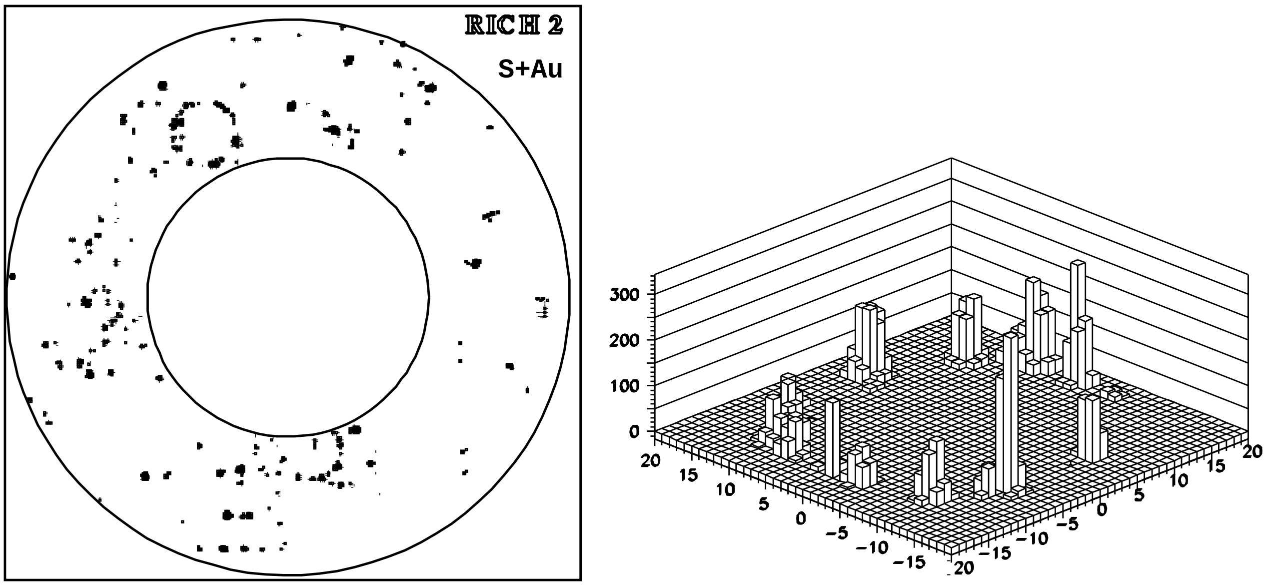

Figure 3.4: A S+Au collision as seen in RICH2. A series of background hits and two asymptotic electron rings can be easily identified. The pad structure of one of the rings is shown in the right plot.

For calibration purposes, a pulsed UV-lamp is mounted on each RICH detector. It illuminates approximately 1/4 of each detector. The specifications of the two RICH detectors, including the two UV-photon detectors, are summarized in Table 3.1, and details on the construction and laboratory's test performance of the UV detectors are given in [111, 112].

[3)]An amplitude $a \geq p + 3\sigma$ was required to considered the pad fired, where p stands for the pad's pedestal and σ the pedestal's r.m.s

Spectrometer specifications

	RICH1	RICH2
RICH specifications:		
$\Delta\eta$	0.93	0.61
$< \eta >$	2.34	2.34
Radiator length (m)	0.9	1.75
Radiator gas	CH_4	CH_4
γ_{thr} (measured)	31.4	32.6
window	CaF_2	quartz
RICH band width (eV)	5.4 – 8.5	5.4 – 7.4
Mirror specifications		
material (thickness)	carbon fiber (0.8 mm)	glass (6 mm)
geometry	one piece	10 azimuthal segments
inner/outer diameter (m)	0.20 – 0.65	0.85 – 1.75
focal length (cm)	126	420
UV-detector specifications:		
UV-detector area (m^2)	0.42	2.84
inner/outer diameter (m)	0.27 – 0.79	1.06 – 2.20
number of pads	53800	48400
pad size (mm^2)	2.74×2.74	7.62×7.62
channels/module	8×32	11×11
number of modules	210	400
readout chains	16	14
readout freq. (MHz)	2.5	2.5
readout time (μs)	1600	1600

Table 3.1: Specifications of the two RICH detectors.

3.1.3 Performance of the RICH detectors.

There are two basic quantities which define the performance of a RICH detector: the figure of merit, N_o, and the single hit resolution.

The figure of merit determines the average number of photons in an asymptotic electron ring as $\langle N \rangle = N_o L/\gamma_{thr}^2$, where L is the length of the radiator. N_o is given by the folding integral of the conversion efficiency of the TMAE over the bandwidth of the RICH. RICH1 is sensitive to photons in the range 5.4–8.5 eV, while RICH2 to the 5.4–7.4 eV range. These boundaries are determined by the ionization threshold of the TMAE and the window transmission cut-off, the different upper values in both detectors reflecting the different window materials. A CaF_2 window for UV1 was chosen because of its higher transmission cut-off which compensates for the shorter radiator length of RICH1, giving a final number of photoelectrons per ring similar to that in UV2. The values obtained for the theoretical N_o are 229 and 135 cm^{-1} for RICH1 and RICH2 respectively.

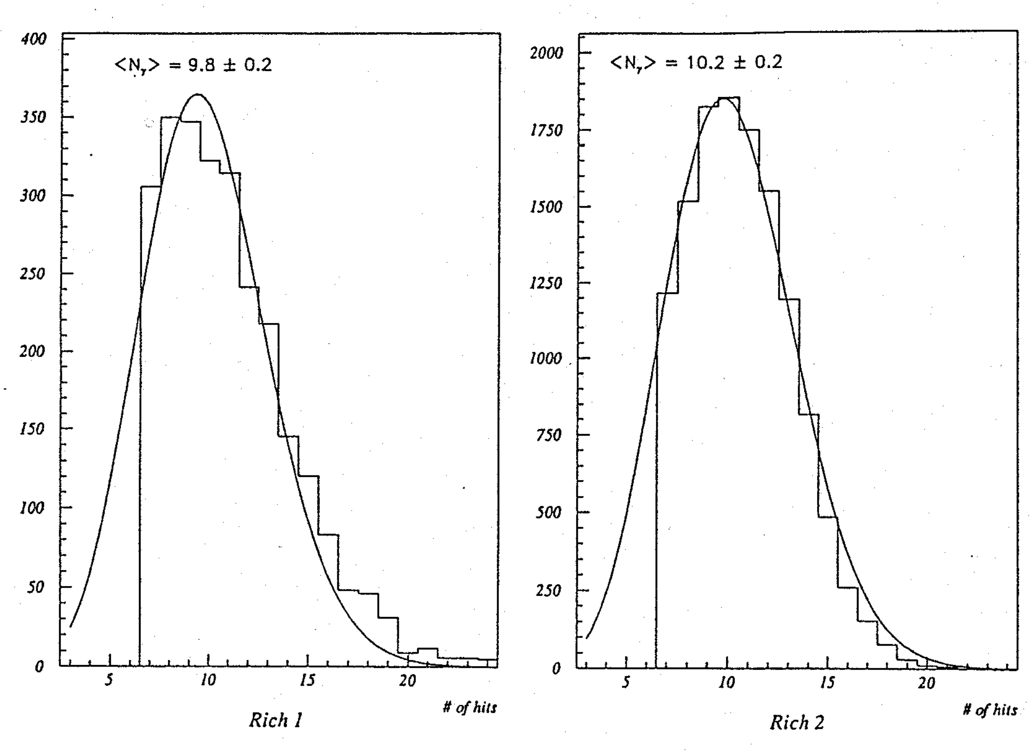

Figure 3.5: Measured distribution of number of hits per ring. The curve is a fit to a Poisson distribution.

The theoretical values of N_o are somewhat degraded by the transmission efficiency of the optical system –radiator transparency and mirror reflectivity– hit losses due to the spokes, the efficiency of the conversion gap and the transparency of the first anode grid of the UV chambers. The zero-suppression applied on the pad signal introduces an additional loss of low amplitude hits. All these losses are explicitly quoted in Table 3.2 and result in a final value of N_o of 131 (78) cm^{-1} in RICH1 (RICH2). The expected values of the average number of photon hits per ring is 11.8 (12.6) in UV1 (UV2). To compare these numbers to the measured ones, we must introduce a final correction due to the finite pile-up probability of two hits on

Number of photons per ring

	RICH1	RICH2
N_o theoretical value	**229**	**135**
mirror reflectivity	0.85	0.85
radiator transparency	0.98	0.96
window spokes losses	0.93	0.93
first anode mesh transparency	0.89	0.89
conversion efficiency	0.90	0.90
signal threshold (zero-suppression)	0.92	0.92
N_o expected value	**131**	**78**
γ_{thr} (measured)	31.6	32.6
radiator length (cm)	90	172
expected photons/ring ($N_o L/\gamma_{thr}^2$)	**11.8**	**12.6**
hit pile-up prob.	0.17	0.16
expected resolved photons/ring	**9.8**	**10.6**
measured resolved photons/ring	**9.8**	**10.2**

Table 3.2: Comparison of the expected an measured average number of photons per ring.

a ring, which are not resolved by the hit finding software. The pile-up probability for a ring with $\langle N\rangle$ hits and radius R is

$$P(d) = 1 - e^{d\langle N\rangle/2\pi R} \tag{3.1}$$

where d is the double hit resolution (1.5 pads). The pile-up probability amounts to 17% in both UV detectors. This effect brings the number of expected *resolved* photons per ring to 9.8 (10.6) in UV1 (UV2). The measured values are 9.8 and 10.2 respectively (see Figure 3.5), well within less than 5% of the expected ones, ruling out any hit losses of hardware or software origin.

The single hit resolution, σ_h, is the quantity that defines the mass resolution of the spectrometer through the ring center resolution, σ_c. It can be viewed as the average spread of the hits with respect to the nominal asymptotic ring radius. The ring center resolution depends on the single hit resolution as

$$\sigma_c = \frac{\pi}{2\sqrt{\langle N\rangle - 2}}\sigma_h \tag{3.2}$$

It also determines the ring quality through the ring radius resolution,

Single-hit resolution
(rms in mrad)

	RICH1	RICH2
chromatic dispersion	0.89	0.53
readout accuracy (finite pad size)	0.33	0.25
single electron diffusion	0.37	0.11
mirror quality	-	0.35
expected resolution	1.08	0.69
measured resolution	1.02	0.76

Table 3.3: Comparison of the expected and measured single hit resolution.

$$\sigma_r = \frac{1}{\sqrt{\langle N \rangle - 2}} \sigma_h \tag{3.3}$$

which in turn is crucial in the electron/pion separation. For an infinite momentum particle, the single hit resolution is limited by the chromatic dispersion of the radiator gas, the electron diffusion in the conversion gap and the readout accuracy due to the finite pad size. An additional effect in RICH2 is introduced by a small blurring effect due to the non uniformity of the focal length over the different sectors of the mirror. This effect is negligible for the single-piece mirror of RICH1. A further momentum dependent contribution comes from the multiple scattering in the radiator. Note that only the multiple scattering in the radiator gas contributes to the single hit resolution. The other materials in the spectrometer contribute to the ring center resolution, but do not affect the quality of the rings. All the mentioned contributions are given in Table 3.3 together with the resulting expected and measured single hit resolution. In Figure 3.6 we show the measured value obtained from a gaussian plus a linear background fit to the distribution of hit distances from the ring center for high-momentum ($p \geq 1$ GeV/c) particles, for which the multiple scattering is negligible.

3.1.4 The Silicon Pad Detector.

The SiPAD detector [113] is used for a coarse multiplicity evaluation which is the basis of the centrality trigger. It is located 90 mm away of the target and consists of 8 concentric rings, each one with 8 azimuthal sectors, giving a total of 64 pads. The pad sizes vary between 4

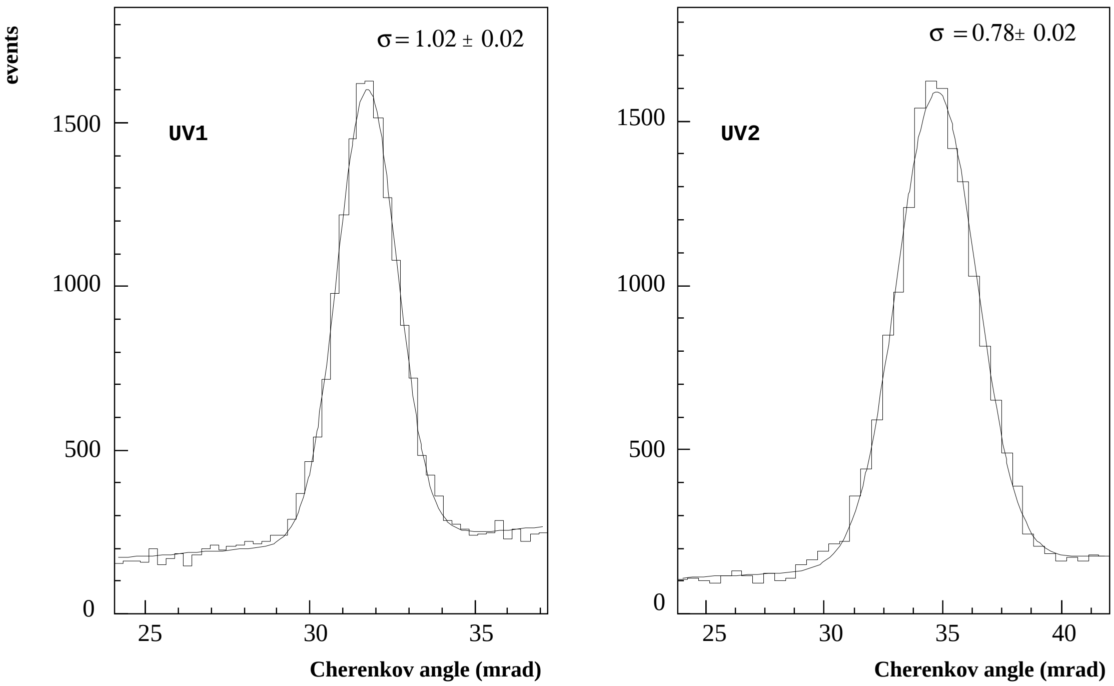

Figure 3.6: Measured single hit resolution for high momentum (p_t >0.2 GeV) particles. The curve is a fit to a gaussian plus a linear background. The values quoted are the r.m.s in mrad.

mm^2 and 168 mm^2 in order to cover a similar $dN_{ch}/d\eta$ range per sector. A 5 mm diameter hole in the middle of the detector allows beam passage. The active area is 27.5 mm^2 between radii 4.5 and 32 mm. which at 90 mm from the target corresponds to a pseudo-rapidity coverage of $1.6 \leq \eta \leq 3.6$. A schematic view of the response of the detector to a central S-Au interaction is shown in Figure 3.7. The grey scale is proportional to the analog signal in the corresponding pad.

The signal deposited by a minimum ionizing particle is amplified by DC–coupled charged preamplifiers located inside the target tube (see figure 3.10). The resulting signal is delivered to eight fast summing electronics VME modules (one per ring). An additional "super-sum" module delivers the total analog sum of the eight channels for triggering purposes. With a proton beam the SiPAD can work in digital mode. The input to the eight summing modules is then the number of hit pads in the corresponding ring. The summing module provides the total number of hit pads, which is compared to a predefined digital threshold to issue a trigger signal.

With a nuclear beam the high multiplicities seen by the detector easily saturate the digital logic and, therefore, the total analog signal is used instead. The event multiplicity is then determined from the analog response of the pads by analyzing them as a convolution of Landau distributions produced by minimum ionizing particles. The multiplicity derived in

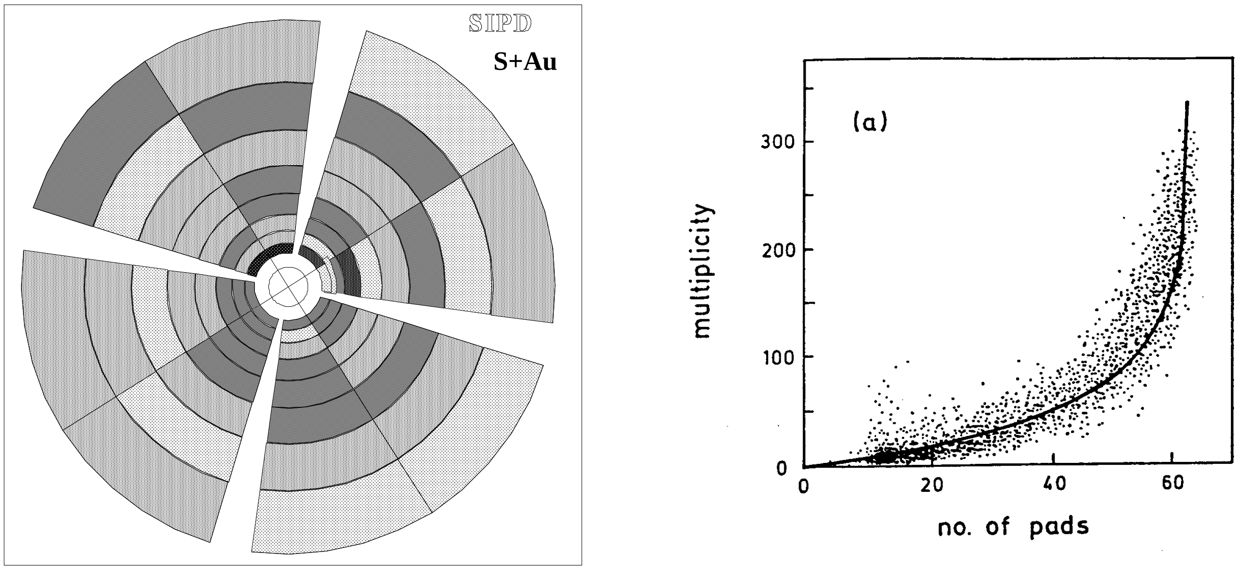

Figure 3.7: **left:** The SiPAD detector, where the pad structure of the eight concentric sectors can be seen. The grey scale is proportional to the analog signal seen by each pad. The summed analog signal of these sectors is used to define the first–level trigger. **right:** The number of hit pads as a function of the event multiplicity. The superimposed curve represents the expectation of a uniform multiplicity distribution over the covered pseudo-rapidity range.

this way is shown in the right plot of Figure 3.7 as a function of the number of hit pads. We see that for the typical multiplicities produced in heavy ion collisions the number of hit pads in the detector is already saturated and we need the analog operating mode.

3.1.5 The Silicon Drift Chamber.

The SiDC is located before the SiPAD, 80 mm after the target, and provides the (θ, ϕ) coordinates of the charged particles produced in the collision. It has a disc shape of 3" diameter and 280 μm thickness. A schematic view of the detector is shown in Figure 3.8 and a detailed description of its specifications and performance can be found in [114].

Electrons liberated in the silicon by fast particles traversing the detector drift radially, towards the outer edge of the chamber, which consists of an array of 360 anodes where the electrons are collected. The drift time gives the radial coordinate of the particle, r (or, equivalently, θ), and the charge deposit in the anodes measures the azimuthal coordinate, ϕ. The longest drift distance is about 3 cm, corresponding to a drift time of 4.2 μs with the chosen drift field of 500 V/cm. The anode signal is fed into a charge-sensitive preamplifier located inside the target tube and then sent to a quasi-gaussian shaper–amplifier outside the spectrometer. The pulses are then sampled by a FADC at a rate of 50 MHz. For the total drift time of 4.2 μs this corresponds to 210 equivalent pixels per anode and, therefore, a total 75600

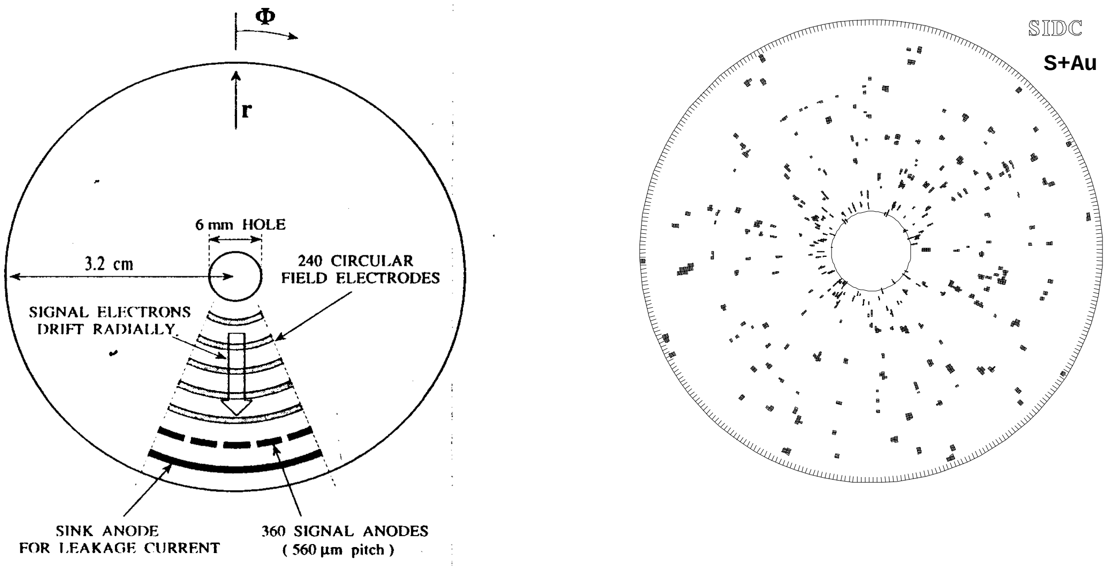

Figure 3.8: **Left:** Schematic view of the SiDC detector. **Right:** A typical S+Au event as seen by SiDC. The SiDC provides the (θ, ϕ) coordinates of the charged particles produced in the collision and serves for the off-line characterization of the event multiplicity.

pixels for the whole detector.

The drift time is the crucial ingredient which limits the detector resolution, as the electrons diffuse both in the drift direction and in the azimuthal direction, ϕ, during this time. Thus the initial charge is shared by adjacent anodes, and the ϕ coordinate of the original particle is obtained by calculating the centroid of the produced pulse in the azimuthal direction. The resolution of the detector is therefore a function of the radial distance from the anode where the hit was produced.

The detector used in the 1992 run was the first of a series of custom-designed SiDCs used in subsequent CERES runs, and suffered from two imperfections. First, memory limitations in the software used to produce the lithography masks in the construction phase forced a polygon approximation to the ideal circular geometry. The concentric field rings which define the drift field were actually 120^o polygons. This deviation from the circular geometry tends to focus the drift cloud into the anodes aligned with the central anodes of the 3^o field shaper segments. This results in a drastic loss of charge division which affects the azimuthal resolution, especially for hits produced in the inner part of the detector (about two thirds of these hits are focused into one single anode). Second, a ballistic deficit due to a capacity-dependent amplifier gain introduces a drift-time dependent pulse amplitude. This effect becomes significant for hits produced at r $<$ 15 mm.

A further unexpected problem which somewhat degraded the in-beam performance of the

SiDC specifications

Material		n-type silicon, 280 μm thick.
Geometry		3" wafer. Central hole of 3.2 mm radius. 360 charge collecting anodes. 240 drift field shaping electrodes of 3^o polygon structure.
	sensitive region:	$4.5 < r < 32$ mm, $0 < \phi < 2\pi$.
	θ acceptance:	$3.3 < \theta < 22.3$ degrees.
	η acceptance:	$1.62 < \eta < 3.55$
Electron drift	field:	500 V/cm
	drift velocity:	6.7 mm/μs
	max. drift time:	4.2 μs
	max. diffusion:	26 ns
Resolution	in r	from 6.7μm at r=0.48mm to 25μm at r=26mm.
	in ϕ	3 mrad (hits with charge sharing) between 5 mrad and 16 mrad (hits without charge sharing).

Table 3.4: Specifications of the SiDC geometry and materials.

detector was a pick-up induced by the readout electronics of RICH1, and which could not be adequately shielded. An on-line amplitude threshold of 15 mV (6.5σ of the noise) on the analog signals was applied to avoid excessive event lengths, introducing an additional inefficiency through the loss of low amplitude hits. However the overall efficiency of the detector is 85% when including all the mentioned effects, reaching 95% at large radii, the expected value if one considers the 5% dead anodes. This is shown in Figure 3.9, where a Monte Carlo simulation of the detector is shown as the histogram and the dots represent the measured efficiency. The efficiency is calculated by measuring the number of hits in a r window and comparing it with the expected one from the known rapidity distribution as measured by WA80 [27].

The resolution of the SiDC has been measured with a laser [114]. In the drift direction r it varies from $\delta r = 6.7$ μm at $r = 0.48$ mm to $\delta r = 25$ μm at $r = 26$ mm. The double hit resolution in the r direction is $\sim$400 μm. In the ϕ direction the effect of diffusion is combined with the mentioned focusing effect caused by the finite size of the drift field shapers. The measured resolution in the ϕ direction is 2.5 mrad for hits with charge sharing, while it varies from $1^o/\sqrt{12} = 5$ mrad close to the anodes to three times this value in the center, for hits

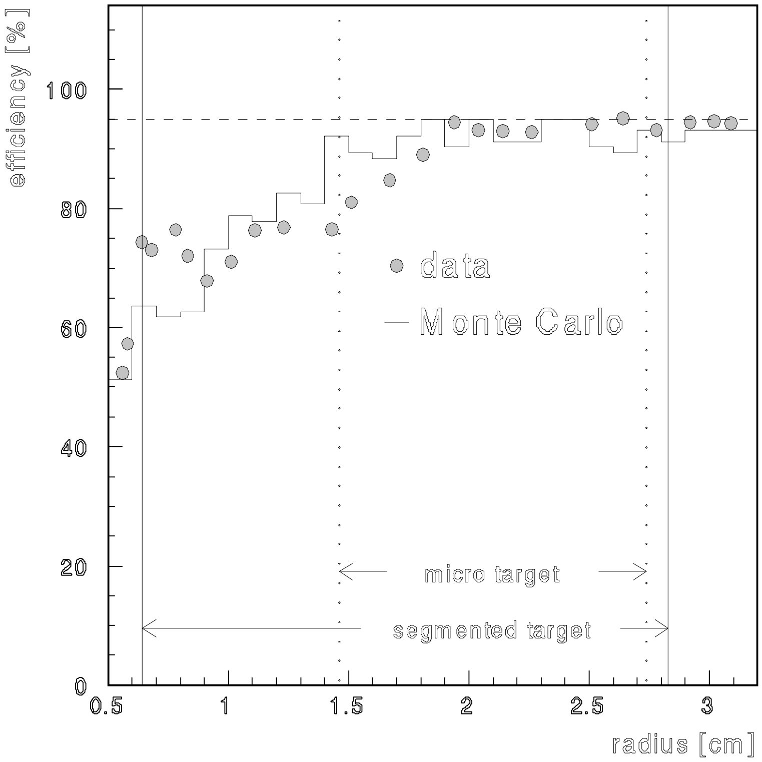

Figure 3.9: SiDC efficiency.

without charge sharing (35% of the total). The double hit resolution in the ϕ direction was found to be $\sim$40 mrad.

The SiDC is used for off-line characterization of the events, providing a precise information of the rapidity density of charged particles, dN_{ch}/dy. In addition it is used in the pattern recognition. In the analysis, a track is defined by one ring in UV1 centered at (θ, ϕ), a ring in UV2 centered at θ and with an azimuthal displacement which gives the particle momentum, and a corresponding hit in the SiDC also at (θ, ϕ). This last requirement assures that the track originated in the target and helps eliminating fake tracks and downstream conversions occuring after the SiDC. It also proves a very powerful tool for rejecting conversions occurring in the target by identifying the corresponding tracks by an unresolved double-dE/dx amplitude hit or two close hits with single dE/dx amplitude.

The target volume.

The SiPAD and the SiDC, along with their preamplifiers and the target disks are held mechanically in a common structure provided by a double wall carbon fibre tube as shown in Figure 3.10. A cooling of this volume is essential as the spectrometer is kept at an average temperature of around 50^o, the operation temperature of the TMAE in the UV detectors surrounding the target. The SiDC detector and the preamplifier electronics are cooled by an air flow entering the target volume through slits in the carbon fibre walls. The SiPAD detector itself is cooled by an independent air stream fed directly through the back-end motherboard.

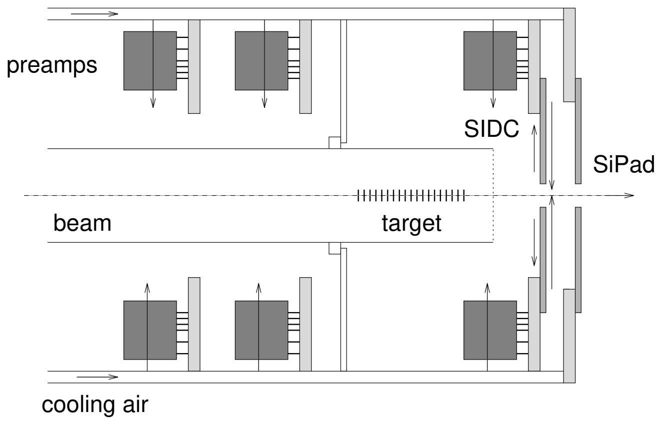

Figure 3.10: The CERES target area. A double wall carbon fibre tube serves both for holding the SiPAD and the SiDC in position respect to the beam direction and for the cooling system.

3.1.6 The trigger system.

The definition of a valid incoming beam particle is obtained from two small (60 mm diameter and 2 mm thick) scintillator counters, B1 and B2, read by two photomultipliers and placed before the target. They further define the trigger timing. A first indication of a possible interaction is defined by another scintillation counter, V2, placed behind the spectrometer. It is a large (500×500 mm^2) scintillator with a central hole of 30 mm diameter to allow beam passage when no interaction occurs.

The trigger operates in two steps. A first–level trigger (FLT) characterizes a valid interaction from B1+B2+V2 and the information on the multiplicity as provided by the SiPAD. In the case of heavy ion collisions, the sum of the analog information (summed pulse height) of all channels in the SiPAD is used to define the trigger. This is equivalent to selecting the events according to their impact parameter, central or peripheral. If the overall sum is greater than a predefined threshold, a FLT signal is issued which starts the readout of all the detector components.

A second level trigger (SLT) has been developed to select only those events with candidate electron pairs. It performs a rough pattern recognition on a reduced pad grid in UV1 using only each second pad in each direction. A complex processor "performs" a Hough transformation on the pad array, building a ring of the nominal electron radius around each hit pad. Candidate ring centers are then identified as maxima in the Hough array. Two candidate rings closer than 32 mrad are rejected as a likely Dalitz or conversion pair, and the event is passed to the DAQ if it contains at least two isolated ring candidates[4)]. When running in triggered mode the grid pads are the first to be read out, so the second level trigger can start the evaluation of the event while the rest of the information is being read out. The information of the SLT is available 500 μs after the interaction.

3.2 Signal and Background estimates.

In the absence of new physics we expect the dielectron yield in a nuclear collision to originate from the decays of the known hadronic sources. In Table 3.5 we summarize the relevant hadron decays which contribute to the e^+e^- yield in the invariant mass region covered by CERES. We have included the decays of the π^o, η, η', ρ, ω and ϕ as mentioned in Section 2.1.1. The values of the differential cross sections listed in the second column are taken from the NA27 experiment on p-p interactions at 450 GeV/c [96], and the branching ratios from the PDG compilation [115]. We will call the yield above invariant pair masses of 200 MeV/c^2 from these hadronic sources the *signal*. This mass cut assures the rejection of the π^o Dalitz decay mode which is the overwhelming contribution at very low pair masses. The last column of Table 3.5 shows the relative strength of the signal with respect to the π^o yield at central rapidity, both without and with a p_t cut of 200 MeV/c on the single tracks of the pair. This cut is used in the data analysis to reject the much softer conversion and π^o Dalitz tracks. The yield per π^o is used for normalization purposes as explained in Section 4.3. Any new source of dileptons in heavy ion collisions will be detected as a deviation of the dilepton spectrum from the signal as defined above.

We see that we have to be able to detect an extremely weak source of dielectrons, of the order of $5\times10^{-5}/\pi^o$. Here we must note the importance of the p-p and p-Au part of the CERES programme. A systematic study of hadron-hadron, hadron-nucleus and nucleus–nucleus collisions with the same experimental set-up allows, first, to prove that the spectrometer is able to detect the weak dilepton pair yield and, second, to consistently compare the results of the hadron programme with those from the nuclear programme, allowing the direct identification of any deviation from the known physics in the later case. This approach avoids the always tricky comparison of results from different experiments performed at different rapidity windows and/or with different cuts on p_t.

But the real experimental problem lies in the huge *combinatorial background* originating from random combinations of tracks from unrecognized π^o Dalitz decays or γ conversions in the same event. When a track of this origin is lost, the remaining partner contributes to the

[4)]A distance greater than 8 SLT grid pixels between ring center candidates is actually required. This corresponds to the quoted opening angle of 32 mrad.

Meson (decay channel)	$(d\sigma/dy)/(d\sigma_{\pi^o}/dy)_{y_{cm}=0}$	$\mathbf{BR}_{e^+e^-}$	$\epsilon_{\mathbf{m>200}}$	$\mathbf{e^+e^-/\pi^o}$ (10^{-5}) no $p_\perp$ cut	$p_\perp > 200$
$\eta \to e^+e^-\gamma$	0.1	$5.02\ 10^{-3}$	0.075	3.75	1.69
$\eta' \to e^+e^-\gamma$	0.042	$6.5\ 10^{-4}$	0.22	0.60	0.36
$\omega \to e^+e^-\pi^o$	0.15	$5.9\ 10^{-4}$	0.20	1.74	1.04
Total continuum				6.09	3.09
$\omega \to e^+e^-$		$7.1\ 10^{-5}$	-	1.07	0.86
$\rho \to e^+e^-$	0.15	$4.4\ 10^{-5}$	-	0.66	0.53
$\phi \to e^+e^-$	0.0081	$3.1\ 10^{-4}$	-	0.25	0.20
Total direct decays				1.98	1.59
Total				8.07	4.68

Table 3.5: Estimate of the e^+e^- production rate from meson decays relative to π_o emission at central rapidity in p-p collisions. $\epsilon_{m>200}$ represents the fraction of the e^+e^- yield above mass $m > 0.2$ GeV/c^2.

combinatorial background[5)].

Below we give an estimate of the expected signal from the decay processes mentioned in Table 3.5 and also of the combinatorial background expected from the π^o and γ conversion yield.

Expected signal/event.

We can readily estimate the expected yield of e^+e^- pairs per event within the CERES acceptance from the known hadronic decay processes in Table 3.5. The number of e^+e^- pairs per event with mass $m > 0.2\ GeV/c^2$ can be expressed as

$$N_{m>0.2} = \left(\sum_i \frac{d\sigma_i/dy}{d\sigma_{\pi^0}/dy} \cdot BR_{e+e-} \cdot \epsilon_{m>200} \right) \left(\frac{N_{\pi^o}}{N_{ch}} \right) \left(\frac{dN_{ch}}{dy} \right) \chi \qquad (3.4)$$

where we have included the π^o -to-charged-multiplicity ratio (equal to 0.44±0.02 [96]) and the average charged multiplicity per unit of rapidity, dN_{ch}/dy, which amounts to 125 in central S-Au collisions in the CERES acceptance. χ represents the open pair acceptance of the spectrometer (~ 0.10 [74]), and the sum runs over the relevant decay processes, $i = \eta, \eta', \rho, \omega, \phi$. Putting all these numbers together we arrive at an expected signal of $N_{m>0.2} \sim 5.7 \times 10^{-4}$ e^+e^- pairs per event. If we include the p_t cut on single tracks we get $N_{m>0.2,p_t>0.2} \sim 3.3 \times 10^{-4}$ e^+e^- pairs per event.

[5)]Tracks are primarily lost by the p_t cut of 200 MeV. They can also be lost by missing one or both rings. A ring can be distorted beyond recognition by multiple scattering of the parent electron in the radiator or by the cut-off in the minimum number of hits required by the analysis software. Hits are lost because of the spokes, because of dead pads or by hit pile-up.

Expected combinatorial background/event.

On top of this extremely weak hadronic signal we have an overwhelming yield of dielectrons from π^o Dalitz decays and γ conversions. With a 100% pair reconstruction efficiency this would not pose any problem. However in real experimental conditions they will contribute to the combinatorial background when one of the tracks of the pair is lost. Due to their high production probability, Dalitzes and conversions represent the *main* source of combinatorial background.

z (cm)	**Component**	**Material**	**X** (cm)	**X$_o$** (cm)	**X/X$_o$** (%)
0	Segmented target	Au	40x50 10^{-4}	0.334	1.29$^{1)}$
	Target support foils (50%)	mylar	40x6 10^{-4}	28.7	0.04
7.4	Si drift detector	Si	280 10^{-4}	9.36	0.30
	Si drift det. protection foils	mylar	2x30 10^{-4}	28.7	0.02
	Si drift det. ceramics bars		635 10^{-4}		0.20$^{1)}$
9.1	Si pad detector	Si	300 10^{-4}	9.36	0.32
	Si pad det. protection foil	mylar	160 10^{-4}	28.7	0.06
10	Target zone	Air	10	30420	0.03
10	Radiator 1 entrance window	mylar	2x50 10^{-4}	28.7	0.03
88	Radiator 1 gas (50%)	CH_4 at 50^{o}C	88	79102	0.06
	Total				2.35

Table 3.6: List of materials and corresponding radiation length in the CERES spectrometer used during the S+Au run of April 1992.

1) The effective target radiation length is given by half the thickness of one disk plus some small contribution from other disks. The number quoted includes this effect which has been determined from a Monte Carlo simulation [75].

π^o **Dalitz decays:** The number of expected π^o Dalitz decays per event is easily evaluated as

$$N_{Dal} = n_{\pi^o} BR(\pi^o \to e^+e^-\gamma) \quad (3.5)$$

where n_{π^o} is the π^o yield within the spectrometer acceptance, given by

$$n_{\pi^o} = \frac{N_{\pi^o}}{N_{ch}} \frac{dN_{ch}}{dy} \Delta y \quad (3.6)$$

Using the CERES rapidity window, $\Delta y = 0.55$, we obtain that the Dalitz yield per event is $N_{Dal} \sim 0.4$

Conversions: The net yield of conversion pairs depends on the experimental set-up through the total amount of material present in the trajectory of the photons. Table 3.6 lists the

	pairs/event
Signal ($m > 0.2$)	6×10^{-4}
($m > 0.2$ & $p_t > 0.2$)	3×10^{-4}
π^o Dalitz	0.4
γ conversions	1.6
combinatorial pairs (no cuts)	2
comb. pairs ($p_t > 0.2$)	0.13
comb. pairs ($m > 0.2$ & $p_t > 0.2$)	0.11

Table 3.7: Expected e^+e^- pairs per event from the signal and the main physical background sources relevant to CERES, π^o Dalitz decays and γ conversions.

different materials present in the CERES set-up for the 1992 heavy ion run. The total radiation length up to the RICH1 radiator amounts to $0.024X_o$. The conversion yield can be expressed as [116]

$$N_{conv} = n_\gamma \frac{7}{9} \frac{X}{X_o} \tag{3.7}$$

and the gamma yield n_γ can be related to the π^o yield as

$$n_\gamma = \frac{N_\gamma}{N_{\pi^o}} n_{\pi^o} \tag{3.8}$$

with $N_\gamma / N_{\pi^o} = 2.25$ as measured by HELIOS [117]. Thus the expected number of conversions per event is $N_{conv} \sim 1.6$

From the number of gamma conversions and π^o Dalitz decays per event just calculated, $N_{conv} + N_{Dal} \sim 2$/event, we can easily estimate the combinatorial background from such sources. Two pairs per event of such origin amount to 4 tracks per event. The total number of pairs that can be formed from 4 tracks is 6 and, therefore, the additional strictly combinatorial pairs is 4. Half of these will be of unlike sign type which represent the background to the signal. We have thus 2 unlike–sign pairs per event of pure combinatorial origin. The signal-to-background ratio (S/B) at this level is thus $\sim 3 \times 10^{-4}$.

Since single tracks from Dalitz and conversion pairs are rather soft compared to those from the heavier mesons, a $p_t > 200$ MeV/c cut on single electron tracks is an extremely useful rejection of pairs of combinatorial origin. Only 26% of π^o and γ decays will result in a pair with one track with $p_t > 200$ MeV/c and only 5% of them will have both tracks with $p_t > 200$ MeV/c. Thus, if we form pairs only with tracks with a $p_t > 200$ MeV/c, the 4 tracks per event of combinatorial origin are reduced to 0.72 tracks per event. Assuming a poissonian distribution $P(n;\mu)$ for the number of tracks per event with $\mu = 0.72$, the number of pairs we can form is

$$N_p = \sum_{n=2}^{\infty} P(n;\mu)\,\frac{n(n-1)}{2} = \frac{\mu^2}{2} \tag{3.9}$$

which gives 0.13 of un-like sign type. The p_t cut alone has reduced the combinatorial background by a factor of 15, while reducing the signal by a factor of 2. To be able to really compare our combinatorial contamination to the signal we have to apply the same mass cut as we have done in defining the signal, that is, we have to consider only those combinatorial pairs with $m > 200$ MeV/c^2. This mass cut reduces them by a 15%, leaving 0.11 per event. The overall effect of the mass and p_t cut is reducing the combinatorial background by a factor of 19 and the signal by a factor of 2, resulting in an improvement of a factor of approximately 10 in the S/B. The situation is summarized in Table 3.7.

Though both the mass and p_t cuts improve considerably the S/B ratio, this is still not enough since we have to be sensitive to a signal which is three orders of magnitude weaker than the background. We need an efficient further rejection of the remaining background. We will come this topic in more depth in Section 5.2 when we describe in detail the data analysis procedure.

Chapter 4

The Monte Carlo e^+e^- -pair generator

In absence of *new physics* the relevant processes in the dielectron invariant mass range covered by CERES are the known decays of the pseudo-scalar and vector mesons mentioned in Table 3.5. The production and decay of these processes have been simulated by a Monte Carlo generator in order to determine the expected global yield and to produce a differential invariant mass distribution from the *known physics* to compare with the data. I next describe the different particle production mechanisms and decay parameterizations modeled in the CERES Monte Carlo generator.

4.1 Relative particle-production cross sections.

The Monte Carlo generates e^+e^- pairs from the decay processes quoted in Table 4.1 over the whole kinematic phase space [118]. The parent-particle yields are proportional to their total cross sections as measured in p-p collisions at 450 GeV by NA27 [96]. The e^+e^- pairs are generated according to the proper branching ratios following the decay laws mentioned in the next section. The difference between the symmetric p-p collisions and the asymmetric S+Au system is embedded in the rapidity distributions used in the generation of the parent particles. These are generated according to the Bourquin-Gaillard (BG) parameterization [119] which links the particle-production invariant cross section $d^3\sigma/d\vec{p}$ with the rapidity and transverse momentum of the produced particle. Originally proposed to describe the data available at the time (1976)[1)], this parameterization has well stood the advent of a wealth of new data at higher energies. However we have actually used a somewhat improved version of the original BG parameterization for the reasons described below.

4.1.1 Parameterization of the particle-production cross sections.

The original BG expression reads [119]:

[1)]The data available at that time was from the PS, AGS and ISR, covering a CM energy range of $6 < \sqrt{s} < 63$ GeV.

Decay channel	$\sigma_{\mathbf{tot}}$ (mb)	σ/σ_{π^o}	$\mathbf{BR}_{e^+e^-}$
$\pi^o \rightarrow e^+e^-\gamma$	127 ± 3.2	1	$11.98\ 10^{-3}$
$\eta \rightarrow e^+e^-\gamma$	9.8 ± 0.6	0.077	$5.02\ 10^{-3}$
$\eta' \rightarrow e^+e^-\gamma$	~ 3.3	0.026	$6.5\ 10^{-4}$
$\omega \rightarrow e^+e^-\pi_o$	12.8 ± 0.8	0.101	$5.9\ 10^{-4}$
$\rightarrow e^+e^-$			$7.1\ 10^{-5}$
$\rho \rightarrow e^+e^-$	12.6 ± 0.6	0.099	$4.4\ 10^{-5}$
$\phi \rightarrow e^+e^-$	0.62 ± 0.06	0.005	$3.1\ 10^{-4}$

Table 4.1: Values of the total cross sections and branching ratios into e^+e^- of the hadron decay processes included in the CERES Monte Carlo generator.

$$E\frac{d^3\sigma}{d\vec{p}} = \left(\frac{A}{E_\perp + 2} \right)^{12.3} f(y) \begin{cases} e^{-p_\perp}, & \text{for } p_\perp < 1\ GeV/c \\ e^{-23(p_\perp - 1)/\sqrt{s}-1} & \text{for } p_\perp > 1\ GeV/c \end{cases} \tag{4.1}$$

where A is a normalization constant and $f(y)$ is given by

$$f(y) = e^{-\frac{5.13}{Y^{0.38}}} \tag{4.2}$$

where

$$Y = y^{max} - y = ln\left(\frac{E^{max} + P_L^{max}}{E + P_L} \right) \tag{4.3}$$

with E^{max} and P_L^{max} the maximum allowed particle energy and longitudinal momentum respectively,

$$E^{max} = \sqrt{\frac{s}{4} + m^2} \tag{4.4}$$

$$P_L^{max} = \sqrt{P_{max}^2 - P_T^2} \tag{4.5}$$

The main feature of equation (4.1) is that it includes p_t and y, which are kinematically related, in a single expression. However it shows an inconsistency in the rapidity distribution of the produced particles: it produces an unphysical cusp at y=0 as shown in figure 4.1. The origin of this cusp comes from the assumptions made about the dependence of $f(y)$ on y. In order to eliminate this cusp, while keeping the link between p_t and y, we have changed the function $f(y)$ as follows [120],

$$f(y) = e^{-\frac{y^2}{2Y^2}} \tag{4.6}$$

and therefore an improved version of $d^3\sigma/d\vec{p}$ is

$$E\frac{d^3\sigma}{d\vec{p}} = \left(\frac{A}{E_\perp + 2} \right)^{12.3} e^{-\frac{y^2}{2Y^2}} \begin{cases} e^{-p_\perp}, & \text{for } p_\perp < 1\ GeV/c \\ e^{-23(p_\perp - 1)/\sqrt{s}-1} & \text{for } p_\perp > 1\ GeV/c \end{cases} \tag{4.7}$$

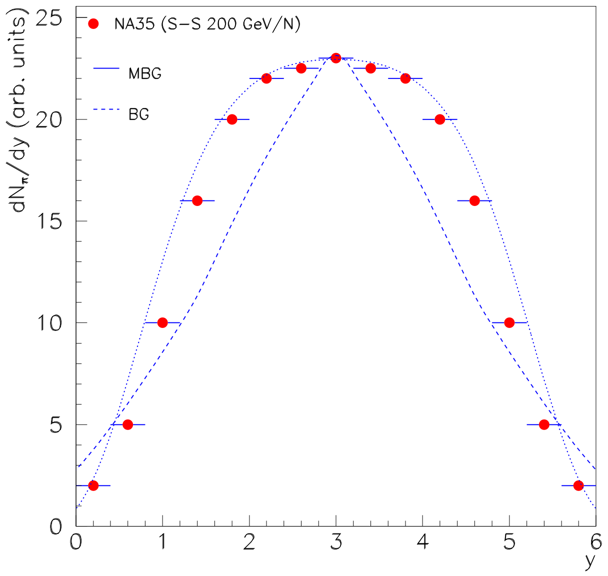

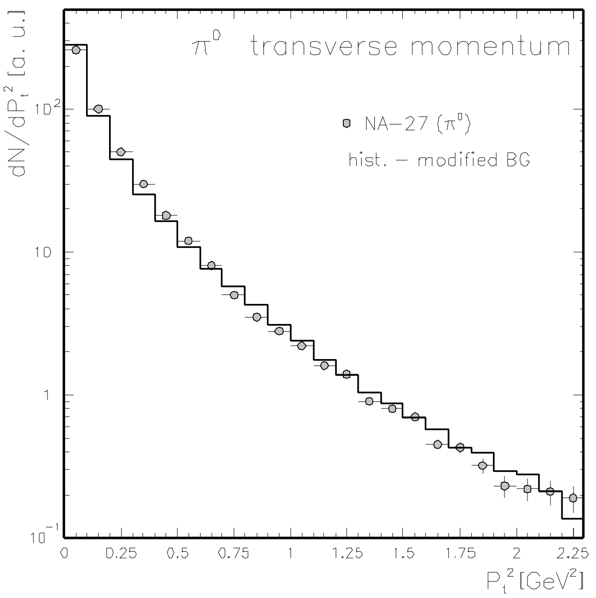

Figure 4.1: **Left:** Rapidity distribution of pions produced according to Bourquin-Gaillard (BG) parameterization, equation (4.1), and according to the modified Bourquin-Gaillard (MBG), equation (4.7). The superimposed data correspond to S-S collisions at 200 GeV/n measured by NA35. **Right:** p_t distribution from π^o 's generated according the modified BG parameterization. Data of p-p collisions at 450 GeV/c from NA27 is superimposed.

The modified Bourquin-Gaillard (MBG) expression (4.7) reproduces very well a large amount of momentum and rapidity distributions measured in p-p and nucleus–nucleus collisions. As an example we show in the left plot of Figure 4.1 the rapidity distributions obtained from both parameterizations compared to the measured rapidity distribution of negative pions produced in S-S collisions at 200 GeV/nucleon measured by NA35 [121]. Note that not only the cusp has been eliminated, but the shape of the experimental rapidity distribution is much better reproduced. The right plot of Figure 4.1 shows the p_t distribution of π^o mesons produced in p-p collisions at 450 GeV/c measured by NA27 [96] compared with the MBG prediction. We have used the modified version (4.7) to generate the processes of Table 4.1.

4.2 Functional form of the different particle decays.

The dependence on the e^+e^- invariant mass of the cross section for the decay processes mentioned in (2.1) and (2.2) is quite different in both cases. Dalitz decay modes follow an elementary QED cross section modified by the relevant form factor, while direct decay modes are described by a resonance shape. Several peculiarities in the way these decays were actually generated deserve further mention.

Direct decay into e^+e^-

The exact shape of the ρ decay into e^+e^- has been calculated by G. J. Gounaris and J. J. Sakurai [122]. A simplified version of their result, where one keeps only those terms relevant in the mass range of the vector meson is

$$F_\rho^{GS}(m) = \frac{N}{m_\rho^2 - m^2 - i\Gamma_\rho \frac{m_\rho^2}{m}\left(\frac{m^2 - 4m_e^2}{m_\rho^2 - 4m_e^2}\right)^{3/2}} \tag{4.8}$$

where N is a normalization constant and we have taken $m_\rho = 769.9$ MeV/c^2 and $\Gamma_\rho = 151.2$ MeV. Equation (4.8) is very similar to a S-wave Breit-Wigner curve[2)] , the main difference being a slight shift of the peak position which amounts to 14 MeV for the ρ.

We have used the Gounaris-Sakurai parameterization for the ρ shape, and the Breit-Wigner shape for the ω and ϕ. This is justified because the shape of the narrower ω and ϕ resonances is completely dominated by the spectrometer mass resolution, and the slight difference between the two parameterizations becomes irrelevant.

The angular distribution of the final dilepton depends on the polarization of the vector parent particle, which we do not know. The exchanged photon carries one unit of angular momentum and in principle we should get a standard $(1+\cos^2\theta)$ angular dependence of the cross section corresponding to the exchange of a transversely polarized photon (or $(1-\cos^2\theta)$ from a longitudinally polarized one). For the actual angular distribution of the decay products we have used a $1 + \cos^2\theta$ dependence as suggested by HELIOS data [71, 94].

Dalitz decay modes

The relevant formulae for the Dalitz decay modes have been given in Chapter 2 and we will repeat them here just for completeness. For the Dalitz decays of the π^o , η and η' we have used the elementary QED Kroll-Wada expression [80] multiplied by the proper form factor,

$$\frac{d\sigma_i}{dm_{e^+e^-}} \propto \frac{1}{m_{e^+e^-}}\sqrt{1-\frac{4m_e^2}{m_{e^+e^-}^2}}\left(1+\frac{2m_e^2}{m_{e^+e^-}^2}\right)\left(1-\frac{m_{e^+e^-}^2}{m_i^2}\right)^3 |F(m_{e^+e^-})|^2 \tag{4.9}$$

We have used pole-type form factors inspired by the VMD model,

$$F = \frac{\Lambda^2}{\Lambda^2 - m_{l^+l^-}^2} \tag{4.10}$$

For the $\omega \to \pi^o e^+e^-$ decay we have (see Section 2.1.1),

[2)] A Breit-Wigner shape of a resonance of mass m_v is given by

$$F_v^{BW}(m) = \frac{1}{\sqrt{\pi}}\frac{\sqrt{\Gamma_v/2}}{m - m_v + i\Gamma_v/2}$$

$$\frac{d\sigma}{dm_{e^+e^-}} \propto \frac{1}{m_{e^+e^-}} \sqrt{1 - \frac{4m_e^2}{m_{e^+e^-}^2}} \left(1 + \frac{2m_e^2}{m_{e^+e^-}^2}\right) \times$$
$$\left[\left(1 + \frac{m_{e^+e^-}^2}{m_\omega^2 - m_\pi^2}\right)^2 - \frac{4m_\omega^2 m_{e^+e^-}^2}{(m_\omega^2 - m_\pi^2)^2}\right]^{3/2} |F(m_{e^+e^-})|^2 \qquad (4.11)$$

As mentioned in Chapter 2, the VMD does not reproduce correctly the ω form factor and therefore we have used a single-pole fit to the experimental data from the Lepton-G collaboration [123] shown as curve 1 in Figure 2.5. Table 4.2 summarizes the pole values used in the form factors of the different processes (taken from [79]).

Meson	Λ (GeV)
$\pi^o \rightarrow e^+e^-\gamma$	0.426 ± 0.06
$\eta \rightarrow e^+e^-\gamma$	0.720 ± 0.09
$\eta' \rightarrow e^+e^-\gamma$	0.770 ± 0.09
$\omega \rightarrow e^+e^-\pi_o$	0.650 ± 0.03

Table 4.2: Λ values used in the pole-type form factors of equation 4.10

The angular distribution for the Dalitz decay modes of the pseudoscalar mesons is in principle isotropic since we start from an L=S=0 state.

4.3 Invariant mass distribution from the Monte-Carlo generator.

The decay processes mentioned in the last sections have been combined into a "cocktail" which gives the theoretical expectation of the shape of the dielectron invariant mass spectrum as well as the absolute yield. A key feature of the Bourquin-Gaillard parameterization is that it incorporates a dependence on $\sqrt{s}$, which allows to use it successfully in the description of data taken at different energies. In the case of nucleus–nucleus collisions the CM energy is calculated from the participant nucleons only (see Figure 1.3) using a simple geometrical model which has proven to reproduce qualitatively the gross features of the experimental results ([14] and references therein). If we take the central collision of a beam nucleus with mass number A and a target nucleus with mass number B (B>A), the number of target participants can be expressed as

$$N_t = B - A[(B/A)^{2/3} - 1]^{3/2} \qquad (4.12)$$

and the CM energy of the collision is

$$\sqrt{s} = [(Am)^2 + (N_t m)^2 + 2E_{beam} N_t m]^2 \qquad (4.13)$$

where m is the nucleon mass. To use the Bourquin-Gaillard parameterization in the case of S-Au collisions at 200 GeV/nucleon we have used $\sqrt{s}$ calculated as in (4.13).

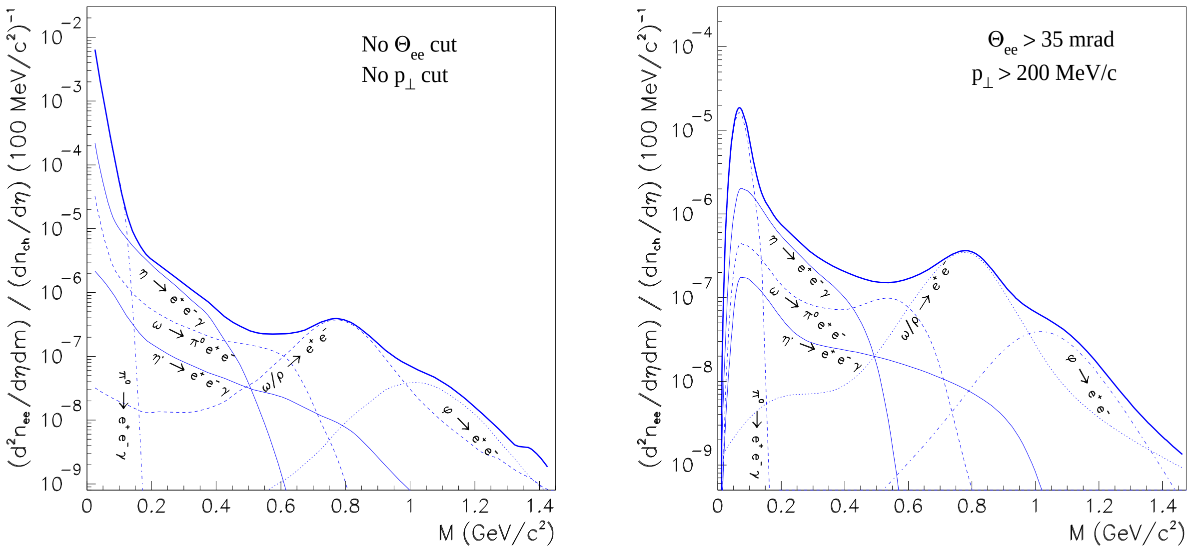

Figure 4.2: Invariant mass distribution of the hadronic decays known to contribute to the CERES mass range. The yield has been scaled by the measured average charged particle multiplicity in S-Au collisions.

The normalization of the Monte Carlo spectrum is done in a similar way as we calculated the expected signal in equation (3.4) in Section 3.2 . The individual contributions are generated according to the measured yield relative to the π^o , σ_i/σ_{π^o}, as quoted in Table 4.1[3)]. Thus, the generator provides in a direct way the e^+e^- yield per π^o , $(d^2N_{e^+e^-}/dmd\eta)/(dN_{\pi^o}/d\eta)$. Since we have chosen to normalize the data as number of e^+e^- pairs per charged-particle rapidity density, the same normalization is applied to the Monte Carlo by multiplying it by the measured π^o yield per charged particle, $N_{\pi^o}/N_{ch} = 0.44 \pm 0.02$ [96]. Figure 4.2 shows the cocktail of the individual contributions to the dielectron invariant mass spectrum in the mass range $m_{e^+e^-} \leq 1.5$ GeV/c^2 in the CERES geometrical acceptance. The left plot includes the contributions within the CERES acceptance without any kinematical cuts. The effect of the kinematical cuts used in the data analysis ($p_t >$ 200MeV/c, opening angle $>$ 35 mrad, see Chapter 5) can be seen in the right plot. These cuts reduce the contribution of the π^o by

[3)]There are no measurements of the η' total cross section. The value quoted is obtained from the $\sigma_\eta/\sigma_{\pi^0}$ ratio measured by NA27 and extrapolating using the Bourquin-Gaillard parameterization. The same problem arises with its branching ratio into e^+e^- . Assuming $e\mu$ universality we can express

$$\frac{\Gamma(\eta' \to e^+e^-\gamma)}{\Gamma_{total}} = \frac{\Gamma(\omega \to e^+e^-\pi^o)}{\Gamma(\omega \to \mu^+\mu^-\pi^o)} \times \frac{\Gamma(\eta' \to \mu^+\mu^-\gamma)}{\Gamma_{total}}$$

where all the factors in the r.h.s. are known.

almost three orders of magnitude, while the contributions to pair invariant masses greater than 200 MeV/c^2 is reduced by less than a factor of 2. All the individual contributions have been convoluted with the measured mass resolution of the spectrometer, which is of the order of 10% at the ρ/ω mass.

4.3.1 Comparison of the Monte Carlo results with experimental data.

A comparison between the generated dielectron invariant mass spectrum and CERES data on p-Be at 450 GeV/c is shown in Figure 4.3. The vertical bars in each bin of the plot show the statistical error and the small brackets the linear combination of the statistical and systematic errors. The shaded area represents the uncertainty in the Monte Carlo generator due to the errors in the experimental cross sections and decay widths used. The figure shows an excellent agreement with the data within the present errors. Results from CERES on p-Au collisions at 400 GeV/c show that the dielectron yield in the p-nucleus case is also well reproduced by the conventional p-p sources [127]. This provides a confirmation that the generator reproduces the dielectron yield from the "conventional" hadronic sources and gives the basis to use it as a comparison with the spectrum obtained in S-Au collisions. It also confirms the finding of HELIOS [94] that there is no need to call for anomalous e^+e^- pairs in p-p collisions.

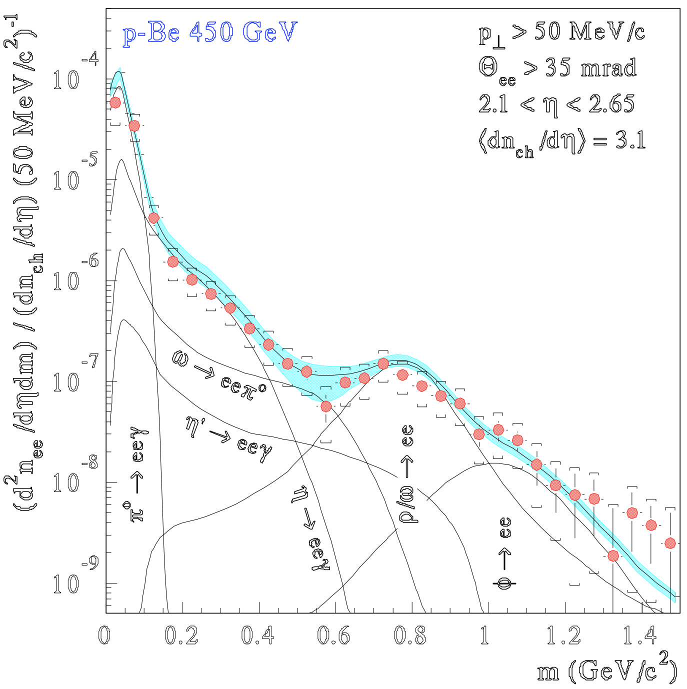

Figure 4.3: Comparison between the generated dielectron invariant mass spectrum and CERES data on p-Be at 450 GeV/c.

Chapter 5

The $S - Au$ data sample and analysis

5.1 The 1992 heavy ion running conditions.

The results presented in the next chapter were obtained from the analysis of the data from the first CERES heavy ion dedicated run. The data were taken during April 1992 under two different conditions: untriggered data with only a multiplicity threshold provided by the SiPAD (FLT data), and triggered data with the SLT described in Section 3.1.6. This chapter gives an account of the CERES running set-up used in the 1992 heavy ion run as well as a detailed description of the data analysis procedure.

5.1.1 The target.

The requirement of the target is twofold: On one hand we require a high interaction rate to collect sufficient statistics from a very weak signal and a limited beam intensity. This would point towards using a thick target. On the other hand we must minimize conversions and secondary interactions, which require a thin target. In this spirit, a segmented target, which fulfills both needs, was used in the 1992 heavy ion run. It consisted of 40 disks of gold separated by 1.6 mm, 50 μm thick and 600 μm in diameter each, corresponding to a total interaction length of $X/X_{Au} \sim 5\%$. The gold disks were glued to 5 μm thick mylar foils acting as support structure. The interaction length of the mylar part amounts to $\sim 0.1\%$ and it is therefore totally negligible.

An infinite spacing between disks would make the effective target thickness for conversions to be half the thickness of the individual disks, 25 μm, or $X/X_{Au} = 0.75\%$. The higher value of $X/X_{Au} = 1.3\%$ quoted in Table 3.6 was determined by Monte Carlo and it reflects the effect of the finite spacing and the finite size of the beam and the target disks. With such geometry, the majority of the secondaries from the interaction in one disk do not hit the next downstream disks. Secondary interactions amounted to $\sim 15\%$ of the total interaction rate.

Beam: ^{32}S at 200 GeV/nucleon	**Target:** Au		
	trigger enrichment E	events	minimum bias equivalent
FLT (16 days)	-	3.041×10^6	3.041×10^6
SLT (7 days)	1.6	2.143×10^6	3.429×10^6

Table 5.1: Data sample of the CERES 1992 heavy ion run. In the case of the second level triggered (SLT) the number of minimum bias equivalent events is calculated from the analyzed sample taking into account the trigger enrichment (see Section 5.2.2 below).

5.1.2 Trigger.

The data in the 1992 run were taken with the two trigger modes described in chapter 3. Part of the data sample was taken with the FLT only and part with the FLT plus the SLT. The total number of events collected with the two trigger modes is summarized in Table 5.1.

In order to eliminate the much higher rate of peripheral interactions giving rise to very low multiplicity events we used a global minimum threshold of $dN_{ch}/d\eta \geq 40$. Further, to enrich the data sample in central collisions, where the interesting physics is expected, a trigger mix was used: low multiplicity events were scaled down by a factor of 4 with respect to the higher multiplicity ones[1)]. The threshold for the high multiplicity events was set to $dN_{ch}/d\eta \geq 125$. Figure 5.1 shows the charged particle multiplicity distribution as seen by CERES before and after correcting for the scaling factor[2)]. In Figure 5.2 we show the difference in shape of the measured charged multiplicity distributions from the FLT and SLT data samples.

On top of the FLT and SLT data samples, MT and UV-lamp triggers were also written to tape. MT triggers are random pulse triggers correlated with the burst signal. MT and UV–lamp triggers were scaled down to amount to approximately 4% of the total data written to tape.

[1)]In parts of the run a scaling factor of 6 or even 10 was used. When taking SLT data the scaling used was 2.

[2)]The dots in the region $dN/d\eta > 125$ have been slightly displaced in the plot for clarity. As no scaling was applied for high multiplicity events, both distributions overlap in this region.

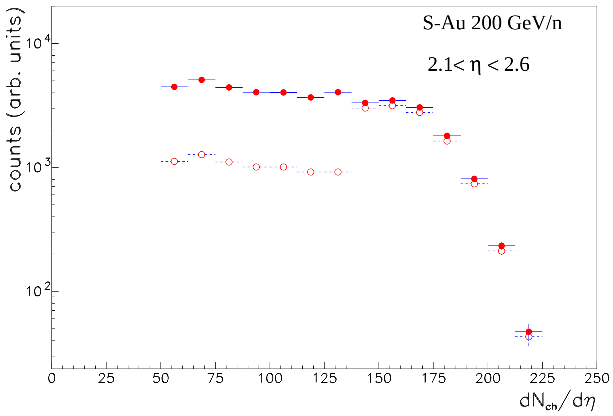

Figure 5.1: Charged particle multiplicity distribution. The white dots represent the actually measured down-scaled distribution. The black dots represent the distribution corrected by the down-scaling factor.

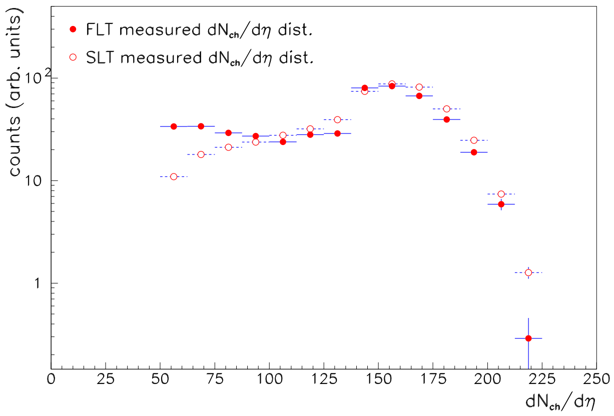

Figure 5.2: Measured charged particle multiplicity distributions from the FLT and SLT data samples. The distributions have been normalized to the same (arbitrary) number of entries to enhance the difference in shape.

Beam intensity and event rate.

The typical beam intensity delivered to CERES from the SPS in heavy ion mode in 1992 was $\sim 1.5 \times 10^6$ S ions per burst. With the CERES effective target thickness of 5% of an interaction length this amounts to a total interaction rate of $\sim$ 7x10^4 per burst[3)]. The typical number of events written to tape per burst at the end of the trigger filter with the 1992 setup was $\sim$ 250 using only the FLT mode, and $\sim$ 170 with SLT triggered data.

5.2 The data analysis procedure.

There are two main tasks that the data analysis has to perform: the first one is the event pattern recognition, namely finding the rings in RICH1 and RICH2 with the highest possible efficiency and matching them into tracks. Second, we must identify pairs and single tracks originating from gamma conversions and π^o Dalitz decays to minimize the combinatorial background. This is the most critical step of the analysis. The remaining tracks are then combined into pairs giving rise to an unlike-sign (e^+e^-) pair sample and a like-sign (e^+e^+ and e^-e^-) pair sample. The remaining combinatorial background in the unlike-sign sample is estimated to be the total like-sign sample, so the net signal is extracted as the number of unlike-sign pairs minus the number of like-sign ones. In this section we explain the data analysis procedure from the unpacking of the raw event up to the extraction of the final signal.

[3)]The duration of a burst in the SPS in heavy ion mode is 4.8 sec., with a repetition rate of 19.2 sec.

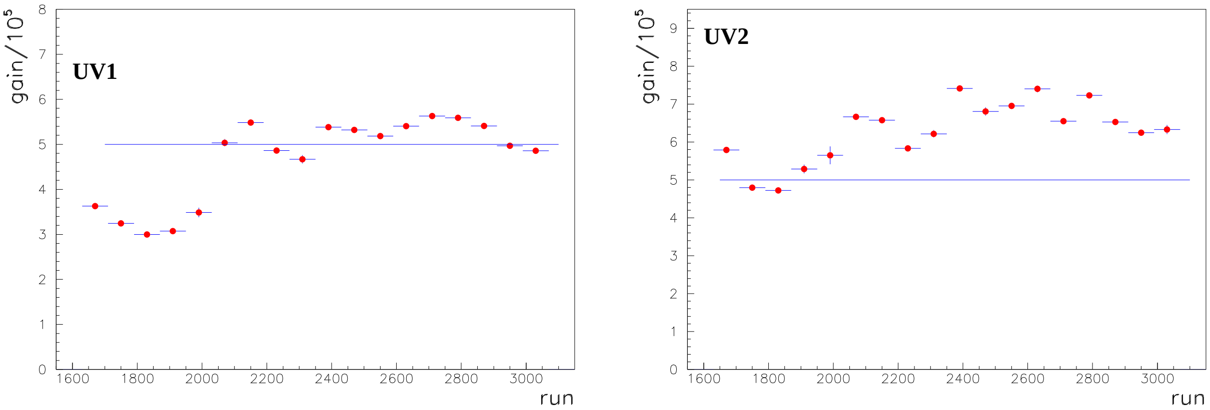

Figure 5.3: Variation of the UV detectors gain along the Sulphur run period. An off-line gain correction brings the run gain to a nominal of 5×10^5, shown as the horizontal line in the plots.

5.2.1 Pattern recognition.

Essentially, a raw CERES event consists of the location and pulse height of each of the pads of the UV detectors' pad plane and the (r,ϕ) coordinates and amplitude of the hits in the SiDC. A preprocessing of the event at the pad level is performed at unpacking time, before entering the pattern recognition proper. This preprocessing consists of two tasks: gain equilibration and event clean-up.

Event unpacking and preprocessing.

a) Gain equilibration.

There are two factors which affect the gain of the UV detectors and which are reflected in the response of the individual pads. There are local (spatial) gain variations along the area of the detectors due to the detector electronics and mechanical tolerances of the different amplification steps. On top of this there are temporal gain variations during the data taking period (20 days in the 1992 heavy ion run) due to changes in temperature, atmospheric pressure and voltage settings in the amplification gaps (see Figure 5.3). A correction factor for each pad, which takes into account both contributions, has to be introduced to improve the performance of the pattern recognition software as explained below. The temporal fluctuations are corrected on a tape-by-tape basis by a factor G^o/G^t. G^o is a nominal (reference) gain (set to 5×10^5)[4)], and G^t is the tape average gain. This factor corrects for the deviation of the current tape gain from the constant nominal gain. The local gain correction must take into account on a pad-by-pad basis the deviation of the response of each individual pad from the global pad average. Therefore the average amplitude of each pad over several tapes g_i has

[4)]One could also use the global average of all the G^t. For technical reasons connected with saving computing time, the mentioned nominal value was used.

been obtained, along with the global average amplitude from all pads, $\bar{g} = \sum g_i/N$, with N the number of pads. The factor $\bar{g}/g_i$ is the correction we need. When the event is unpacked for the data analysis, the raw amplitude of each pad recorded on tape is corrected as

$$a_i^{corr} = \frac{G^o}{G^t}\frac{\bar{g}}{g_i}\,a_i$$

This correction averages out the local and temporal gain variations and reflects the real response of the pad to an incoming avalanche, reproducing the bell-shape of a photon hit (which typically extends over several pads). The main goal of the gain equilibration is to obtain the real amplitude of the hits, which in turn it is used to calculate the total amplitude of the rings. This quantity is used as a cut to reject overlapping rings in RICH1 from γ conversions as we will mention below.

b) Event clean-up.

The second preprocessing step is an event clean-up. This is mandated by the hit background present in the events. On top of the genuine UV photon hits from the Čerenkov rings, or from high momentum pions or δ–electrons, we have large clusters of pads fired by highly ionizing particles crossing the detector or by defective electronic modules, and individual pads due to pedestal fluctuations. These clusters have to be removed in order to minimize the number of fake rings that would otherwise result from random combinations of hits.

The clean-up proceeds as follows. First, clusters are found and their mean amplitude calculated. Clusters are defined as connected pad structures with size or total amplitude greater than predefined cutoff values. Care must be taken not to select genuine photon hit pile-up, which is typically bigger than a single hit and has a higher amplitude, as a cluster, since this would result in hit losses that would affect the ring reconstruction efficiency. Values of 100 (80) pads and 1200 (2000) ADC counts for the minimum cluster size and amplitude where found to be optimal in UV1 (UV2). They correspond roughly to 4 times the size of a single hit and 10 times the average hit amplitude, assuring that really extended or abnormally loaded blobs are selected as candidates for rejection. Next a series of cuts on the amplitude and shape of the clusters are applied. The effect of this cleaning method is clearly seen in Figure 5.4. The plot shows the same event before and after the cluster rejection. This event is particularly illustrative since it contains a typical example of each of the three main types of pad clusters we face: an ionizing track characterized by its elongated shape and a high mean amplitude (most of the pads are usually in saturation) which can be seen in the upper left corner, a module with all the pads fired[5)] and characterized by its square geometry as seen in the upper right area of the plot and, third, structureless extended blobs of pads with several pads in saturation.

[5)]Modules can lit up due to a traversing particle as is the case shown in Figure 5.4, or simply by instabilities in the readout electronics. In the latter case the module lits up with a low amplitude, being only recognized by the geometry and not by an unusually high load.

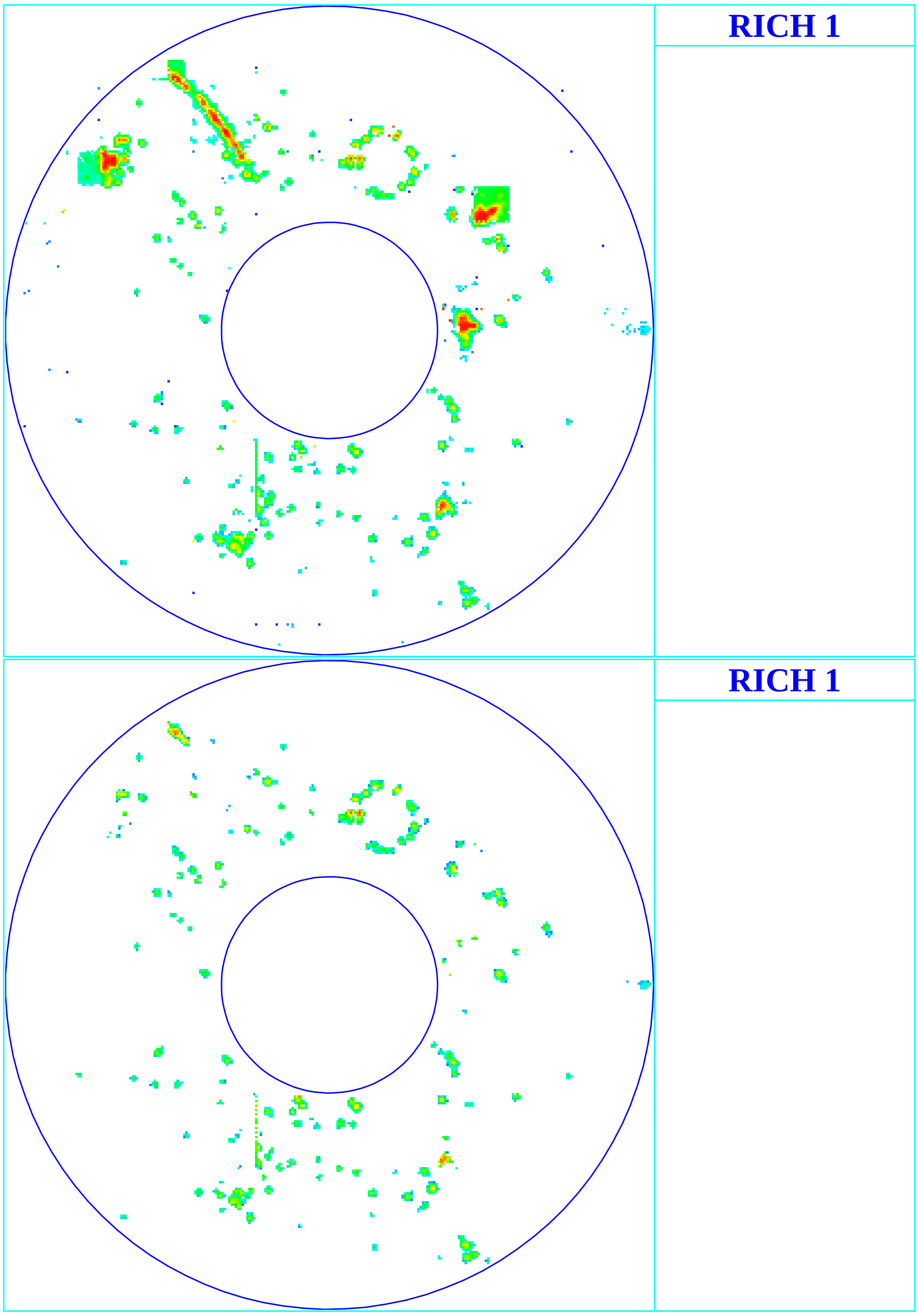

Figure 5.4: A typical S-Au event as seen by the CERES first RICH detector. Unphysical pad clusters due to electronic instabilities or particle tracks traversing the UV detector seen in the raw event (top) are removed by the off-line software (bottom).

Ring candidate search.

The next step in the analysis is to look for electron rings. As we do not have an *a priori* knowledge of the ring centers, the whole detector area has to be searched for ring candidates. The fact that we are looking for rings of a fixed radius can be exploited to use a point–to–ring Hough transformation on the pads: a ring of the nominal asymptotic electron radius is built around each fired pad. Ideally, this transformation would give a clear peak at the center of each ring. The different hit sizes and the single hit resolution results in a somehow spread peak as shown in figure 5.5. A cut on the amplitude of this peak is used to select the candidate rings over the background. To save processing time, the candidate search is first performed in RICH1 and a minimum of two candidates is required to proceed with the event analysis.

Hit reconstruction.

Hits are fitted on the remaining pad clusters located in an area 1.5 times the asymptotic electron ring radius (R_c) around the candidate centers. This saves the time of finding hits all over the detector area and which will not be used further in any ring fit. The hit centers are found by the center of gravity method using a 3×3 pad box. If ξ represents either the x or y coordinates in the pad coordinate system, then the corresponding hit center coordinate ξ_o is given by

$$\xi_o = \frac{\sum_i \xi_i \, a_i}{\sum_i a_i}$$

where i runs over the 9 pads in the box and a_i represents the amplitude of the i*th* pad.

Ring fitting and characterization.

Rings are fitted using the asymptotic ring radius as a fixed value, the candidate position as initial value for their centers and the coordinates of the hits found in the area around the candidate. A minimum of 6 hits is required to fit a ring. This is a compromise to avoid the huge number of fake rings which would otherwise be fitted over background hits while keeping a high ring reconstruction efficiency as the average number of hits per ring is 10.

The ring fit itself is performed by minimizing the distance of the hits around each candidate center to the nominal ring radius R_c. Since in the previous step hits have been found in a wide area around the candidate center, each hit is weighted by a gaussian "potential" when performing the fit. That is, the function to minimize is not the simple linear distance from the hit to the ring radius, d, but instead

$$f = \sum_i -e^{-d_i^2/2\sigma^2}$$

where i runs over the hits entering the fit and σ has been taken to be 1. Thus hits closer to the ring radius weight more in the fit, while far away hits practically do not contribute. The ring radius and center are allowed to vary within a narrow limit, defined by the single

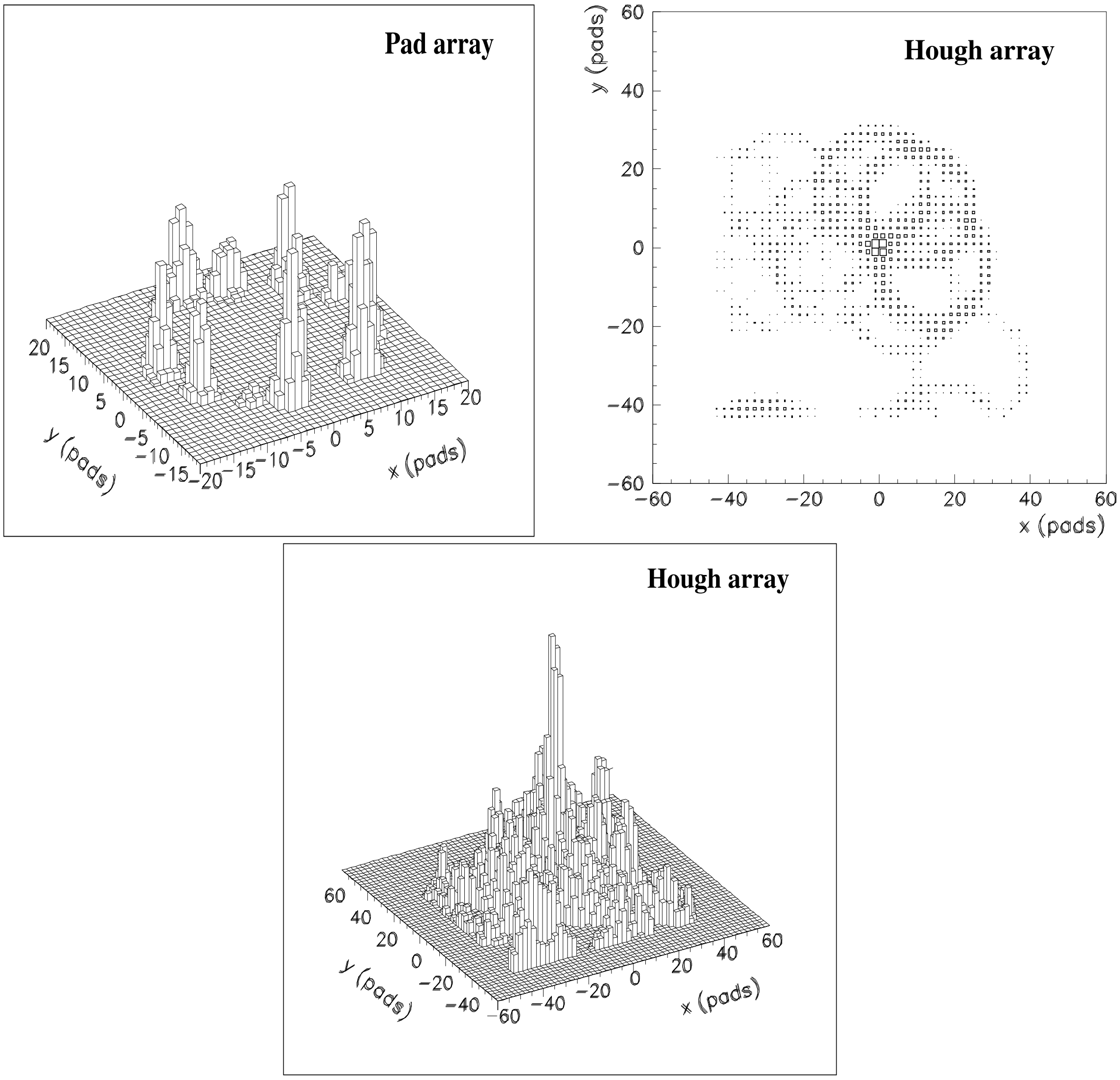

Figure 5.5: An asymptotic electron ring as seen in the pad array (left) and its Hough transformation (right). The Hough transformation gives a peak at the ring center position (bottom).

hit resolution spread, to improve the final ring center position with respect to the rough estimation of the candidate search. Figure 5.6 shows the result of the ring fitting procedure. The candidate centers are shown as the small crosses. Note that in principle all the hits within $1.5\,R_c$ participate in the fit while the weighting procedure just described forces only the closest ones to define the ring.

Since hits from a high energy pion ring together with some background hits can be fitted as a saturated electron ring, a second fit with the radius as a variable parameter between $0.8\,R_c$ and $1.2\,R_c$ is performed on each ring. The ring center position and radius as obtained

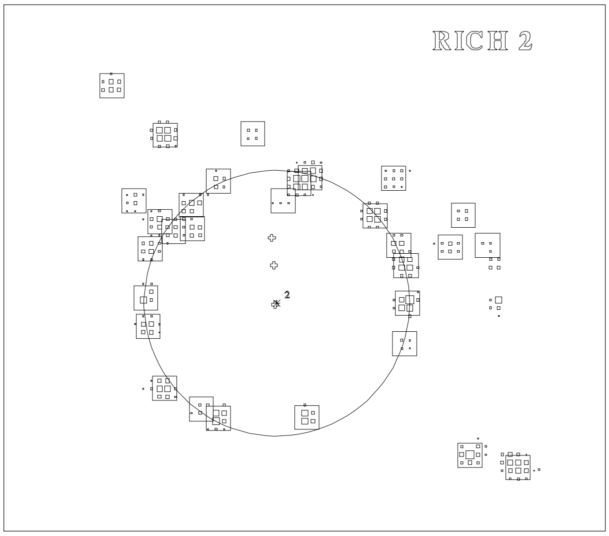

Figure 5.6: Fitted ring in RICH2. The original candidate centers are shown as the crosses. Only one of the three potential candidates survived the Hough peak quality cut or the fitting cuts applied.

from the variable radius fit are stored along with several other ring characteristics for later rejection of fake fits in the extraction of the final signal. A ring is characterized by

- The sigma of the fit, defined as

$$\sigma^2_{fit} = \frac{\sum_i d_i^2}{N-1}$$

  where N is the number of hits in the ring and d_i their distance to the ring radius. σ_{fit} can therefore be interpreted as the mean spread of the hits around the ring circumference, and it gives a quantitative estimation of the ring quality.

- The position and radius obtained from the variable radius fit.

- The number of hits.

- The summed amplitude in a 3×3 and a 7×7 box around the candidate center in the Hough array, and their respective r.m.s. These quantities serve to define the quality of the candidate peak.

- The number of activated pads in a 3 and 6–pad wide annular mask around the ring circumference.

- The summed amplitude of the activated pads in the 6–pad wide mask. This quantity is used to reject double unresolved rings where the probability of loosing hits due to pile-up is high, and an upper cut on the number of hits is not efficient.

- The result of the Kolmogorov and ω^2 [124] statistical tests on the uniformity of the angular distribution of the hits along the ring circumference [6)].

- The two biggest angular gaps between adjacent hits.

Cuts on the distributions of these variables are applied as we will mention below with the aim of selecting genuine electron rings and reject conversions or fake rings.

If a minimum of two rings are found in RICH1, the same ring-search procedure is performed in RICH2. We require a minimum of two rings on each RICH to proceed further.

Track reconstruction.

The rings in both detectors are then matched in search for tracks. For every ring in RICH1, an area in RICH2 centered at the same radial angle, θ, is searched for a matching ring. The magnetic field induces a deflection $\Delta\phi$ on the tracks inversely proportional to their momentum as

$$\Delta\phi = \frac{120}{p} \tag{5.1}$$

where $\Delta\phi$ is in mrad if p is in GeV. The matching area in RICH2 is thus determined by the combined effect of the magnetic field deflection, the multiple scattering and the ring center resolution, which produce the butterfly-like shape as shown in Figure 5.7. For an infinite momentum particle ($\phi_2 - \phi_1 = 0$) the size of the butterfly in the radial direction is given by the ring center resolution of the RICH detectors. As the momentum of the particle decreases, the radial size of the area to be searched becomes larger due to the multiple scattering. In the azimuthal direction the area is limited by a 50 MeV/c p_t cut applied on the single tracks. To recognize conversion patterns, a ring in RICH1 is allowed to match two rings in RICH2 if the resulting tracks have opposite signs. This is illustrated in Figure 5.8 where the actual search area is indicated and where we can see a typical conversion pattern with two rings in RICH2 within the butterfly area of the ring in RICH1. The cases in which an ambiguity exists, i.e., two rings in RICH2 lie within the butterfly of a ring in RICH1 resulting in two tracks of the same sign, are resolved by taking only the track with the best θ match.

Vertex reconstruction.

If at least two tracks have been found, then the interaction vertex is searched for using the track coordinates in RICH1 and the SiDC hit information. The SiDC alone can not determine the interaction vertex since we are using an extended target. Firstly, the z axis is scanned within the limits of the target overall longitudinal dimension, $L_t = 6.5$ cm, in steps of $L_t/500$, while the x and y coordinates are kept to a fixed value of 0. The z value which minimizes

[6)] The ω^2 test, also called Smirnov-vonMises test, follows essentially the same philosophy as the Kolmogorov test but taking into account the *integral* of the difference between the measured distribution and the theoretical one, not just the maximum deviation as Kolmogorov. It is considered to be a more robust test for small statistics.

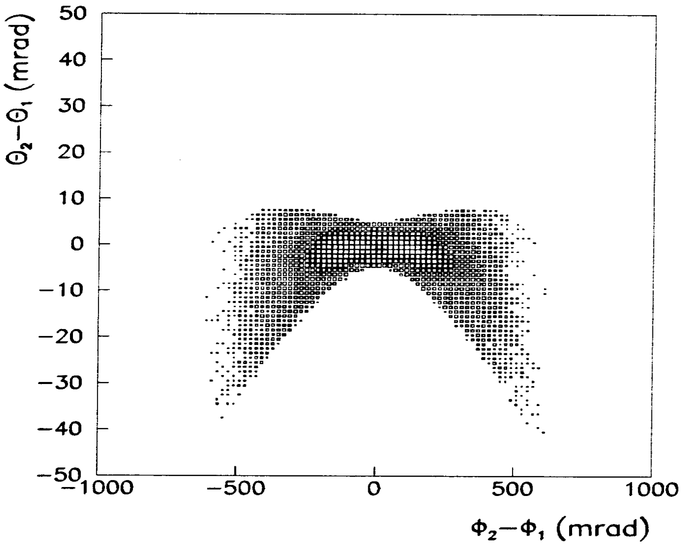

Figure 5.7: Matching of rings between RICH1 and RICH2. The angular displacement results from the combined effect of the magnetic field deflection, the ring center resolution and the multiple scattering.

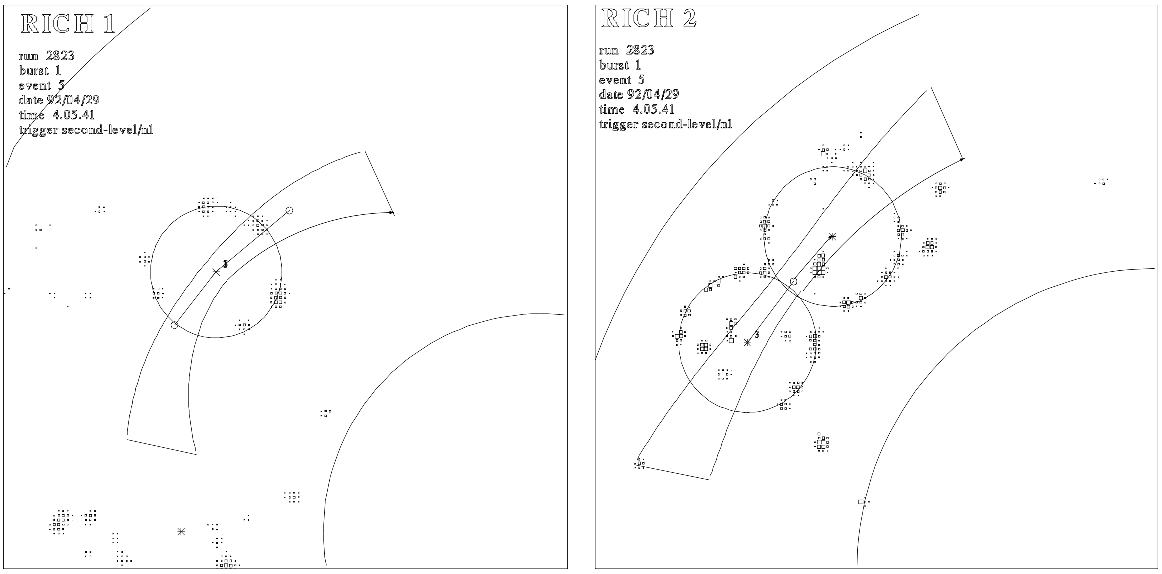

Figure 5.8: The actual butterfly-shaped area used in the analysis to match rings between RICH1 and RICH2. In this event two rings have been found in RICH2 within the search area of the ring in RICH1. Such pattern is identified as a γ conversion.

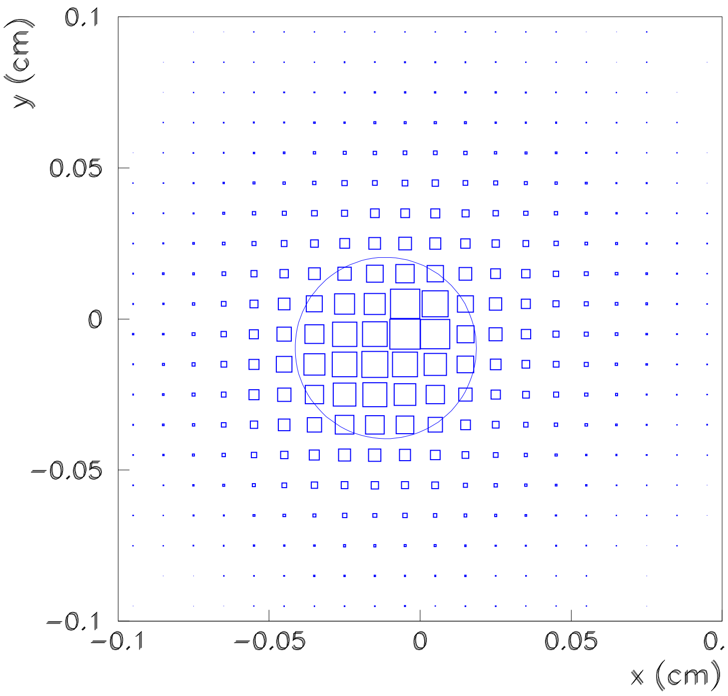

Figure 5.9: Distribution of the fitted vertex position in the x-y plane. The circle shows the position and size of the target disk.

the distance[7)] of all the tracks to their closest SiDC hit at the same time is taken as the vertex z-coordinate candidate value. In a final global fit x, y and z are allowed to vary within pre-specified limits to find the (x, y, z) point which minimizes the above mentioned function. This point is taken as the event interaction vertex. The reconstructed vertex position in the x-y plane can be seen in Figure 5.9 where the superimposed circle shows the position and size of the target disk.[8)]

5.2.2 Extraction of the signal.

At this level, tracks are combined to form pairs. In order to identify the weak signal among the still strong yield of combinatorial pairs, a series of additional cuts on the ring, track and pair level are applied. We have followed the philosophy of keeping the analysis as versatile as possible, applying the cuts only at the very end of the analysis chain. This approach ensures that the signal is not lost by any cut at an intermediate step and allows to optimize the cuts

[7)] Actually a function F of the individual track distances is minimized, $F = \sum_i e^{-d_i^2/2\sigma^2}$ where i runs over all the tracks in the event. Thus each track is weighted in a way inversely proportional to the quality of its SiDC match.

[8)] In actual running conditions the target was found to be actually displaced by approximately -0.1 mm in both x and y from its nominal (0,0) position.

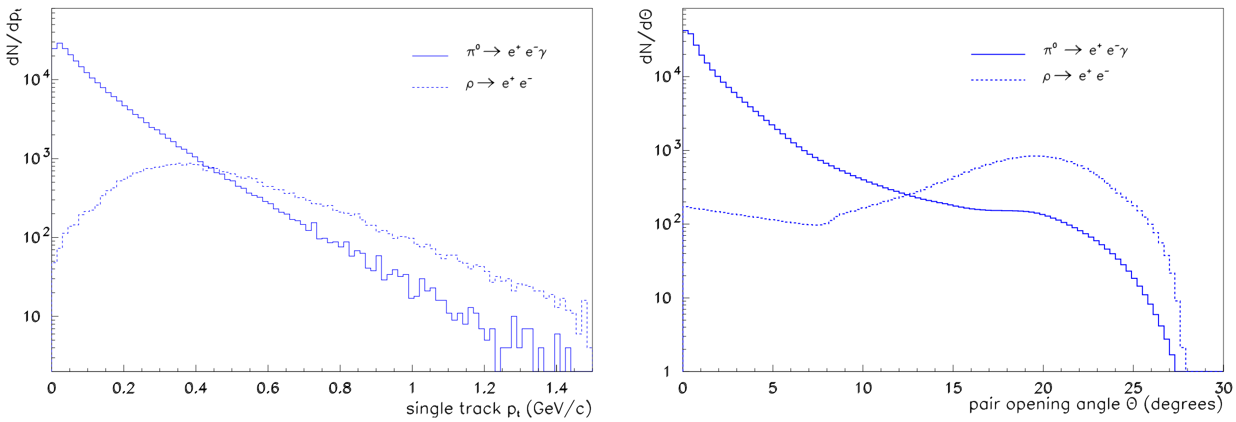

Figure 5.10: p_t of single tracks and opening angle distributions of the e^+e^- pair from the π^o Dalitz and $\rho \to e^+e^-$ decays.

globally.

We can distinguish two kinds of cuts: those based on the physical properties of the decay processes –angular cut, p_t cut– and those based on the signatures left by the particles in the detector –based on the characteristics of the rings – and which are related to the detector design specifications.

At the ring level we apply what we will call *ring quality cuts* to discriminate real rings from fake ones fitted over remaining background clusters. For these cuts the quantities used to characterize a ring as mentioned in the previous section are used. Essentially, these cuts are aimed at identifying rings with a uniform angular distribution of hits along their circumference, with a well defined candidate peak from the Hough transformation and with a summed amplitude and number of hits between the expected limits for a single ring[9)].

The next step is to identify pairs from γ conversions and π^o Dalitz decays. Here we can exploit the physical characteristics of such decays through the pair opening angle, Θ, defined as the angular distance between the two rings in RICH1. The small opening angle Θ of a γ conversion or a π^o Dalitz pair gives rise to two unresolved (overlapping) rings in RICH1 opened by the magnetic field in RICH2, producing a typical V pattern, or to two close rings in RICH1. Thus, tracks belonging to pairs with an opening angle of $\Theta < 2$ degrees are not used for further pairing on the grounds that they probably belong to a conversion or π^o Dalitz decay. In order to increase the recognition efficiency of conversions and π^o Dalitz pairs, the second track of the pair is allowed to have a p_t as low as 50 MeV/c. The clear differences between the p_t and Θ distributions of the π^o Dalitz decay and the direct decay of the ρ into

[9)]The expected limits of the different quantities characterizing a ring mentioned in Section 5.2 have been obtained from a sample of rings belonging to tracks selected by eye scanning on the data. The same distributions were obtained from fake rings also selected by eye scanning.

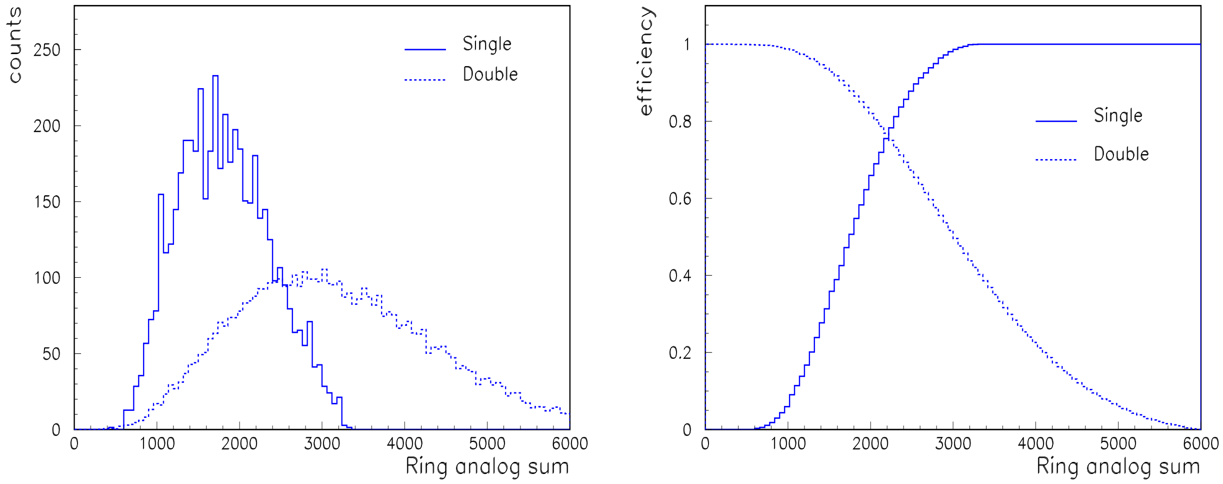

Figure 5.11: **Left:** Distribution of the analog sum for single and double rings. **Right:** Corresponding recognition and rejection efficiency curves based on the summed analog cut.

e^+e^- are shown in Figure 5.10. In the spirit of what we discussed in Section 3.2 when evaluating the benefits of a p_t cut on the S/B, only tracks with $p_t > 200$ MeV/c are paired to obtain the final signal. Among the remaining single tracks we still have a contamination from γ and π^o Dalitz pairs where one track has been lost by loosing one of the rings in RICH2 (see footnote on page 48). Several additional cuts can be exploited to identify such tracks. A double ring in RICH1 from a conversion has on average a double summed amplitude and a higher number of hits than a single one. The increased probability of hit pile-up in this case

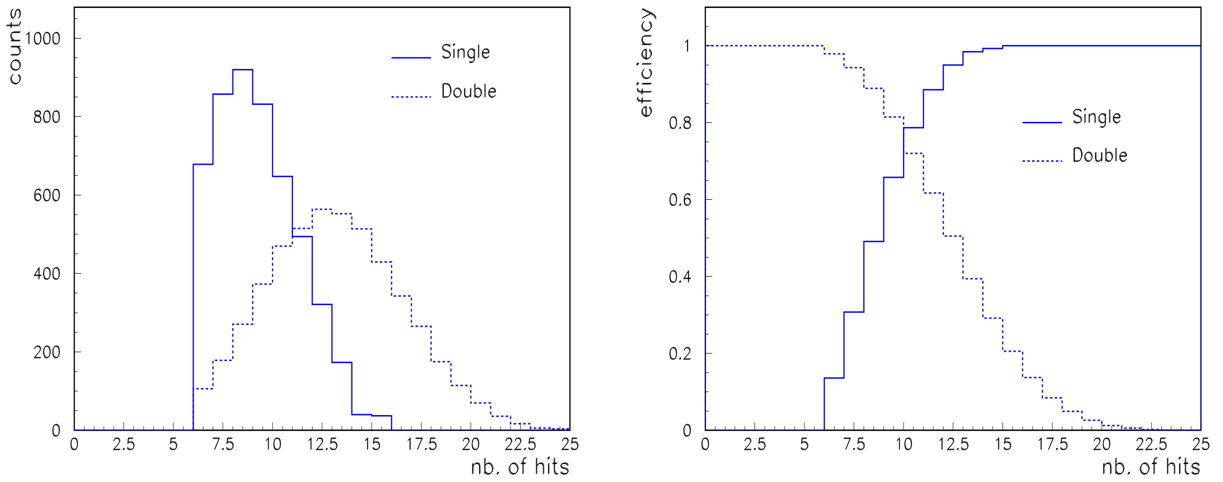

Figure 5.12: **Left:** Distribution of the number of hits for single and double rings **Right:** Corresponding recognition and rejection efficiency curve based on the number of hits cut.

makes that the number of hits will not double the average number of hits of a single ring. Nevertheless, cuts in these two quantities can be defined to reject single tracks with a double ring in the first RICH. Figures 5.11 and 5.12 show the double-ring rejection and single-ring acceptance efficiencies for both cuts.

An extremely useful rejection tool is provided by the SiDC information. A conversion is characterized by a double dE/dx hit in the SiDC, or by two resolved close hits with single dE/dx. Single tracks which are matched with such patterns in the SiDC are rejected as members of an unrecognized conversion. On the same grounds, tracks with a ring in RICH1 closer than 2 degrees are rejected as members of an unrecognized Dalitz decay if the ring has a single-dE/dx matched hit in the SiDC.

A final contribution to single tracks comes from high momentum pion tracks with rings' radii close to the asymptotic electron radius. A high momentum cut and a cut on the radius from the variable radius ring fit are used to eliminate these tracks.

The residual combinatorial background in the e^+e^- sample is determined by the number of like sign pairs (e^+e^+ and e^-e^-). The e^+e^- pair signal is finally obtained by subtracting the like-sign contribution from the e^+e^- sample as explained in the next chapter.

Chapter 6

Results

In this chapter I present the results obtained from the analysis of the data on S-Au collisions at 200 GeV/nucleon taken by CERES in April 1992. The experimental dielectron mass spectrum is compared to that from the known hadronic sources relevant to the CERES mass range (see Chapter 4). Also the question of a possible quadratic dependence of the dielectron yield on the event charged-particle multiplicity is addressed.

6.1 Dielectron signal.

The final sample of e^+e^- pairs obtained from both the FLT and SLT data sets, as well as the combined global one, is shown in Table 6.1. The signal S is defined as

$$S = N_{+-} - (N_{++} + N_{--}) \tag{6.1}$$

where N represents the number of pairs with sign as indicated by its subscript. The like-sign pair sample ($N_{++} + N_{--}$) represents our combinatorial background, and the last line of Table 6.1 shows the signal-to-background ratio as S/($N_{++} + N_{--}$). The errors quoted are only statistical. Figure 6.1 shows the comparison between the pair invariant mass distribution for the like-sign and unlike-sign samples.

There are some further considerations to be made in the way the signal is extracted. Our straightforward method of simply subtracting the like-sign background assumes that the spectrometer has the same acceptance for like–sign and unlike–sign pairs and that the underlying physical processes produce positive and negative tracks with the same probability. The only sources which could cause a charge asymmetry are δ-electrons produced by the beam as it traverses the target and charged secondaries as they traverse the spectrometer, and Compton electrons from the scattering of produced photons off the target atoms. Both contributions give rise to low energy electrons which will produce rings in RICH1 of non-asymptotic radius and blurred due to the strong effect of multiple scattering at such energies. The focusing action of the magnetic field deflects most of the tracks of this origin off the RICH2 acceptance. The combined effect of the requirements of the ring finding routine and the p_t cut applied at

		FLT	SLT	TOTAL
like sign:	++	782	636	
	– –	865	695	
	total (B)	1647	1331	2978
unlike sign		1865	1607	3472
Signal (S)		218 ± 59	276 ± 54	494 ± 80
S/B		0.14 ± 0.04	0.21 ± 0.04	0.17 ± 0.03

Table 6.1: Sample sizes in the FLT, SLT and total data sets.

the track level enssures the further rejection of such contributions to a negligible level [74]. The only effect of electrons from such sources is a contribution to the random hit background. As we have not detected any appreciable charge asymmetry within the CERES acceptance we can justify the use of equation (6.1).

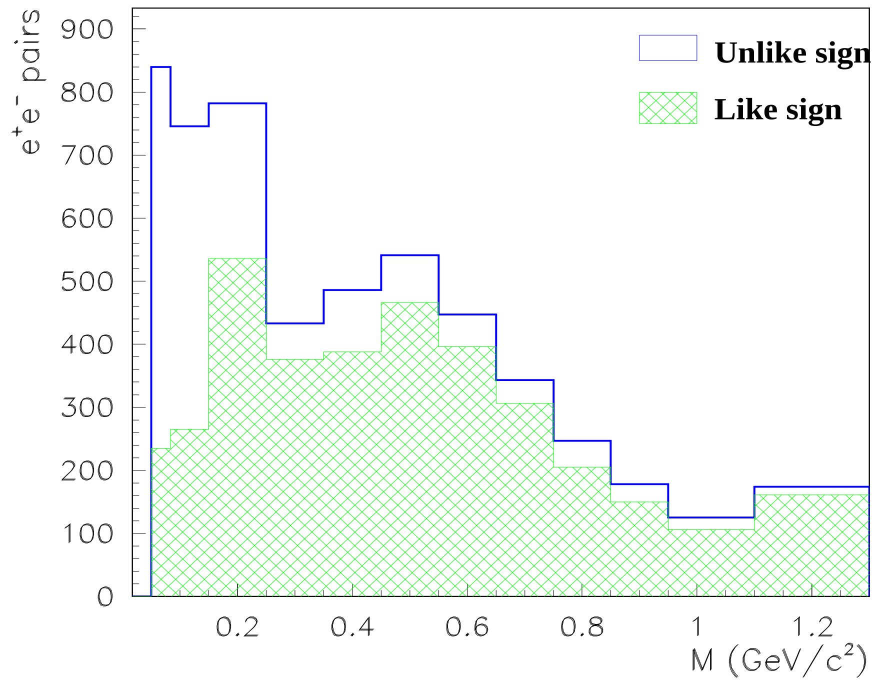

Figure 6.1: Like-sign and unlike-sign pair invariant mass distributions.

6.2 Normalization of the signal

For the overall normalization of the data we need to know precisely the effect of the SLT trigger on the collected data sample as well as the pair reconstruction efficiency. In this section we describe the methods used to obtained these quantities.

6.2.1 Trigger enrichment.

There are two effects at interplay in the enrichment of the trigger, namely the trigger rejection R and the trigger efficiency ϵ. These two quantities are defined as follows: Assuming that N events containing a signal S are fed into the trigger logic and N' events containing a signal S' are accepted by the trigger, the rejection R is defined as the inverse of the fraction of events the trigger rejects,

$$R = \frac{N}{N'} \tag{6.2}$$

and the trigger efficiency as the fraction of the signal present in the initial sample which is still present in the accepted sample.

$$\epsilon = \frac{S'}{S} \tag{6.3}$$

The trigger enrichment is defined as $E = R\,\epsilon$ and it can be viewed as the gain in signal–per–event in the final sample due to the introduction of the trigger,

$$E = R\,\epsilon = \frac{S'/N'}{S/N} \tag{6.4}$$

We have used two independent ways to obtain the trigger enrichment. The first one relies on a software emulator of the hardware trigger. The operations of the rough pattern recognition performed by the second level trigger are performed by off-line software on untriggered events. The full FLT sample, N_{FLT} events containing a signal S_{FLT}, have been passed through the emulator program, obtaining a reduced sample N'_{FLT} containing a signal S'_{FLT}. The trigger enrichment is then readily evaluated as in equation (6.4).

Actually there is another method of obtaining the rejection which does not make use of the software emulator. It takes advantage of the fact that for debbuging purposes we have collected a series of untriggered data tapes where the second level trigger decision on each event was kept as a label. Thus each event on this sample is flagged by an "accepted/rejected" label. This provides a powerful method to calculate in principle both the trigger rejection and efficiency. The accumulated data sample is nevertheless not large enough to calculate the efficiency. The rejection in this case is simply obtained by the ratio of the number of events labeled as "accepted" to the total number analyzed. We have thus calculated an average rejection from these two methods, which combined with the efficiency obtained from the emulator gives us the enrichment. The results are presented in Table 6.2. The errors quoted are only statistical.

	Rejection	Efficiency	Enrichment
From software emulator	4.5 ± 0.4	0.40 ± 0.11	
From FLT flagged data	4.0 ± 0.3	-	
Average	4.18 ± 0.24		1.67 ± 0.42
From data samples			1.60 ± 0.51
Global average			1.64 ± 0.32

Table 6.2: Trigger rejection, efficiency and enrichment factors obtained by the different methods mentioned in the text.

A second approach to obtain the enrichment factor uses the collected SLT data sample, avoiding the use of the software emulator. We can assume that the observed SLT signal, S_{SLT}, is obtained from an (unknown) number of untriggered–equivalent events N_{SLT}^{EQ}. The relation between the number of events processed and the signal obtained can be deduced from the FLT data. Thus N_{SLT}^{EQ} can be estimated as

$$N_{SLT}^{EQ} = N_{FLT}\,\frac{S_{SLT}}{S_{FLT}}$$

The trigger enrichment is obtained directly from the actual number of SLT events on tape, N_{SLT}, and the untriggered–equivalent events,

$$E = \frac{N_{SLT}^{EQ}}{N_{SLT}}$$

The average enrichment factor obtained from the two methods mentioned previously is 1.6±0.3 (see Table 6.2). We have used this mean value in the normalization of the data as explained in Section 6.1 below.

There is a third way of obtaining the trigger enrichment factor by making combined use of the Monte Carlo generator and the trigger emulator. We can overlay Monte Carlo generated tracks on untriggered events and pass such events through the emulator. Again, the trigger enrichment would be given directly by equation (6.4). This method introduces additional uncertainties through the use of the Monte Carlo in comparison with the other methods mentioned in the text, which make direct use of the data.

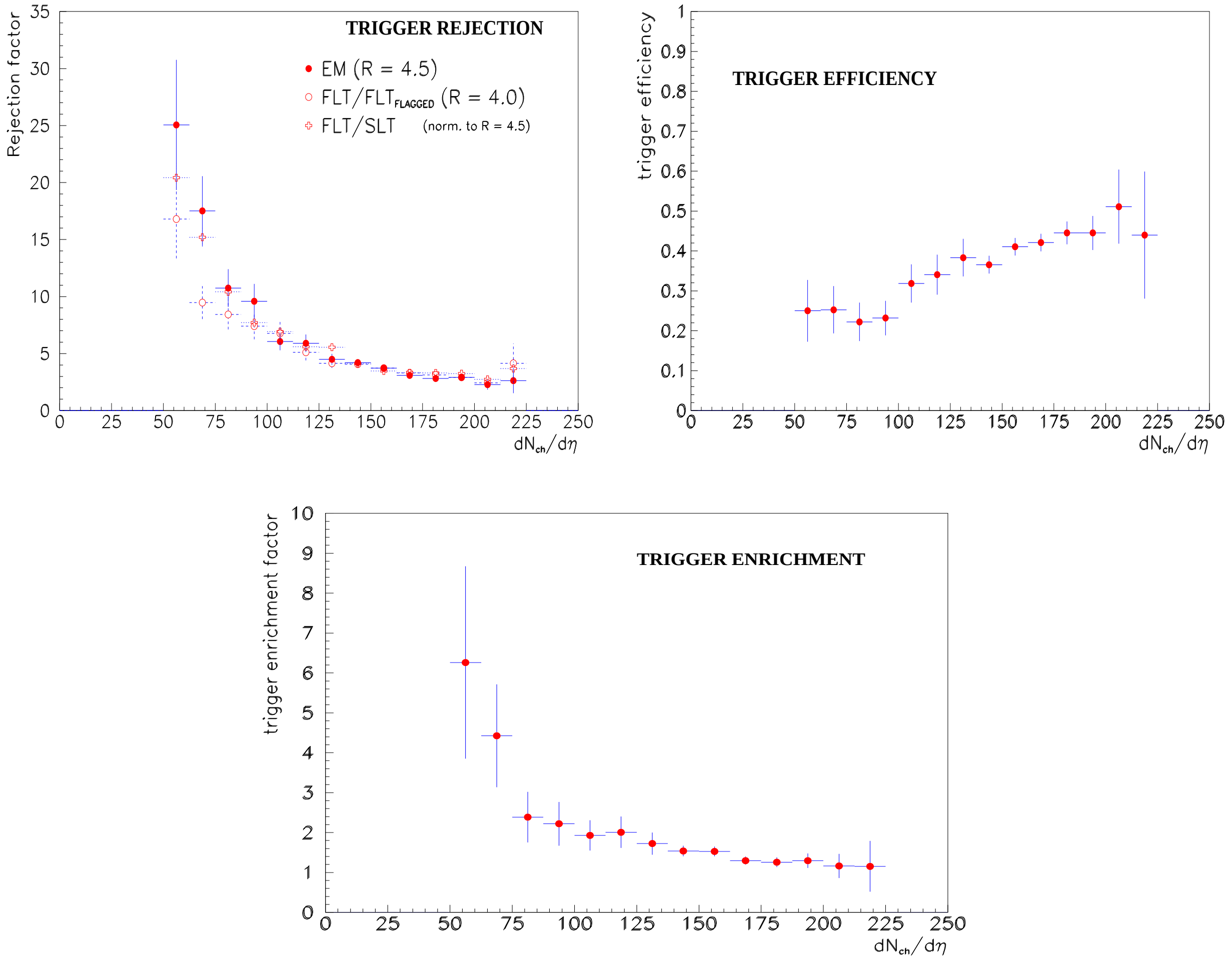

Figure 6.2: Trigger rejection, efficiency and enrichment as a function of the charged particle rapidity density. The three curves of the rejection factor shown correspond to the three methods of obtaining the rejection as explained in the text.

In Section 6.4 we will present our results on the charged multiplicity dependence of the dielectron yield as measured by CERES. For this study we need to assess the multiplicity dependence of the trigger enrichment factor through the dependence of the rejection and efficiency. We expect a strong multiplicity dependence in both quantities: high multiplicity events involve a high number of activated pads and the crude SLT pattern recognition is expected to deteriorate as the event multiplicity increases. On one side, with increasing number of active pads, more fake rings will be found and less events rejected. On the other hand the fake rings found can veto the signal through the 2-degree cut, making the efficiency dependent on the event multiplicity also. The combined effect results in an overall decreasing of the enrichment factor with event multiplicity.

The rejection factor as a function of the event multiplicity has been obtained using the two methods mentioned above–from the events taken by the software emulator, and from the events flagged by the hardware trigger on the debbuging set of tapes. A third method, the direct ratio of the experimentally measured multiplicity distributions from the FLT and SLT data samples, can give us the shape of the rejection curve. It does not provide an absolute normalization but, in order to compare it with the rejection curves obtained by the other two methods, we have normalized it to the average rejection value of 4.5 obtained from the emulator.

Similarly, we can obtain the multiplicity dependence of the trigger efficiency as the ratio of the multiplicity distributions of events with at least one signal pair before and after passing the FLT sample through the emulator.

The results on the dependence of the trigger rejection, efficiency and enrichment with the event charged multiplicity are shown in Figure 6.2. The rejection factor obtained with the emulator and by the flagged set of events are overlayed for comparison, along with the normalized curve from the FLT/SLT ratio.

6.2.2 Pair reconstruction efficiency.

Another crucial quantity to extract the final signal is the pair reconstruction efficiency, ε_{pair}, defined as the fraction of pairs found by the software analysis chain with respect to the total number of pairs within the spectrometer acceptance. ε_{pair} was obtained by generating the relevant decay processes as mentioned in Chapter 4 and simulating the corresponding rings in the RICHes with an independent Monte Carlo. This Monte Carlo takes into account the specific characteristics of the RICHes (the average number of hits per ring, $\langle N \rangle$, the hit amplitude distribution and the single hit resolution) to generate realistic electron tracks. The ring centers obtained from the physics generator are smeared according to the measured ring center resolution, which includes the multiple scattering suffered by the electrons in their passage through the spectrometer. A ring is generated at the new position with a number of hits obtained from a Poisson distribution with an average given by the measured $\langle N \rangle$ of the UV detectors. The hit coordinates are spread around the nominal ring radius according to the measured single hit resolution. The hit amplitude is generated according to the typical exponential distribution of single UV photons. The obtained amplitude is spread according to a two-dimensional Gaussian over a box of 5×5 pads to mimic the typical hit size. Hits falling under a spoke are removed to mimic the detector hit losses from this source.

The resulting rings are overlayed on untriggered events which are passed through the analysis programme, with the *same* cuts used in the real data analysis. ε_{pair} is thus given by the fraction of found Monte Carlo pairs with respect to the total generated ones.

The pair reconstruction efficiency is a function of both the event multiplicity and the pair invariant mass. For high multiplicities we expect ε_{pair} to decrease, as we increase the fake-ring probability and also the veto on single tracks due to a close ring. In the case of low masses

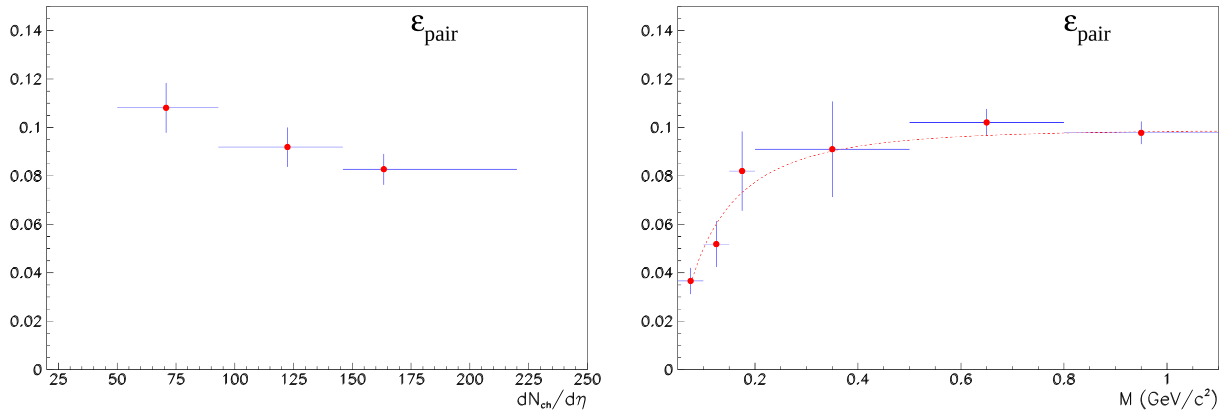

Figure 6.3: Pair reconstruction efficiency as a function of the event multiplicity for pairs with $m > 200$ MeV/c^2 (left) and as a function of the pair invariant mass (right). In both cases a $p_t > 0.2$ GeV/c^2 cut on each track and an opening angle cut of $\Theta > 35$ mrad. was applied.

two variables enter the game, the momentum and the pair opening angle. The reconstruction of low momentum tracks is limited by the multiple scattering up to the point where a ring can be deformed beyond recognition and lost, whereas the reconstruction of pairs with very small opening angles is limited by the double ring resolution. These effects result in the multiplicity and mass dependence of ε_{pair} as shown in Figure 6.3. The average value is $(9.2 \pm 1.0) \times 10^{-2}$.

6.3 Differential e^+e^- invariant mass spectrum.

We have chosen to present the differential invariant mass spectrum as pair density per charged particle rapidity density. The basic assumption underlying such normalization is that, in the absence of new physics, nucleus–nucleus collisions are a superposition of nucleon–nucleon collisions. This implies that the ratios of particle production cross sections remain constant when going from p-p collisions to nucleus–nucleus collisions and that therefore e^+e^- pair production scales with the event multiplicity,

$$\left(\frac{d\sigma_i/dy}{d\sigma_{\pi^o}/dy}\right)_{p+p} = \left(\frac{d\sigma_i/dy}{d\sigma_{\pi^o}/dy}\right)_{p+A} = \left(\frac{d\sigma_i/dy}{d\sigma_{\pi^o}/dy}\right)_{A+A} \tag{6.5}$$

This assumption allows us to normalize in a consistent way our data and the expected yield from the hadronic sources included in the generator described in Chapter 4. The normalization of the data is therefore done in the following way

$$\frac{d^2N_{e^+e^-}/dmd\eta}{dN_{ch}/d\eta} = \frac{dS/dm}{N_{ev} \cdot \varepsilon \cdot \langle \frac{dN_{ch}}{d\eta} \rangle \cdot \Delta\eta} \tag{6.6}$$

where ε is the pair reconstruction efficiency, $\langle dN_{ch}/d\eta \rangle$ the average charged particle multiplicity determined from the FLT trigger data, $\Delta\eta$ the spectrometer pseudo-rapidity coverage

E	1.6 ± 0.3
N_{FLT}	3.041×10^6
N_{SLT}	2.143×10^6
ε	$(9.2 \pm 1.0) \times 10^{-2}$
$\langle \frac{dN_{ch}}{d\eta} \rangle$	125
$\Delta\eta$	0.55

Table 6.3: Values of the quantities used in the normalization of the data. The pair reconstruction efficiency ε is a function of mass (see Figure 6.3) and only the average value is quoted. E is the average trigger enrichment factor as determined in Section 5.2.2

and N_{ev} the number of events processed. This latter quantity combines both the FLT sample and SLT sample as $N_{ev} = N_{FLT} + E\,N_{SLT}$, where E is the SLT enrichment factor. The values used in the normalization are quoted in Table 6.3. The final dielectron mass spectrum measured by CERES in S-Au collisions is shown in Figure 6.4. Note that the data has been corrected for the pair reconstruction efficiency but not for the pair acceptance. The vertical bars on each bin show the statistical error only, while the brackets correspond to the quadratic sum of the statistical and systematical errors. The main contributions to the systematical errors come from the errors on the pair reconstruction efficiency ϵ and the enrichment factor E. The data are compared to the expected yield from the hadronic sources included in the generator (see Section 4.3 and Table 3.5). The shaded area in the plot represents the theoretical uncertainty in the scaled p-p yield, resulting from the experimental uncertainties in the branching ratios, form factors and cross sections used in its evaluation.

Figure 6.4 reveals a statistical significant excess of electron pairs over the hadronic sources in the mass range $0.2 < m < 1.5$ GeV/c^2. A quantitative measure, Δ, of such an enhancement can be defined as

$$\frac{\text{integral of the measured data}}{\text{integral of the expected yield from hadronic sources}} \tag{6.7}$$

The enhancement obtained from the data is $\Delta = 4.7 \pm 0.8_{stat} \pm 2.2_{sys}$. This result should be compared to the results obtained by CERES on p-Be (shown in figure 4.3) and p-Au [127], where the measured e^+e^- yield is reproduced by the generator sources. The shape of the experimental invariant mass spectrum is also revealing. The enhancement sets in for masses $m > \sim 0.2$ GeV/c^2 which is close to twice the pion mass. This could be an indication that we are observing $\pi^+\pi^-$ annihilation from a hot fireball. As mentioned when discussing the VMD model, this process proceeds through a virtual ρ, which would further explain the extension of the enhancement up to the ρ mass region. This would be the first observation of thermal radiation from a hot and dense hadron gas. I will discuss possible interpretations of these results in the next chapter.

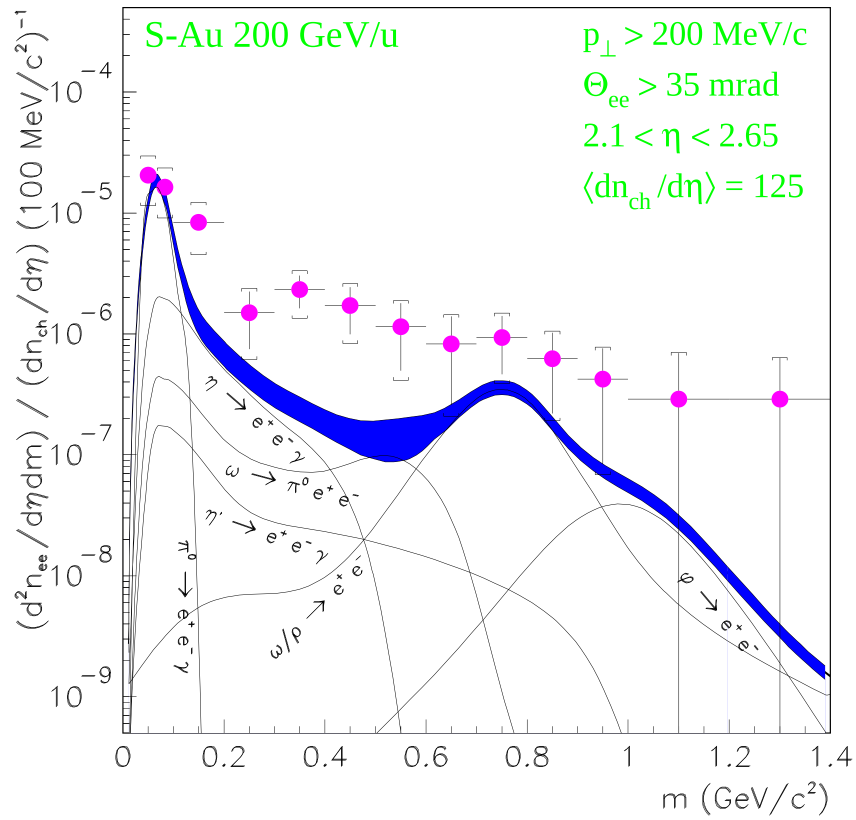

Figure 6.4: Dielectron invariant mass spectrum obtained from the S-Au data by CERES.

6.4 Multiplicity dependence of the dielectron yield.

The dependence of the dielectron yield on the event charged-particle multiplicity N_{ch} can be a useful tool to identify the type of emitting process. As described in Chapter 2, one can distinguish three stages in a nuclear collision. First, particles are produced by direct parton-parton scattering, then a radiating hot and dense fireball is formed, and, finally, resonances and final state hadrons decay into stable particles. The dependence of the dielectron yield on the charged-particle multiplicity in these three stages is quite different [125].

Dielectron production from a hot dense fireball proceeds through $q\bar{q}$ or $\pi^+\pi^-$ annihilation and thus it should be proportional to N_{ch}^2 (assuming that the quark content of a possible QGP is proportional to the final hadron multiplicity). On the other hand, the dielectron yield from hadron decays is proportional to the N_{ch} produced in the interaction[1)].

[1)]Dilepton production from Drell-Yan is expected to be independent of multiplicity, but in any case it is not relevant in the CERES mass range.

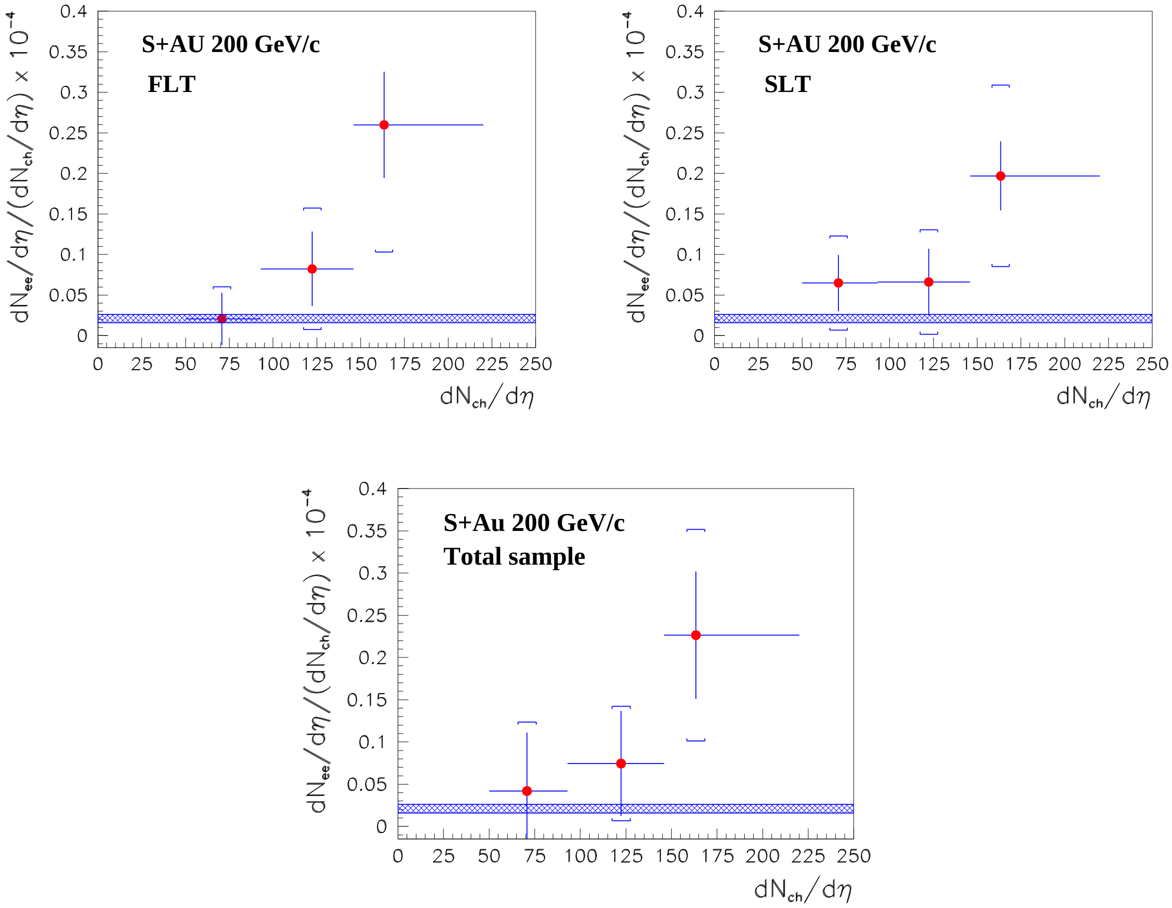

Figure 6.5: Dependence of the e^+e^- yield on the event charged particle multiplicity for both the FLT and SLT data samples. The lowest plot shows the combined FLT+SLT results. We have used the average trigger enrichment from the three possible methods discussed in the text.

We can not follow the time evolution of the interaction in a way as to detect these dependences independently. The dielectron yield observed is the superposition of the different processes mentioned, and we should expect a differential yield $dNe^+e^-/d\eta$ composed of two contributions which we can write as

$$\frac{dN_{e^+e^-}}{d\eta} = a_1 \frac{dN_{ch}}{d\eta} + a_2 \left(\frac{dN_{ch}}{d\eta}\right)^2 \tag{6.8}$$

which when plotted *per charged particle rapidity density* would give a linear dependence

$$\frac{dN_{e^+e^-}/d\eta}{dN_{ch}/d\eta} = a_1 + a_2 \frac{dN_{ch}}{d\eta} \tag{6.9}$$

Figure 6.5 shows the multiplicity dependence of the dielectron yield measured by CERES for the FLT, SLT and total data samples. The low statistics available does not allow to divide the multiplicity axis in more than three bins, which have been chosen, somehow arbitrarily, as to contain the same fraction of events. The data shown in Figure 6.5 are normalized to show pair rapidity density per charged particle rapidity density,

$$\frac{dN_{e^+e^-}/d\eta}{dN_{ch}/d\eta} = \frac{S_{bin}}{N_{bin} \cdot \varepsilon_{bin} \cdot \langle \frac{dN_{ch}}{d\eta} \rangle_{bin} \cdot \Delta\eta} \tag{6.10}$$

where the quantities are defined as in equation (6.6), but now they refer to the respective multiplicity bin. The error bars represent the statistical error and the small brackets correspond to the statistical and systematical errors added quadratically. The experimental points are located at the center of gravity of the corresponding bin. The shaded horizontal line represents the yield from the standard hadronic sources which, being a scaled p-p yield, is independent of multiplicity.

To extract some quantitative information on whether our data supports a thermal dielectron yield scenario, we have performed an statistical χ^2 hypothesis testing on the two following cases:

a) A straight line fit to equation (6.9) (two free parameters, a_1 and a_2) to test the hypothesis of a quadratic (thermal) dependence. The fitted values of the parameters are $a_1 = (-0.891 \pm 0.172) \times 10^{-4}$ and $a_2 = (0.158 \pm 0.150) \times 10^{-6}$. We obtain a χ^2 of 0.46 for one degree of freedom (3 bins minus two fit parameters). The large errors associated with the data give room to fit a variety of curve shapes or straight lines with different slopes. This results in a very low confidence level (*c.l.*) for the quadratic dependence hypothesis, *c.l.* = 48%.

b) A test to the hypothesis that the observed points come from the expected yield from the conventional hadronic sources included in the generator (shown as the grey band in Figure 6.5). Since in this case the "theoretical" prediction has an associated error the variable χ^2 is defined as

$$\chi^2 = \sum_i \frac{(y_i - y_{th})^2}{\sigma_i^2 + \sigma_{th}^2} \tag{6.11}$$

where the subscript *th* stands for the conventional hadronic scenario prediction, $y_{th} = \text{constant} = 2.08^{+0.35}_{-0.42} \times 10^{-6}$. In this case the large errors on the data points and on the theoretical prediction allow for a sizeable probability that the data could originate from the flat generator distribution. We obtain a χ^2 of 3.4 for 3 degrees of freedom (no free fit parameter). From this result we conclude that the conventional hadronic scenario could reproduce our results with a probability of 35%.

From the figures just obtained, we see that our present results are not restrictive enough to unambiguously extract any conclusion on the multiplicity dependence of the e^+e^- yield.

The statistical tests performed on the data do not allow us to reject the linear scenario, which would be a claim of non standard dielectron production mechanisms in our data.

Note that equation (6.8)– and therefore our statistical tests– implicitly assume a unique scenario for the multiplicity dependence of the signal along the whole range of the multiplicity axis. A more specific scenario would take into account different production mechanisms in different ranges of multiplicity: a linear dependence, which would stem just from decays of reaction products, for all multiplicities and the set in of a quadratic dependence for high multiplicity events, around $dN/d\eta \sim 100$ as suggested by Figure 6.5. The confirmation of such scenario would require increased statistics over the whole multiplicity range to be able to increase the data points by means of a finer binning. Such a measurement would be of extreme interest for addressing the type of mechanisms at play in nuclear collisions. We believe that the data taken by CERES in November 1995 with a ^{208}Pb beam will be determinant to address these issues.

Chapter 7

Discussion

It is interesting to view the results from CERES on low mass dielectron production along with the results of the other two dilepton experiments at CERN, HELIOS-3 and NA38, on low and intermediate mass dimuon production. In this chapter I compare the results of these three experiments, summarizing the current status of dilepton production in heavy ion collisions at the SPS. I will also discuss recent theoretical approaches which have been proposed in order to explain the observed experimental data.

7.1 Comparison with other experiments.

An excess of muon pairs has been reported by the HELIOS/3 collaboration [126] on S–W collisions at 200 GeV/c^2 with respect to the proton induced reactions. HELIOS covers a much wider mass range than CERES, up to masses $m_{\mu\mu} \sim 4$ GeV/c^2 and therefore it is also sensitive to the behaviour of the dimuon yield in the intermediate mass region. HELIOS results are shown in the left plot of Figure 7.1, where the S–W dimuon yield is compared to the p–W one. The data are normalized to the charged-particle multiplicity measured in the acceptance of the spectrometer. The dimuon enhancement covers a very wide mass range, from the low mass region below the ρ/ω peak, up to dimuon invariant masses of $m_{\mu\mu} \sim 2.5$ GeV/c^2. To be able to compare with the CERES result, we can calculate the HELIOS dimuon enhancement factor in the mass range common to both experiments, $0.2 < m < 1.5$ GeV/c^2, as the ratio of the integral of the measured data on S-W to the measured data on p-W.[1)] The value is ~ 1.6, smaller than the value found by CERES in the same mass range. This discrepancy could be a consequence of the different rapidity coverage of the two experiments. HELIOS covers the forward rapidity region, $3.7 < \eta < 5.5$, whereas CERES sits at mid-rapidity, $2.1 < \eta < 2.6$. Both experiments have therefore access to very different charged particle rapidity densities and, if the dilepton production mechanism scales non-linearly with the event multiplicity (see Section 6.4), such a discrepancy could be accounted for. Note that Figure 7.1 also shows the

[1)]Results from CERES on p+Au collisions at 400 GeV/c show that the dielectron yield in the p-nucleus case is well reproduced by the p-p yield [127]. We can then assume that the results from HELIOS-3 on p+W represent the p-p data with some degree of confidence.

J/ψ suppression as seen by this experiment and confirming the results of NA38.

NA38 has also reported a dimuon excess of 1.4 ± 0.1 [91] in the intermediate invariant mass range, $1.5 < m < 2.5$ GeV/c^2. Their result is shown in the left figure of 7.1 where the results for S-U are overlayed to those from p-W data. The spectra have been normalized in the high mass region ($m > 4.2$ GeV/c^2 where data are well reproduced by the Drell-Yan background. The rapidity window of NA38 is $3 < \eta < 4$ and therefore its results can be directly compared with HELIOS provided one chooses the appropriate mass range. The excess of dimuons found by HELIOS in the mass range covered by NA38 is 2.4 ± 0.4. Given that the NA38 data has not been corrected by the pair acceptance and that neither experiment quotes systematic errors, the discrepancy is not severe.

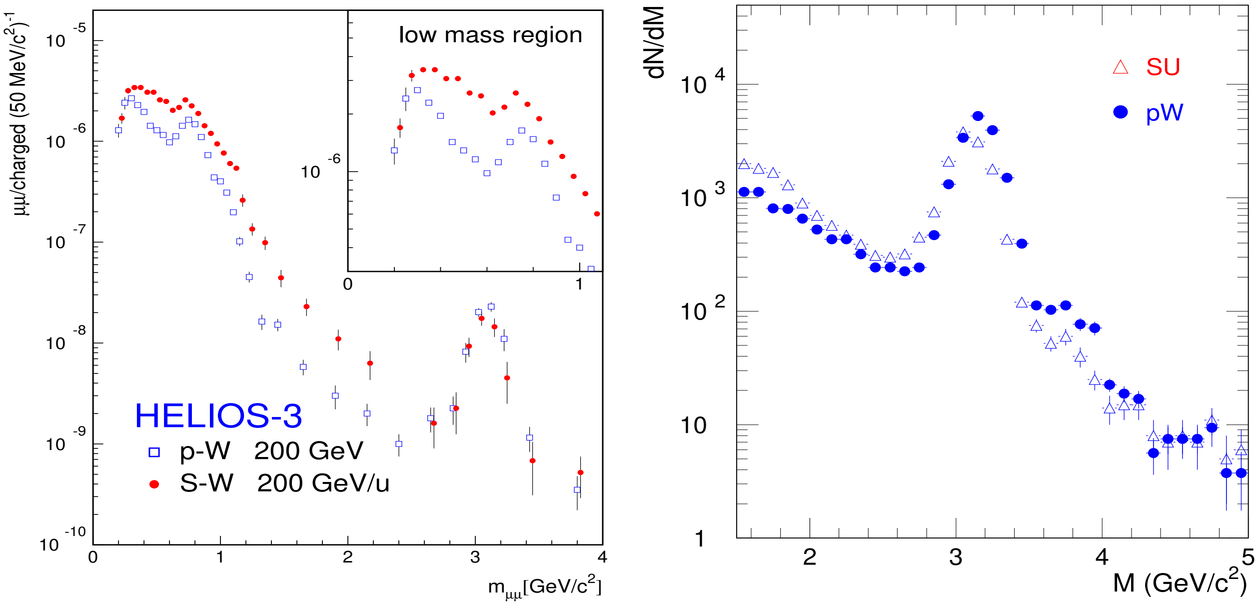

Figure 7.1: Results from HELIOS (left) and NA38 (right) collaborations on dimuon production in both p-nucleus and nucleus-nucleus collisions.

In summary, the three CERN dilepton experiments have observed an enhanced yield of dielectrons and dimuons over a wide range of invariant masses with a reasonable degree of consistency considering the different rapidity coverages. The still open experimental question is that of the multiplicity dependence of the observed dilepton excess, for which none of the mentioned experiments have conclusive data.

7.2 Comparison with theoretical models.

The measured enhancement of the low mass dilepton yield has triggered an intense theoretical activity to try to understand its origins. The attention focuses mainly on the dielectron data from CERES since it was measured at mid-rapidity and it is therefore directly comparable with calculations using standard transport models. But viewed in a comprehensive frame along with the results from HELIOS-3 and NA38, any phenomenological model describing a collision between two nuclei at SPS energies has to reproduce the observed dilepton enhancement over a wide dilepton invariant mass range, $0.2 < m_{l^+l^-} < 2$ GeV/c^2. It has to reproduce as well the wealth of data on particle multiplicities and rapidity and p_t distributions obtained by several experiments in the last decade. This provides a basics to be confident that the dynamics included in the model reflect in a reliable way the dynamics of the real collision. I describe below three of the recently proposed models which try to reproduce the data from CERES as an example of current efforts in these lines.

The model proposed by G. Li *et al.* [129] assumes that, initially, a hot and dense hadronic fireball is formed in the collision of two nuclei. In the case of an S-Au interaction at 200 MeV/c the initial temperature is taken to be 185 MeV and the initial baryonic density between 3 and $4\rho_o$. These values are chosen as to reproduce the measured proton and pion rapidity and p_t distributions after the complete evolution of the system. The initial chemical composition of the fireball includes the π, η, η', ρ, ω, a_1 and K and $\bar{K}$ and all the baryon resonances below 1720 MeV/c^2, as well as the Λ and Σ hyperons. The fireball is evolved according to the usual relativistic Vlasov-Uehling-Uhlenbeck (VUU) transport model [132, 133] down to a decoupling temperature of 120 MeV, from which interactions among produced particles are frozen. Dileptons are produced from the decays of the ρ and ω mesons and from $\pi^+\pi^-$ annihilation through the VMD model. In a more recent calculation [130] the authors have extended the model to include the description of the collision by the relativistic quantum molecular dynamics (RQMD) model [131]. This model is based on the formation and fragmentation of strings in the individual nucleon-nucleon collisions and hence there is no need to assume thermalization. The products of the primary interactions are evolved as in the previous calculation, through the VUU model, and hadrons are allowed to interact with each other and the resonances to decay into ground state hadrons.

A similar approach has been proposed by Cassing *et al* [134]. They use the Hadron String Dynamics (HSD) [135] to describe the space-time evolution of the collision. This is a microscopic transport model where the collision is described from the individual incoming parton-parton collisions, and there is no need to assume thermalization. The nucleons' effective mass and self-energy within the nuclei are extracted from their quark degrees of freedom using a low-energy effective Lagrangian. Particle production is assumed to proceed through binary nucleon-nucleon collisions in a similar fashion as in the LUND string fragmentation model. Produced nucleons, Δ's, N*(1440)'s, N*(1535)'s, Λ's, Σ's, π's, η's, ρ's, ω's, ϕ's, K's and K*'s are considered, along with their interactions. Dilepton production is calculated from the contributions of pn, nn, $\pi\pi$ bremsstrahlung, the Dalitz decays of the Δ, N*(1440), η and ω and the direct decays of the vector mesons as well as $\pi^+\pi^-$ annihilation.

A somewhat more unconventional approach is that taken by D. Srivastava *et. al.* [136]. In this model it is assumed that QGP is initially formed in the collision at a proper time τ_i at

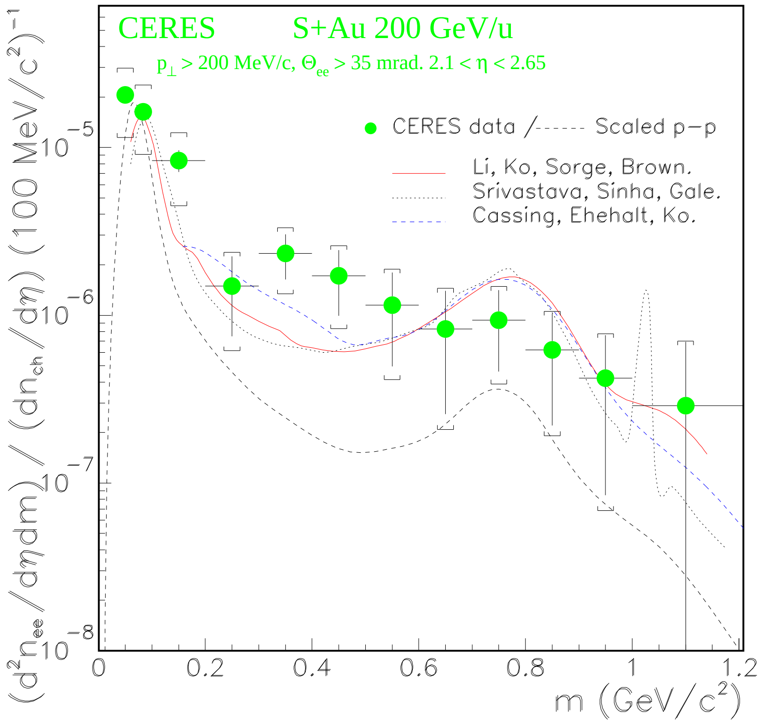

Figure 7.2: Comparison of the predictions of the models of Li *et al*, Cassing *et al* and Srivastava *et al* with CERES data. See the text for further details and references.

a temperature T_i. Assuming adiabatic expansion throughout the process, the initial temperature can be related to the measured particle multiplicity density dN/dy and the initial time [137]. Thus, assuming $\tau_i = 1$ fm and using the charged particle density measured by CERES, $dN_{ch}/dy = 125$, the authors arrive at an initial temperature of $T_i = 199$ MeV. The system expands and cools through hydrodynamical longitudinal expansion (transverse expansion is *not* included in this model), reaching a mixed phase at a transition temperature $T_c = 160$ MeV. Further expansion brings the hadron gas to a freeze-out temperature $T_f = 140$ MeV where the hadrons decouple. Dilepton emission from the QGP phase proceeds through $q\bar{q}$ annihilation, whereas in the hadronic system dilepton production comes from meson annihilation and the decays of the resonances as proposed in [138].[2] The relatively low initial temperature results in a very short lived QGP and makes that the main contribution to dilepton production comes from the mixed and hadronic phases.

[2]In particular the decays $\rho \to \pi e^+e^-$, $\rho \to \eta e^+e^-$, $K^{*\pm} \to K^{*\pm}e^+e^-$, $K^o \to K^o e^+e^-$, $\omega \to \pi^o e^+e^-$, $\eta' \to \rho e^+e^-$, $\eta' \to \omega e^+e^-$, $\phi \to \eta e^+e^-$, $\phi \to \eta' e^+e^-$, $\phi \to \pi^o e^+e^-$ and the **V**ector+**P**seudoscalar type interactions $\omega + \pi^o$, $\rho + \pi$, $\phi + \pi^o$, $\omega + \eta$, $\omega + \eta'$, $\phi + \eta$, $\phi + \eta'$, $\rho + \eta$, $\rho + \eta'$, $\bar{K}^* + K$ and $K^* + \bar{K}$ have been included, along with the V + V and P + P type, leading to a dilepton in the final state

The results of these three models are compared with the CERES data in Figure 7.2[3]. The three models reproduce well the CERES enhancement around the ρ region, mainly due to the inclusion of the $\pi^+\pi^-$ annihilation channel in their calculations. But also the three approaches fall short in reproducing the data at lower masses, $0.2 < m_{e^+e^-} < 0.4$ GeV/c^2.

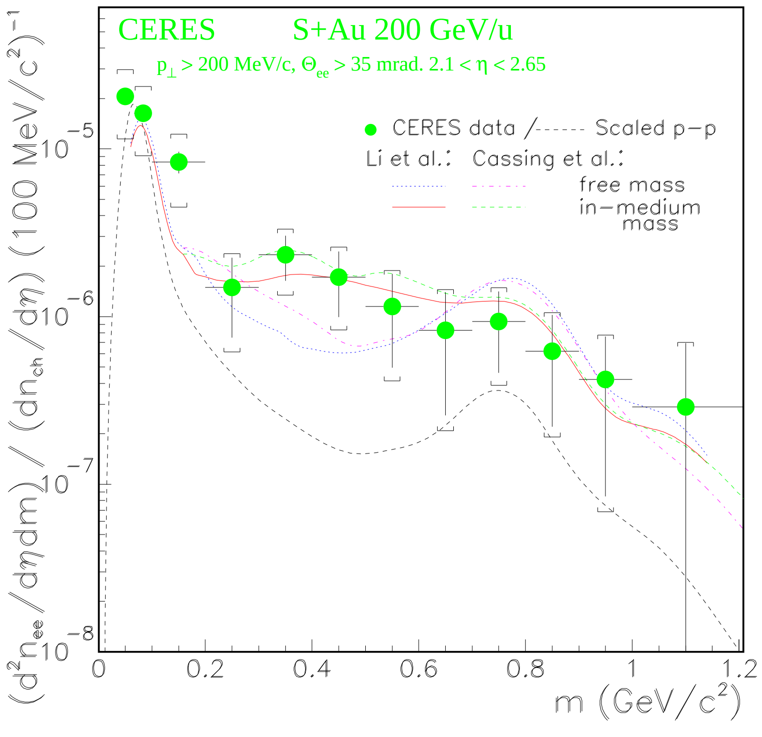

Figure 7.3: Comparison of the prediction of the models from Li *et al* and Cassing *et al* with CERES data when the in-medium modification of the ρ mass is included. See the text for further details and references.

Since the production of low mass dileptons in the fireball is dominated by $\pi^+\pi^-$ annihilation through an intermediate ρ, any in-medium modification of the ρ mass is expected to affect dramatically the shape and total yield of the dilepton spectrum [109]. In this spirit, the groups of Li *et al.* and Cassing *et al.* have included the modification of the vector and axial-vector meson masses due to partial restoration of chiral symmetry in the dense fireball formed in the nuclear interaction. In the model of Li *et al.* the ρ and ω masses are modified with respect to their vacuum value by coupling to the scalar field included in the effective Lagrangian used to describe the dense many-body nuclear system, in a similar way as it is done in describing the effects of the finite nuclear density on the nucleon inside a nucleus

[3]Note that the Srivastava *et al.* have not convoluted their prediction with the CERES mass resolution and therefore the ϕ peak appears as the bare resonance.

[101]. This allows to include the dense-medium effects on the masses in a straightforward way in the model used to describe the dynamical evolution of the fireball. In this approach the in-medium ρ mass, m^*_ρ, is parameterized as $m^*_\rho = m_\rho - g_s\langle S\rangle$. The scalar field is determined self-consistently from the energy density of the fireball. The agreement with the CERES data in this case is remarkable. Similar calculations have been carried out by Cassing *et al.* [134, 139], but including the dense-medium effects as predicted by QCD sum rules [108] where $m^*_\rho/m^o_\rho = 1 - 0.18(\rho^*/\rho^o)$. They also find an excellent agreement with CERES data and reproduce HELOS-3 data on dimuons.

These are very recent results and should be taken with caution. Note that the large error bars on the data and the lack of an error estimation on the theoretical curves do not completely rule out the standard scenarios of Figure 7.2. We have just opened an exciting topic where improved theoretical calculations and better data from the dilepton experiments are expected soon.

Appendix

Basic Čerenkov radiation formulae

Čerenkov radiation is essentially an electromagnetic shock wave phenomenon, similar to the acustic one. A charged particle traversing a distance ΔL in a dielectric transparent medium induces local rearrangements of the atoms lying along its trajectory, thus creating temporary dipoles. After the passage of the particle the atoms return to their initial state. The net effect is that the element ΔL first absorbs and then re-emits a short electromagnetic impulse. In general the spheric electromagnetic waves emitted by the element ΔL will interfere destructively giving rise to no net electromagnetic field over macroscopic distances. The case is not the same when the velocity of the particle is greater than the speed of light in the medium. In this case we have constructive interference of the emitted waves, giving rise to a net electromagnetic emission which can be observed at macroscopic distances from the original trajectory of the passing particle.

In the latter case the radiation is emitted at an angle θ with respect to the particle's trajectory given by

$$cos(\theta) = \frac{1}{n\,\beta}$$

where n is the refractive index of the medium and $\beta = v/c$. For a given medium, and to keep $cos(\theta) \leq 1$ there is a threshold β, $\beta_{thr} = 1/n$, under which the particle will not emit Čerenkov radiation[4]. We note that β_{thr} depends only on the characteristics of the medium through n, and not on the mass or the charge of the particle.

From the equations of motion for relativistic particles we can easily calculate the threshold momentum for a particle of mass m to emit Cerenkov radiation when traversing a medium of refractive index n,

$$p_{thr} = m\gamma_{thr}\beta_{thr} = \frac{m}{\sqrt{n^2 - 1}}$$

In the case of ultrarelativistic particles with $\beta \sim 1$

$$cos(\theta) = \frac{1}{n} = \frac{\sqrt{\gamma_{thr}^2 - 1}}{\gamma_{thr}^2}$$

and

$$sin(\theta) \sim \theta \sim \frac{1}{\gamma_{thr}}$$

[4]Usually the threshold Lorenz factor $\gamma_{thr} = n/\sqrt{n^2-1}$ is quoted for a given substance.

$n_{CH_4} \,=\, 1.000576$ $\gamma_{thr}(measured) \,=\, 31.6$ RICH1 $f_{RICH1} \,=\, 126$ cm $R_e \,=\, 4.3$ cm

	m (GeV)	p$_{thr}$ (GeV)	R$_{thr}/R_e$	p$(_{R=0.95R_e})$ (GeV)
$\pi^{\pm}$	0.139	4.1	0.05	12.7
$\mu^{\pm}$	0.106	3.1	0.22	9.8

Table 7.1: Threshold momenta, p_{thr}, ring radius at p_{thr} and momenta for a radius equal to the asymptotic electron radius for pions and muons in RICH1.

Given the CERES geometry, the radius of the Čerenkov ring produced by particles traversing the RICH radiators is given by

$$R \,=\, f\,tan(\theta)$$

where f is the focal length of the mirror. In the case of electrons we are in the asymptotic regime ($\beta \sim 1$) and therefore we have $tan(\theta) \sim \theta$ and

$$R_{asymp} \,=\, f\,\theta$$

In general, $\beta \,=\, p/E \,=\, p/\sqrt{p^2 + m^2}$ and thus

$$cos(\theta) \,=\, \frac{1}{n}\sqrt{1 \,+\, \frac{m^2}{p^2}}$$

Then the momentum of the particle and the radius of the produced ring are related by

$$R(p) \,=\, f\,tan\Big(\sqrt{\frac{n^2}{1 + m^2/p^2} \,-\, 1}\Big)$$

$$p(R) \,=\, \frac{m}{\sqrt{\frac{n^2}{1+atan^2(R/f)} \,-\, 1}}$$

where R is given in cm and p in GeV.

Table 7.1 summarizes the relevant quantities for the specific CERES setup. We show the threshold momentum for pions and muons, the relative size of their rings at the threshold momentum and the momentum at which they produce a ring with 95% the electron asymptotic radius. Figure 7.4 shows the radius of the Čerenkov ring as a function of the particle's momentum for both pions and muons respect to the asymptotic electron radius.

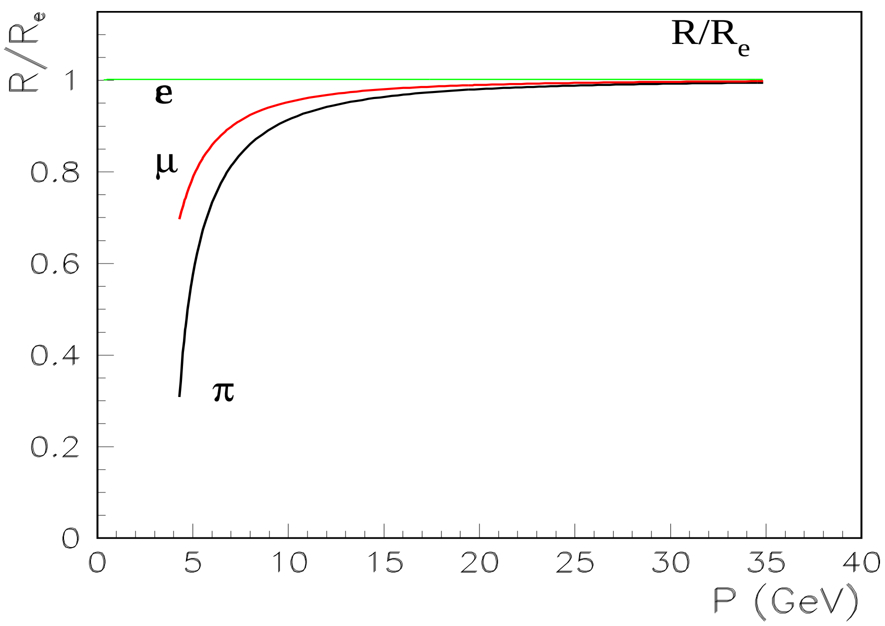

Figure 7.4: Momentum dependence of the Čerenkov ring radius for pions and muons with respect to the asymptotic electron one in RICH1.

Bibliography

[1] A. M. Polyakov. *Thermal properties of gauge fields and quark liberation.* Phys. Lett. **72B**, 477–480, 1978.

[2] R. D. Pisarski. *Phenomenology of the chiral phase transition.* Phys. Lett. **110B**, 155–158, 1982.

[3] H. Reeves. *Big-Bang nucleosynthesis and the quark-hadron phase transition.* Phys. Rep. **201** (6), 335–354, 1991.

[4] E. V. Shuryak. *Quantum Chromodynamics and the theory of superdense matter.* Phys. Rep. **61**, 71, 1980.

[5] K. Geiger. *Space-time description of ultrarelativistic nuclear collisions in the QCD parton picture.* Phys. Rep. **258**, 237–376, 1995.

[6] J. B. Kogut *An introduction to lattice gauge theory and spin systems.* Rev. Mod. Phys. **51**, 659, 1979.
M. Creutz *Quarks, Gluons and Lattices.* Cambridge Univ. Press 1983.

[7] L. J. Reinders, H. Rubinstein and S. Yazaki. *Hadron properties from QCD sum rules.* Phys. Rep. **127**, 1, 1985.

[8] E. G. Drukarev and E. M. Levin. *Nuclear matter and QCD sum rules.* Progr. Part. Nucl. Phys. **27**, 77, 1991.

[9] Y. Nambu and G. Jona-Lasinio. *Dynamical Model of Elementary Particles Based on an Analogy with Superconductivity.* Phys. Rev. **122 & 124**, 345 & 246, 1961.

[10] U. Vogl and W. Weise. *The Nambu Jona-Lasinio model: Its implications for hadrons and nuclei.* Progr. Part. Nucl. Phys. **27**, 195, 1991.

[11] M. Jacob and H. Satz (eds.) *Proc. of the Bielefeld Workshop on quark matter formation and heavy ion collisions.* World Scientific, Singapore 1983.
T. Lundlam and H. E. Wegner (eds.) *Proc. 3rd Int. Conf. on Ultra-Relativistic Nucleus-Nucleus collisions.* Brookhaven, USA, 1983. Nucl. Phys. **A418**, 1984.
K. Kajantie (ed.) *Proc. 4th Int. Conf. on Ultra-Relativistic Nucleus-Nucleus collisions.* Helsinki, 1984. *Lecture Notes in Physics* **22**, Springer Verlag, 1985.
S. Schroeder and M. Gyulassy (eds.) *Proc. 5th Int. Conf. on Ultra-Relativistic Nucleus-Nucleus collisions.* Asilomar, 1986. Nucl. Phys. **A461**, 1987.

H. Satz, H. J. Specht and R. Stock (eds.) *Proc. 6th Int. Conf. on Ultra-Relativistic Nucleus-Nucleus collisions.* Nordkirchen, 1987. Z. Phys. **C38**, 1988.
G. Baym, P. Braun-Munzinger and S. Nagamiya (eds.) *Proc. 7th Int. Conf. on Ultra-Relativistic Nucleus-Nucleus collisions.*Lennox, USA, 1988. Nucl. Phys. **A498**, 1989.
J. P. Blaizot et al. (eds.) *Proc. 8th Int. Conf. on Ultra-Relativistic Nucleus-Nucleus collisions.* Menton, 1990. Nucl. Phys. **A525**, 1991.
T. C. Awes et al. (eds.) *Proc. 9th Int. Conf. on Ultra-Relativistic Nucleus-Nucleus collisions.* Gatlingburg, 1991. *North Holland*, 1992.
E. Stenlund et al. (eds.) *Proc. 10th Int. Conf. on Ultra-Relativistic Nucleus-Nucleus collisions.* Borlange, Sweden, 1993. Nucl. Phys. **A566**, 1994.
A. M. Poskanzer et al. (eds.) *Proc. 11th Int. Conf. on Ultra-Relativistic Nucleus-Nucleus collisions.* Monterey, USA, 1995. Nucl. Phys. **A590**, 1995.

[12] J. Cleymans, R. V. Gavai and E. Suhonen. *Quarks and gluons at high energies and temperatures.* Phys. Rep. **130**, 217–292, 1986.

[13] H. Stocker and W. Greiner. *High energy heavy ion collisions-Probing the state of highly excited hadronic matter.* Phys. Rep. **137**, 1, 1986.

[14] H. R. Schmidt and J. Schukraft. *The physics of ultra-relativistic heavy-ion collisions.* J. Phys. **G19**, 1705–1795, 1993.

[15] C.-Y. Wong. *Introduction to High-Energy Heavy-Ion Collisions.* World Scientific, 1994.

[16] R. C. Hwa. *Quark-Gluon Plasma*, volume 6 of Advanced Series on Directions in High Energy Physics. World Scientific, 1990.

[17] I. Tserruya. *Heavy Ion Collisions* To appear in Proc. of the Int. Europhysics Conference in High Energy Physics. Brussels, 27 July - 2 August 1995.

[18] J. Schukraft et al. (HELIOS collab.). *Recent results from Helios(NA34) on proton-proton and nucleus-nucleus reactions.* Nucl. Phys. **A498**, 79c, 1989.

[19] E802 collab. In *Proc. of the Workshop on Heavy Ion Physics at the AGS*, O. Hansen (editor), BNL, USA, 1990.

[20] R. J. Glauber. *Lectures in Theoretical Physics*, volume 1. Interscience, N.Y. 1959.

[21] C.-Y. Wong. *Introduction to High-Energy Heavy-Ion Collisions*, chapter 12. In [15], 1994.

[22] A. Capella et al. *Multiplicity distributions in nuclear collisions.* Phys. Rev. **D35**, 2921, 1987.

[23] J. D. Bjorken. *Highly relativistic nucleus-nucleus collisions: the central rapidity region.* Phys. Rev. **D27**, 140, 1983.

[24] J. P. Blaizot and J. Y. Ollitraut. *Hydrodynamics of Quark-Gluon Plasma*, page 393. Volume 6 of *Advanced Series on Directions in High Energy Physics* [16], 1990.

[25] W. Heck et al. (NA35 collab.). *Study of energy flow in* ^{16}*O-nucleus collisions at 60 and 200 GeV/nucleon.* Z. Phys, **C38**, 19–34, 1988.

[26] S. P. Sorensen et al. (WA80 collab). *Oxygen induced reactions at 60 AGeV and 200 AGeV studied by calorimetry.* Z. Phys, **C38**, 3–14, 1988.

[27] I. Lund et al. (WA80 collab). *Charged particle spectra in ^{16}O induced nuclear collisions at the CERN SPS.* Z. Phys, **C38**, 51–57, 1988.

[28] F. Corriveau et al. (Helios collab.). *Transverse energy distributions in ^{16}O-nucleus collisions.* Z. Phys. **C38**, 15–18, 1988.

[29] H. Satz. In *Proc. of the Joint Int. Lepton-Photon Symp. and Europhysics Conf. on High Energy Physics*, Geneva, Switzerland, Jul 25 - Aug 1 1991.

[30] J. Pišút, N. Pišútová and P. Závada. *Formation time of hadrons and density of matter produced in relativistic heavy ion collisions.* Z. Phys. **C67**, 467–477, 1995.

[31] T. Hatsuda and S. H. Lee. *QCD sum rules for vector mesons inthe nuclear medium* Phys. Rev. C46, R34, 1992.

[32] D. J. Dean et al. *Dynamical evolution of hadronic matter in relativistic collisions.* Phys. Rev. **C48**, 2433, 1993.

[33] T. Alber et al. (NA49 collab.). *Transverse energy production in $^{298}Pb+Pb$ collisions at 158 GeV per nucleon.* Phys. Rev. Lett. **75**, 1995.

[34] T. Alber et al. in [33]
R. Albrecht et al. (WA80 collab.). *Transverse momentum distributions of neutral pions from central and peripheral $^{16}O+Au$ collisions at 200 AGeV.* Z. Phys, **C47**, 367–375, 1990.
T. Akesson et al. (HELIOS collab.). *Inclusive negative particle p_t spectra in p-nucleus and nucleus-nucleus collisions at 200 GeV per nucleon.* Z. Phys. **C46**, 361, 1990.
H. Strobele et al. (NA35 collab.). *Negative particle production in nuclear collisions at 60 and 200 GeV/nucleon.* Z. Phys. **C38**, 89, 1988.
T. Abbott et al. (E802 collab.). *Bose-Einstein correlations in Si+Al and Si+Au collisions at 14.6 AGeV/c.* Phys. Rev. Lett. **69** (7), 1030, 1992.
T. Hemmik et al. (E814 collab.). *Low p_t enhancement in S+Pb collisions at 14.6 GeV/c.* Nucl. Phys. **A566**, 435–438, 1994.

[35] J. Casado et al. *Small p_t particle production in the Dual Parton Model.* Z. Phys. **C46**, 129–131, 1990.

[36] T. Hemmik et al. in [34].

[37] M. Lev and B. Peterson. *Nuclear effects at large transverse momentum in a QCD parton model.* Z. Phys. **C21**, 155–161, 1983.

[38] E. Schnedermann et al. *Thermal phenomenology of hadrons from 200 AGeV in S+S collisions.* Phys. Rev. **C48**, 2462, 1993.

[39] J. Dodd et al. (NA44 collab.). *Charged hadron distributions in pA and AA collisions at the CERN SPS.* Nucl. Phys. **A590**, 523c-526c, 1995.

[40] G. Goldhaber et al. *Influence of Bose-Einstein statistics on the antiproton-proton annihilation process.* Phys. Rev. **120** (1), 300, 1960.

[41] B. V. Jacak et al. (NA44 collab.). *Recent Results from NA44 and a Review of HBT.* Nucl. Phys. **A590**, 215c–232c, 1995.

[42] A. Bamberger et al. (NA35 collab.). *Probing the space-time geometry of ultra-relativistic heavy-ion collisions.* Phys. Lett. **B203**, 320, 1988.

[43] H. Boggild et al. (NA44 collab.). *Identified pion interferometry in heavy ion collisions at CERN.* Phys. Lett. **B302**, 510, 1993.

[44] R. Albrecht et al. (WA80 collab.). *Bose-Einstein correlations in the target fragmentation region in 200 AGeV ^{16}O+nucleus collisions.* Z. Phys. **C53**, 225–237, 1992.

[45] V. Cianciolo et al. (E859 collab.). *Bose-Einstein correlations of positive kaon pairs in E859 - extended results and model comparisons.* Nucl. Phys. **A590**, 459–464, 1995.

[46] P. Koch, B. Mueller and J. Rafelski. *Strangeness in relativistic heavy ion collisions.* Phys. Rep. **142**, 167, 1986.

[47] L. Letessier et al. *Hot hadronic matter and strange anti-baryons.* Phys. Lett. **B292**, 417, 1992.

[48] M. Gazdzicki et al. (NA35 collab.). *New Data on the Strangeness Enhancement in Central Nucleus-Nucleus Collisions at 200 AGeV.* Nucl. Phys. **A566**, 503–506, 1994.

[49] E. Andersen et al. (NA36 collab.). *Results from CERN Experiment NA36 on Strangeness Production.* Nucl. Phys. **A544**, 309–320, 1992.

[50] WA85 collab. In *Proc. of Hadron Structure 92.*, D. Bruncko and J. Urban (editors), Stara Lesna, Czec. Rep. September 1992.

[51] T. Abbott et al. (E802 collab.). *Centrality dependence of K^+ and π^+ multiplicities from Si+A collisions at 14.6 AGeV/c.* Phys. Lett. **B291**, 341–346, 1992.

[52] E810 collab. In *Proc. of the Conference on Heavy Ion Physics at the AGS*, Cambridge, MA. January 1993.

[53] A. Shor. *ϕ Meson Production as a Probe of the Quark-Gluon Plasma.* Phys. Rev. Lett. **54** (11), 1122–1125, 1985.

[54] J. Izuka, K. Okada and D. Shito. *Systematics and phenomenology of boson mass levels.* Prog. Theor. Phys. **35**, 1061, 1966.

[55] C. Baglin et al. (NA38 collab.). *ϕ, ρ and ω production in p-U, O-U and S-U reactions at 200 GeV per nucleon.* Phys. Lett. **B272**, 449, 1991.

[56] M. C. Abreu et al. (NA38 Collab.). *ρ, ω, ϕ production in p+W and S+U collisions at 200-GeV/nucleon.* Nucl. Phys. **A525**, 497c, 1991.

[57] P. Koch, U. Heinz and J. Pisut. *ϕ enhancement and J/ψ suppression in nuclear collisions by rescattering of secondary hadrons.* Phys. Lett. **B243**, 149, 1990.

[58] F. Grassi and H. Heiselberg. *ϕ enhancement in nuclear collisions.* Phys.lett. **B267**, 1, 1991.

[59] K. Haglin. *Collision rates for ρ, ω and ϕ mesons at nonzero temperature.* Nucl. Phys. **A584**, 719–736, 1995.

[60] C. B. Dover. *Aspects of strangeness* Nucl. Phys. **A590**, 333c–345c, 1995.

[61] T. Matsui and H. Satz. *J/ψ suppression by quark-gluon plasma formation.* Phys. Lett. **B178**, 416–422, 1986.

[62] M. C. Abreu et al. (NA38 Collab.). *The production of J/ψ in 200 GeV/A Oxygen-Uranium interactions.* Z. Phys. **C38**, 117, 1988.

[63] J. Ftáčnik et al. *An alternative mechanism of J/ψ suppression in heavy ion collisions.* Phys. Lett. **B 207**, 194–198, 1988.

[64] R. Vogt et al. *J/ψ interactions with hot hadronic matter.* Phys. Lett. **B 207**, 263–268, 1988.

[65] J. P. Blaizot and J. Y. Ollitrault. *The p_t dependence of J/ψ production in hadron-nucleus and nucleus-nucleus collisions.* Phys. Lett. **B217**, 392–396, 1989.

[66] E. V. Shuryak *Quark-gluon plasma and the production of leptons, photons and psions in hadron collisions.* Sov. J. Nucl. Phys. **28**(3), 408–414, 1978.
G. Domokos and J. I. Goldman *Quark matter diagnostics.* Phys. Rev. **D23**, 203, 1981.
K. Kajantie and H. I. Miettinen *Temperature Measurement of Quark-Gluon Plasma Formed in High Energy Nucleus-Nucleus Collisions.* Z. Phys. **C9**, 341-345, 1981.
L. D. McLerran and T. Toimela *Photon and dilepton emission from the quark-gluon plasma: Some general considerations.* Phys. Rev. **D31**, 545, 1985.
K. Kajantie et al. *Dilepton emission and the QCD phase transition in ultrarelativistic nuclear collisions.* Phys. Rev. **D34**, 2746–2754, 1986.
P. Koch *Low mass lepton pair production and pion dynamics in ultrarelativistic heavy ion collisions.* Z. Phys. **C57**, 283–303, 1993.

[67] K. Huang. *Statistical Mechanics.* John Wiley, 1963.

[68] K. Kajantie et al. *Dilepton emission and the QCD phase transition in ultrarelativistic nuclear collisions.* Phys. Rev. **D34**, 2746–2754, 1986.

[69] U. Heinz and K. S. Lee. *The ρ peak in the dimuon spectrum as a clock for fireball lifetimes in relativistic nuclear collisions.* Phys. Lett. **B259**, 162–168, 1991.

[70] H. Gordon et al. (HELIOS Collab.). *Study of high energy densities over extended nuclear volumes via nucleus-nucleus collisions at the SPS.* CERN-SPSC/84-43, 1984.

[71] R. Veenhof. *Low mass muon pair production in 450 GeV p-Be collisions.* PhD thesis, Univ. Amsterdam/NIKHEF, 1993.

[72] A. Baldit et al. CERN, SPSC/85-20/P211 and SPSC/85-42/P211/Add.1 (NA38 Collab. Proposal). 1985.

[73] C. Lourenço. *J/Ψ, ψ' and dimuon production in p-A and S-U collisions at 200 GeV/nucleon.* PhD thesis, Universidade Técnica de Lisboa, Lisboa. Portugal, 1995.

[74] E. F. Barasch et al. (CERES Collaboration). *Study of electron pair production in hadron and nuclear collisions at the CERN SPS.* CERN/SPSC 88-25. SPSC/P237, 1988.

[75] D. Irmscher. *Search for Direct Photons from S-Au collisions at 200 GeV/u.* PhD thesis, Universitat Heidelberg, Heidelberg. Germany, 1994.

[76] A. Schön. *Pion p_t distributions in ultrarelativistic S-Au collisions at 200 GeV/u.* PhD thesis, Universitat Heidelberg, Heidelberg. Germany, 1993.

[77] T. Gunzel. *Production of e^+e^- pairs in $\gamma\gamma$ reactions from distant Sulfur-Platinum collisions.* PhD thesis, Universitat Heidelberg, Heidelberg. Germany, 1993.

[78] N. S. Craigie. *Lepton and photon production in hadron collisions.* Phys. Rep. **47**, 1–108, 1978.

[79] L. G. Landsberg. *Electromagnetic decays of light mesons.* Phys. Rep. **128** (6), 301–376, 1985.

[80] N. M. Kroll and W. Wada. *Internal pair production associated with the emission of high energy gamma rays.* Phys. Rev. **98**, 1355, 1955.

[81] R. P. Feynmann. *Photon-hadron interactions.* Lecture Notes in Physics. Addison Wesley, 1972.

[82] M. Gourdin. *Weak and electromagnetic form factors of hadrons.* Phys. Rep. **11**, 29–98, 1974.

[83] T. H. Bauer et al. *The hadronic properties of the photon in high-energy interactions.* Rev. Mod. Phys. **50** (2), 261–423, 1978.

[84] R. I. Dzhelyadin et al. *Study of the electromagnetic transition from factor in $\omega \to \pi^o\mu^+\mu^-$ decay.* Phys. Lett. **B102**, 296, 1981.

[85] S. D. Drell and T-M. Yan. *Massive lepton pair production in hadron-hadron collisions at high energies.* Phys. Rev. Lett. **25**, 316, 1970.

[86] P. D. B. Collins and A. D. Martin. *Hadron interactions.* Graduate Student Series in Physics. Adam Hilger, Ltd. Bristol, BS1 6NX. UK, 1984.

[87] F. Halzen and A. D. Martin. *Quarks and Leptons.* John Wiley & Sons, 1984.

[88] R. Stroynowski. *Lepton pair production in hadron collisions.* Phys. Rep. **71** (1), 1–50, 1981.

[89] P. V. Ruuskanen. *Dilepton Emission in Relativistic Nuclear Collisions*, page 519. Volume 6 of *Advanced Series on Directions in High Energy Physics* [16], 1990.

[90] S. N. Ganguli, A. Gurtu, and R. Raghavan. *Estimates on hadronic production of $D\bar{D}$ from dilepton mass spectrum in fusion and cluster models.* Phys. Rev. **D32**, 1104, 1985.

[91] C. Lourenço et al. (NA38 Collab.) *J/ψ, ψ' and muon pair production in p-W and S-U collisions.* Nucl. Phys. **A566**, 77c, 1994.

[92] K. Anderson et al. *Inclusive μ pair production at 150 GeV by π^+ mesons and protons.* Phys. Rev. Lett. **37**, 799, 1976.

[93] T. Akesson et al. (AFS collab.). *Production of prompt positrons at low transverse momentum in 63 GeV pp collisions at the CERN intersecting storage rings.* Phys. Lett. **B152**, 411, 1985.

[94] T. Akesson et al. (HELIOS collab.). *Low mass lepton pair production in p-Be collissions at 450 GeV/c.* Z. Phys. **C68**, 47-64, 1995.

[95] A. Drees et al. (CERES Collaboration). *First results of the CERES electron pair spectrometer from p + Be, P + Au and S + Au collisions.* Nucl. Phys. **A566**, 87C, 1993.

[96] M. Aguilar-Benitez et al. (NA27 collab.). *Inclusive particle production in 400 GeV/c pp interactions.* Z. Phys. **C50**, 405, 1991.

[97] CERES Collaboration. *Study of Electron Pair Production in Hadron and Nuclear Collisions at the CERN SPS* CERN/SPSLC 92-48. Addendum II to proposal SPSC/P237.

[98] P. Koch. *Low mass lepton pair production and pion dynamics in ultrarelativistic heavy ion collisions.* Z. Phys. **C57**, 283–303, 1993.

[99] C. Itzykson and J.-B. Zuber. *Quantum Field Theory.* Int. Series in Pure and Applied Physics. McGraw-Hill, 1980.

[100] J. Varela. In *Proc. of Quark Matter '90*, Nucl. Phys. volume A525, page 275c, 1991.

[101] B. D. Serot and J. D. Walecka. *The Relativistic Nuclear Many-Body Problem.* Adv. Nucl. Phys. **16**, 1, 1986.

[102] F. Karsch. *The Phase Transition to the Quark Gluon Plasma: Recent Results from Lattice Calculations.* Nuc. Phys, **A590**, 367c–382c, 1995.

[103] A. Casher. *Chiral symmetry breaking in quark confinment theories.* Phys. Lett. **83B**, 395–398, 1979.

[104] C. Dominguez and M. Loewe. *Dimuon production in ultrarelativistic nuclear collisions and QCD phase transitions.* Z. Phys. **C49**, 423, 1991.

[105] F. Karsch, K. Redlich and L. Turko. *Chiral symmetry and dileptons in heavy ion collisions.* Z. Phys. **C60**, 519, 1993.

[106] U. Heinz. *Strangeness production and chemical equilibration in relativistic nuclear collisions.* Nucl. Phys. **A566**, 205–216, 1994.

[107] G. E. Brown and C. M. Rho. *Scaling effective Lagrangians in a dense medium.* Phys. Rev. Lett. **66**, 2720, 1991.

[108] M. Asakawa and C. M. Rho. *QCD sum rules for a rho meson in dense matter.* Nucl. Phys. **A560**, 399, 1993.

[109] G. Q. Li and C. M. Ko. *Can dileptons reveal the in-medium properties of vector mesons?* Nucl. Phys, **A582**, 731, 1995.

[110] M. Hermann, B. Friman and W. Norenberg. *Properties of rho mesons in nuclear matter.* Nucl. Phys. **A560**, 411, 1993.

[111] V. Steiner. *The CERES Spectrometer for the Measurement of e+e- Pairs in Relativistic Hadron Collisions.* PhD thesis, Weizmann Institute of Science, Rehovot. Israel, 1993.

[112] R. Baur et al. (CERES Collaboration). *The CERES RICH detector system.* Nucl. Instrum. Meth. **A343**, 87, 1993.

[113] T. F. Gunzel et al. *A Silicon Pad counter for first level triggering in ultrarelativistic proton-nucleus and nucleus-nucleus collisions.* Nucl. Instr. Methods, **A316**, 259–266, 1992.

[114] W. Chen et al. (CERES collab.). *Performance of the multianode cylindical silicon drift detector in the CERES NA45 experiment: first results.* Nuc. Inst. Meth. **A326**, 273–278, 1993.

[115] PDG. *Review of Particle Properties.* Phys. Rev. **D50**, 1994.

[116] Y-S. Tsai. *Pair production and bremsstrahlung of charged leptons.* Rev. Mod. Phys. **46**, 815, 1974.

[117] T. Akesson et al. (HELIOS collab.). *Inclusive photon production in pA and AA collisions at 200 Gev/u.* Z. Phys. **C46**, 369, 1990.

[118] G. Tel Zur. Private communication.

[119] M. Bourquin and J.-M. Gaillard. *A simple phenomenological description of hadron production.* Nucl. Phys. **B114**, 334–364, 1976.

[120] I. Ravinovich. A Hadron Generator for pp, pA and AA Collisions. Weizmann Institute note, 1995.

[121] D. Rohrich et al. (NA35 Collab.). *Hadron production in S-Ag and S+Au Collisions at 200 Gev/n.* Nucl. Phys. **A566**, 35c–44c, 1994.

[122] G. J. Gounaris and J. J Sakurai. *Finite width corrections to the vector meson dominance prediction for* $\rho \to e^+e^-$. Phys. Rev. Lett. **21**, 244, 1968.

[123] R. I. Dzhelyadin et al. *Study of* $\eta \to \mu^+\mu^-$ *decay.* Phys. Lett. **B97**, 471, 1980.

[124] W. T. Eadie et al. (editors). *Statistical Methods in Experimental Physics.* North Holland, Amsterdam, 1971.

[125] V. Cerný, P. Lichard and J. Pisut. *A clear-cut test of low mass dilepton production mechanism in hadronic collisions.* Z. Phys. **C31**, 163–166, 1986.

[126] A. Masera et al. (HELIOS collab.). In *Proc. of Quark Matter '95*, J. W. Harris A. M. Poskanzer and L. S. Schroeder (editors), Nucl. Phys. volume A590, page 93, 1995.

[127] G. Agakichev *et. al.* (CERES coll.) *Enhanced production of low mass electron pairs in 200-GeV/u S - Au collisions at the CERN SPS* Phys. Rev. Lett. **75**, 1272, 1995.

[128] C. Lourenço. In *Proc. of the* 5^{th} *conference on Intersections between Particle and Nuclear Physics.*, St. Petesburg, Florida (US), 1994.

[129] G. Q. Li, C. M. Ko and G. E. Brown. *Enhancement of Low-Mass Dileptons in Heavy Ion Collisions.* Phys. Rev. Lett. **75**, 4007–4010, 1995.

[130] G. Q. Li, C. M. Ko, H. Sorge and G. E. Brown. *Dilepton produciton in proton-nucleus and nucleus-nucleus collisions at SPS energies* Unpublished and private communication of G. Li.

[131] H. Sorge, H. Stocker and W. Greiner *Poincare invariant Hamiltonian dynamics: Modeling multi-hadronic interactions in a phase space approach.* Ann. Phys. **192**, 266, 1989.

[132] C. M. Ko, Q. Li and R. Wang. *Relativistic Vlasov Equation for Heavy-Ion Collisions.* Phys. Rev. Lett. **59**, 1084–1087, 1987.

[133] C. M. Ko and Q. Li. *Relativistic Vlasov-Uehling-Uhlenbeck model for Heavy-Ion Collisions.* Phys. Rev. **C37**, 2270–2273, 1988.

[134] W. Cassing, W. Ehehalt and C. M. Ko. *Dilepton production at SPS energies* Phys. Lett. **B363**, 35–40, 1995.

[135] E. Ehehalt and W. Cassing. *Relativistic Transport Approach for Nucleus-Nucleus Collisions based on a NJL Lagrangian.* Sub. to Nucl. Phys A. hep-ph/9507274. 1995.

[136] D. K. Srivastava, B. Sinha and C. Gale. *Excess production of low mass electron pairs in S-Au collisions at CERN-SPS and quark-hadron phase transition.* Phys. Rev. C (in press), 1995.

[137] R. C. Hwa and K. Kajantie. *Diagnosing quark matter by measuring the total entropy and the photon or dilepton emission rates.* Phys. Rev. **D32**, 1109, 1985.

[138] C. Gale and P. Lichard. *Lepton pairs from thermal mesons.* Phys. Rev. **D49** (7), 3338–3344, 1994.

[139] W. Cassing, W. Ehehalt and I. Kralik. *Analysis of the HELIOS-3* $\mu^+\mu^-$ *Data with a Relativistic Transpot Approach* hep-ph/9691214, Jan. 1996.